Experiments with an Entangled System of a Single Atom and a Single Photon

Wenjamin Rosenfeld

München 2008

Experiments with an Entangled System of a Single Atom and a Single Photon

Wenjamin Rosenfeld

Dissertation
an der Fakultät für Physik
der Ludwig–Maximilians–Universität
München

vorgelegt von
Wenjamin Rosenfeld
aus Odessa

München, den 26.09.2008

Erstgutachter: Prof. Harald Weinfurter
Zweitgutachter: Prof. Gerhard Rempe
Tag der mündlichen Prüfung: 21.11.2008

Zusammenfassung

Verschränkung ist eines der grundlegendsten Merkmale in der Quantenmechanik. Sie beschreibt einen nicht separierbaren Zustand von zwei oder mehr quantenmechanischen Objekten und besitzt z. T. Eigenschaften, welche dem klassischen physikalischen Sinn widersprechen. Während das Konzept der Verschränkung, welches bereits von E. Schrödinger in 1935 eingeführt wurde, allgemein gut verstanden ist, stellen die Erzeugung und Analyse von verschränkten Zuständen noch immer eine erhebliche Herausforderung dar. Insbesondere die Verschränkung von verschiedenartigen Objekten wie Atomen und Photonen wurde erst vor kurzem erreicht und ist Gegenstand aktiver Forschung.

Diese Arbeit berichtet über Experimente mit Verschränkung zwischen einem einzelnen Rubidium Atom und einem einzelnen Photon. Das Atom wird in einer optischen Falle gehalten, wo es exakt lokalisiert ist und sein interner Zustand mit Laserpulsen manipuliert werden kann. Zur Erzeugung der Verschränkung wird das Atom optisch in ein kurzlebiges höheres Niveau angeregt, von wo aus es unter Ausstrahlung eines einzelnen Photons zurück in den Grundzustand fällt. Die Polarisation des emittierten Photons ist verschränkt mit dem Spin des Atoms. In dieser Arbeit wurden Methoden entwickelt, die Präparation und Analyse des Atom-Photon Zustandes mit hoher Genauigkeit erlauben. Um den Zustand für weitere Anwendungen verfügbar zu machen, mussten mehrere Probleme gelöst werden. Erstens ist der interne Zustand des Atoms empfindlich gegenüber äußeren Störungen, insbesondere durch magnetische und elektromagnetische Felder. Um den Zustand des Atoms während des Experiments (welcher auf der Skala von Mikrosekunden abläuft) zu erhalten, wurde u. a. ein System zur aktiven Stabilisierung der Magnetfelder entwickelt. Zweitens muss das vom Atom emittierte Photon zu einem anderen Ort übertragen werden, dabei soll sein Zustand erhalten bleiben. Für diesen Zweck wurde eine faseroptische Strecke von 300 Metern Länge aufgebaut. Wegen der mechanisch bedingten Doppelbrechung in der Faser, ändert sich der Polarisationszustand des Photons während der Übertragung. Deshalb wurde ein System zur aktiven Kompensation der Doppelbrechung entworfen und installiert. Um die Zuverlässigkeit der optischen Verbindung zu bestätigen, wurde das vom Atom emittierte Photon übertragen und Verschränkung nachgewiesen.

Der neue Typ der Verschränkung hat viele Anwendungen, insbesondere im Bereich der Quanten-Informationsverarbeitung. Die Fähigkeit, Superpositionszustände und verschränkte Zustände zu speichern und zu verarbeiten, erlaubt effiziente Lösung von speziellen Problemen, welche auf klassischen Computern nicht innerhalb realistischer Zeit lösbar sind. Darüber hinaus erfordert und ermöglicht die quantenmechanische Natur dieser Information prinzipiell neue Methoden der Kommunikation (z.B. Quanten-Teleportation und Kryptographie). Ein Teil dieser Arbeit beschäftigt sich mit der Implementierung des Protokolls zur Quantenteleportation an dem verschränkten Atom-Photon Paar. Ein Zustand, welcher auf das Photon kodiert wurde, konnte erfolgreich auf den atomaren Spin über eine Entfernung von 5 Metern teleportiert werden.

Mit Hilfe der Methoden und Instrumente, welche während dieser Arbeit entwickelt wurden, wird es möglich, zwei Atome über eine große Entfernung zu verschränken. Dazu ist es geplant, zwei separate Atomfallen simultan zu betreiben, um zwei verschränkte Atom-Photon Paare gleichzeitig zu erzeugen. Die Interferenz der Photonen erlaubt dann einen verschränkten Zustand für die zwei Atome zu erhalten, eine Schlüsselvoraussetzung für einen fundamentalen Test der Quantenmechanik, den so genannten Bell Test.

Summary

Entanglement is one of the most fundamental features in quantum mechanics. It describes a non-separable state of two or more quantum objects and has certain properties which contradict common physical sense. While the concept of entanglement between two quantum systems, which was introduced by E. Schrödinger in 1935, is well understood, its generation and analysis still represent a substantial challenge. Especially entanglement between objects of different nature like atoms and photons was achieved only very recently and is subject of current research.

This thesis presents experiments on entanglement between a single Rubidium atom and a single photon. The atom is stored in an optical trap where it is well localized and its internal state can be manipulated by laser pulses. For generation of entanglement the atom is optically excited into a short-lived upper level from where it falls back emitting a single photon whose polarization is entangled with the atomic spin. During this work methods were developed which allow to prepare and to analyze the atom-photon state with high accuracy. In order to make the entangled state available for further applications, several problems had to be solved. First, the internal atomic state is sensitive to external influence, in particular to magnetic and electromagnetic fields. To preserve the quantum state of the atom during the experimental time (which is of the order of microseconds) the external fields were compensated using a specially developed active stabilization system. The second problem is the communication of the photon to a different location. For this purpose an optical fiber link of 300 meters was set up. Since the polarization state of the photon is changed during propagation due to mechanically and thermally induced birefringence in the fiber, a system for an active maintenance of polarization was implemented. Atom-photon entanglement was distributed over this fiber link confirming its reliability.

The new type of entanglement has many applications, particularly in the field of quantum information processing and communication. The ability to store and process quantum superpositions and entangled states allows to efficiently solve certain problems which can not be solved on classical computers within reasonable time. Furthermore the quantum nature of this information requires and enables fundamentally new communication methods (e.g. quantum teleportation and cryptography). A part of this thesis was dedicated to an implementation of the quantum teleportation protocol on the entangled atom-photon system. A state encoded onto the photon was successfully teleported to the atomic spin over a distance of 5 meters.

Using the tools developed in this work, it becomes feasible to entangle two atoms over a large distance. For this purpose two identical atomic traps will be operated simultaneously producing two entangled atom-photon pairs. The interference of photons will allow to entangle the two atoms providing a key ingredient for a fundamental test of quantum mechanics, the so-called Bell test.

Contents

1. Introduction **9**

2. Atom-Photon Entanglement **12**
2.1. Introduction . . . 12
2.2. The atomic qubit . . . 12
2.3. Principle of atom-photon entanglement . . . 14
2.4. A trap for single neutral atoms . . . 15
2.4.1. Principle of operation . . . 15
2.4.2. Vacuum chamber and optics . . . 16
2.4.3. Optical dipole trap . . . 17
2.4.4. Magneto-optical trap and loading of atoms . . . 18
2.4.5. Lasers . . . 20
2.4.6. Photon detection . . . 20
2.5. Generation of atom-photon entanglement . . . 21
2.6. Detection of the atomic state . . . 22
2.6.1. Hyperfine level detection . . . 23
2.6.2. STIRAP . . . 23
2.6.3. State selectivity . . . 25
2.6.4. Technical realization of the STIRAP process . . . 26
2.6.5. Detection accuracy and detection efficiency . . . 27
2.7. Experimental results . . . 28
2.7.1. Experimental sequence . . . 28
2.7.2. Atom-photon correlations . . . 29
2.7.3. Quantum state tomography of the entangled atom-photon state . . . 30
2.7.4. Violation of Bell's inequality . . . 31
2.8. Summary . . . 32

3. Remote Preparation of an Atomic Quantum Memory **33**
3.1. Introduction . . . 33
3.2. Theoretical scheme . . . 33
3.2.1. Quantum teleportation . . . 33
3.2.2. Remote State Preparation . . . 35
3.3. Experimental Realization . . . 37
3.3.1. Double interferometer setup . . . 38
3.3.2. Interferometer stabilization . . . 41
3.3.3. Control of the interferometer phase . . . 44
3.3.4. Effects of birefringence in the setup . . . 45
3.4. Analysis of the experimental results . . . 46
3.4.1. Tomography of prepared states . . . 46

3.5. Summary . . . 51

4. Coherence Properties of the Atomic Qubit 52
4.1. Introduction . . . 52
4.2. Mechanisms leading to dephasing . . . 53
4.3. Evolution of a spin-1 system in an effective magnetic field . . . 55
4.4. A model for dephasing . . . 56
4.4.1. Static field model . . . 56
4.4.2. Dynamic field effects . . . 58
4.4.3. The role of a magnetic guiding field . . . 60
4.4.4. Effect of the dipole trap upon the atomic state . . . 61
4.5. Measurement and active control of magnetic fields . . . 64
4.5.1. Active control of magnetic fields . . . 66
4.6. Experimental results . . . 68
4.6.1. Measurement of the state evolution . . . 68
4.6.2. Improvements due to stability of magnetic field and trap polarization . . . 69
4.6.3. Effect from polarization of the dipole trap light . . . 71
4.6.4. Effect of the guiding field . . . 72
4.7. Partial tomography of the state evolution . . . 72
4.8. Summary . . . 75

5. Distribution of Entanglement over Long Distance 77
5.1. Introduction . . . 77
5.2. Measurement of polarization drifts in optical fibers . . . 77
5.2.1. Reference polarimeter . . . 78
5.3. Active stabilization of fiber birefringence . . . 80
5.3.1. Polarization controller . . . 80
5.3.2. Parameter optimization algorithm . . . 81
5.3.3. Performance . . . 82
5.4. Atom-photon entanglement over 300 meter fiber . . . 83
5.5. Summary . . . 84

6. Summary and Outlook 85

A. Definition of light polarizations and atomic states 87

B. Quantum state tomography and quantification of state coherence 89

C. Distribution of potential energy of a single atom in a harmonic trap 92

D. Polarization effects in strongly focused beams 96

Bibliography 99

1. Introduction

На озарённый потолок
ложились тени,
скрещенья рук, скрещенья ног,
судьбы скрещенья.

Б. Пастернак

The study of single microscopic systems gives insight into the structure of our physical world at a very fundamental level. The elementary building blocks of matter, the atoms, as well as the units of electromagnetic field, the photons, obey the laws of quantum mechanics. This leads to many counter-intuitive consequences. One of the most interesting non-classical properties in quantum mechanics is entanglement. Two entangled particles are in a common, not separable quantum state even if they are spatially separated. This "non-local" behavior together with the inherent indeterminism (only probabilities of measurement outcomes can be predicted) led to serious doubts in the correctness of the quantum theory.

In 1935 Einstein, Podolsky and Rosen (EPR) formulated their famous question [1] on the completeness of quantum mechanics, also known as the EPR-paradox. By requiring reality, locality and completeness, which are (according to EPR) necessary properties of any physical theory, they constructed a gedankenexperiment apparently contradicting quantum theory. The contradiction can be solved by either abandoning the concept of reality or locality, or by extending the quantum theory with so-called local hidden variables (LHV). The LHV extension would make the theory local, realistic and deterministic.

In 1964 John Bell constructed an inequality, which allowed for the first time to distinguish quantum mechanics from any LHV theory, referred to as Bell's inequality [2]. Based on this inequality an experimental test of LHV concepts was proposed [3]. Such test involves correlation measurements on a pair of entangled particles and predicts a limit for the outcome in LHV theory. This limit is violated by quantum mechanics. First experimental tests of Bell's inequality [4, 5, 6] supported the concept of quantum theory, however two fundamental issues, so-called "loopholes", were not accounted for. First, such test requires strict independence of the two measurements (in the sense of special relativity). This "locality loophole" was closed in an experiment with entangled photons [7] over a distance of $400\,\mathrm{m}$. Second, the test requires detection of at least $\frac{2}{3}$ of the entangled pairs [8], otherwise, no strict conclusions can be done on the whole ensemble. This "detection loophole" was closed in an experiment with two neighboring ions in a trap [9], however, the locality condition could not be satisfied due to small spatial separation of only few $\mu\mathrm{m}$. Until today no experiment has managed to close both loopholes at the same time. One possible solution is to entangle two atoms at a large distance, where the high atomic detection efficiency could be combined with the locality condition. Starting with two atoms, each entangled with a photon, the scheme of entanglement-swapping can be used to entangle the atoms [10].

Besides of fundamental questions, the ability to control quantum systems opened up the new field of quantum information processing. The elementary units of information here are quantum bits or

qubits. In contrast to classical bits, which are well defined in one of their logical states ("0 " or "1"), a quantum bit can also be in a superposition like $\frac{1}{\sqrt{2}}(|0\rangle + |1\rangle)$. Additionally, while classical bits are independent, several quantum bits can be in an entangled state. These unique properties of quantum mechanics allow to cardinally reduce the computational complexity of certain problems. Well-known examples are the factorization of large numbers [11] and database search [12]. Although a full-scale quantum computer is beyond reach of current technology, impressive experimental demonstrations of basic operations and elementary algorithms were already performed in nuclear magnetic resonance systems (NMR) [13], trapped ions [14] and trapped neutral atoms [15].

The main difficulty in the observation of quantum effects is to isolate a quantum system from the environment. Any interaction with the environment leads to a change of the quantum state and finally to the loss of coherence of superposition states. On the other hand any manipulation of the system requires an influence from outside. A compromise has to be found between the isolation of the system (and therefore the purity of its observation) and its controllability. Technological advances of recent years, such as laser cooling and trapping of individual neutral atoms or ions provide a well-isolated quantum system almost on demand. Furthermore, the techniques of spectroscopy and manipulation, e.g. with lasers and microwaves, allow to control the internal atomic states. These achievements make it possible to experimentally study one of the most fundamental systems - a single atom interacting with a single photon.

In this thesis I will describe experiments with a single, optically trapped neutral $^{87}\mathrm{Rb}$ atom which is entangled with a single photon. The quantum state is encoded in long-lived Zeeman substates of the atomic hyperfine ground level. The entanglement is generated by using spontaneous optical decay in a Λ-type system giving an entangled state between the spin of the atom and the polarization of the emitted photon [16]. This is one of the first systems where entanglement between light and matter was directly observed [17, 18]. As well, this type of entanglement was generated with a single trapped $^{111}Cd^{+}$ ion [19], and with a single $^{87}\mathrm{Rb}$ atom strongly coupled to a high-finesse optical resonator [20]. Entanglement between a photon and a collective excitation in an atomic ensemble was reported in [21]. The first challenge of this work was characterize the entanglement and to make it available for further experiments. Chapter 2 describes the methods and techniques necessary for this task.

One of the most interesting experiments which can be performed with an entangled system is quantum teleportation. It allows to transfer the quantum state from one particle to another without need of direct interaction. From the point of view of quantum communication it solves the non-trivial problem of transferring an unknown quantum state which can not be directly inferred by a direct measurement. Chapter 3 describes the experimental realization of a protocol which is based on teleportation. Here the internal quantum state of the atom is prepared remotely by using its entanglement with the photon. The state is imprinted onto the photon by using an additional degree of freedom (spatial mode) and then teleported onto the atom. With our setup we demonstrate this so-called "remote state preparation" achieving a faithful mapping of photonic quantum states onto the atom.

For using the single trapped atom as a quantum memory device, as well as for experiments which require the ability to maintain the quantum state for a certain time, the coherence properties of the internal atomic state are important. In general, the important parameters are the stability of the involved atomic states (which may decay) and their sensitivity upon external influence. The Zeeman states in our experiment are stable ground states, however, due to their magnetic moment they are influenced by external magnetic fields and by the optical field of the trap. These effects are studied in chapter 4 and a model is developed, which allows to explain the observed dephasing. In order to increase the useful coherence time, several improvements were introduced including an active stabilization of magnetic fields.

The advantage of the interface between atomic based quantum memories and photonic communication channels provided by atom-photon entanglement, is that the photon can be sent over, in principle, arbitrary distances via free-space links or optical fibers. In practice the distance is limited by absorption (for free-space also diffraction). Additionally, in optical fibers the polarization state of the transmitted photons is distorted due to birefringence. These reasons make experiments over long distance difficult. Chapter 5 describes the realization of a stable optical fiber link of $300\,\mathrm{m}$ which allows to transfer the entangled photon to a remote location. In order to preserve the polarization state of the photon during transmission an automatic active polarization control was realized. The system was tested by distributing and analyzing atom-photon entanglement over the long fiber.

2. Atom-Photon Entanglement

2.1. Introduction

Entanglement is one of the most striking features of quantum mechanics. It exhibits highly non-classical properties and has various applications in quantum information processing and communication [22]. Furthermore it allows to increase the resolution in lithography and metrology [23]. The technology of entanglement generation has rapidly advanced in recent years. Generation of polarization entangled photons was already performed in 1960-ies using atomic cascade transitions [24]. Nowadays up to 6 [25] entangled photons can be observed using the spontaneous parametric down-conversion (SPDC) technique, producing a variety of multi-particle entangled states [26]. The availability of higher laser powers allows to increase the efficiency of this process and the number of entangled photons. On the other hand, big progress was achieved in trapping and manipulation of atomic systems. Entanglement of up to 8 ions was produced [27] by using collective oscillation of ions in a trap and several thousand neutral atoms in an optical lattice were entangled using collisions [28].

Entanglement considered so far was only between objects of the same type (photon-photon or atom-atom). For future applications in quantum information and communication it is necessary to combine the advantages of atomic systems (long coherence times, advanced manipulation techniques, high detection efficiency) with that of photons (long-distance communication). Entanglement between atomic systems and photonic communication channels forms the necessary interface allowing a variety of new applications. The first direct observation of entanglement between light and matter was achieved between a single photon and a single trapped ion [19] and neutral atom [16]. Entanglement between photons and atomic ensembles was reported as well [21].

This chapter describes the generation and characterization of entanglement between the spin of a single trapped $^{87}\mathrm{Rb}$ atom and the polarization of a photon at a wavelength of $780\,\mathrm{nm}$. In order to achieve this task we use an optical dipole trap to isolate a single atom. Entanglement between the internal atomic state and the polarization of the photon is generated in spontaneous decay in a Λ-type transition. A novel detection method allows to perform quantum state tomography of the internal atomic state. Together with polarization analysis of the photon, full quantum state tomography of the entangled atom-photon state can be performed. Additionally, violation of Bell's inequality with the atom-photon system was observed giving additional evidence of the underlying entanglement.

2.2. The atomic qubit

The ability to perform the necessary experimental tasks relies on the proper choice of the atomic system. For the purposes of our experiment it has to satisfy the following criteria:

- presence of stable ground states which are suitable for encoding a qubit and which have preferably a simple structure

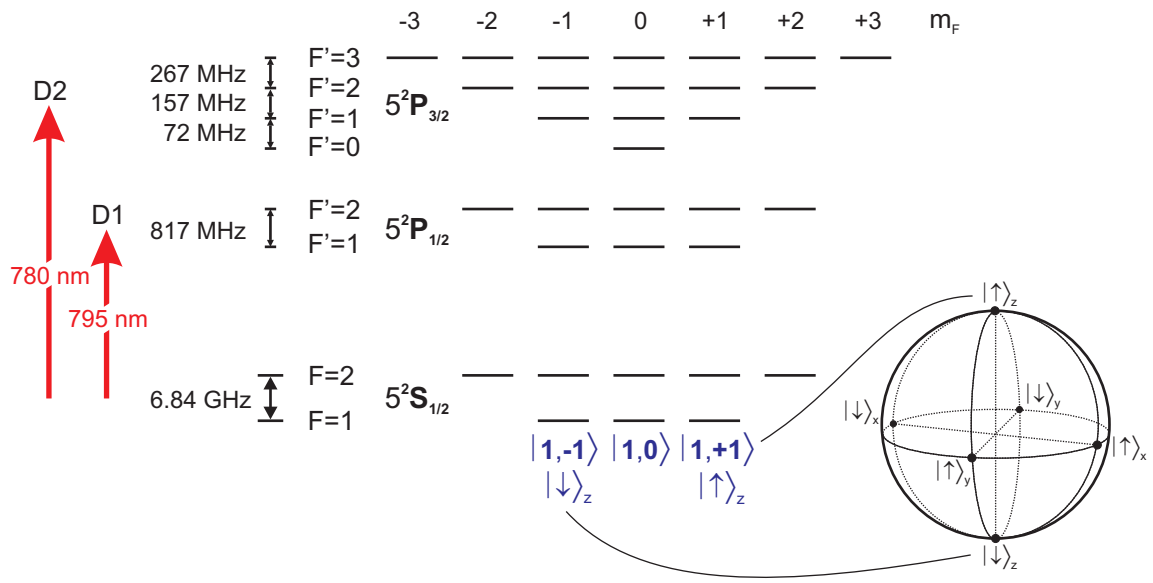

Figure 2.1.: Energy levels of $^{87}\mathrm{Rb}$. Shown is the ground level $5^2S_{1/2}$ and the first two exited levels $5^2P_{1/2}$ and $5^2P_{3/2}$ with their respective hyperfine splittings. The qubit is encoded in the $|F = 1, m_F = \pm 1\rangle$ states of the ground level. The inset shows the Bloch sphere representation of the atomic qubit states. The eigenstates of $\hat{\sigma}_z$ - $|\downarrow\rangle_z$ and $|\uparrow\rangle_z$ are located on the poles, while their superpositions - the eigenstates of $\hat{\sigma}_x$ and $\hat{\sigma}_y$ - lie on the equator.

- the qubit states have to form a Λ-type system with an excited state for the generation of entanglement
- the optical transitions for cooling, preparation, etc. have to be accessible with present laser technology
- the optical transition which generates the entanglement must have a wavelength suitable for communication over optical fibers

The element which has the required properties is Rubidium, $^{87}\mathrm{Rb}$, which is an alkaline metal with a single outer electron. It has a nuclear spin $I = \frac{3}{2}$ leading to the ground state $5^2S_{1/2}$ with a hyperfine splitting in $F = 1$ and $F = 2$ (see Fig. 2.1). The $F = 1$ and $F = 2$ hyperfine levels consist of 3 and 5 Zeeman substates respectively. The first exited state is split due to the fine interaction into $5^2P_{1/2}$ and $5^2P_{3/2}$ states with their corresponding hyperfine and Zeeman structure. For convenience we will use for the ground hyperfine substates the symbol $|F, m_F\rangle$ and for excited states $|F', m'_{F'}\rangle$. The optical dipole transitions from the ground state into exited state manifolds $5^2P_{1/2}$ and $5^2P_{3/2}$ are called the $D1$ and the $D2$ transitions, respectively. The corresponding transition wavelengths of $780\,\mathrm{nm}$ respectively $795\,\mathrm{nm}$ are accessible with well-established diode-laser technology and also suitable for communication over optical fibers. Additionally, single photon detectors with an efficiency of ≥ 0.6 are available for this wavelength range.

This atom is especially well-suited for the purpose of our experiment because of the simplicity of its $F = 1$ ground level which has only three substates. The qubit is encoded into the two long-lived Zeeman states $|F = 1, m_F = -1\rangle$ and $|F = 1, m_F = +1\rangle$, which are degenerate in absence of a magnetic field. They correspond to the combined atomic spin being oriented “down” or “up”. These

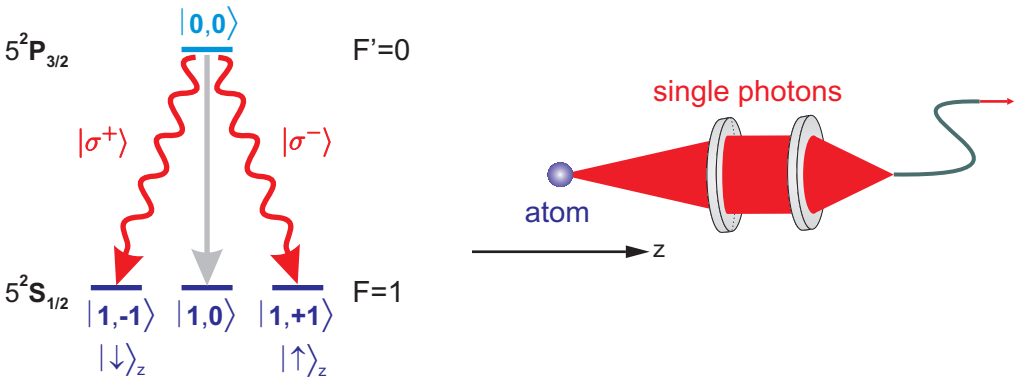

Figure 2.2.: Principle of atom-photon entanglement. The exited atomic state $|F' = 0, m_{F'} = 0\rangle$ has three possible optical decay channels. The polarization of the emitted photon is entangled with the final state of the atom. Coupling the emitted light into a single-mode fiber suppresses the collection of photons from the π-decay. The common optical axis of the objective and of the optical fiber define the quantization axis z.

two states together with a selected excited state (e.g. $5^2P_{3/2}|F' = 0, m_{F'} = 0\rangle$) form a Λ-system, which is a crucial element for the generation of atom-photon entanglement. In terms of a qubit we shall call these states $|\downarrow\rangle_z$ and $|\uparrow\rangle_z$ respectively, where the z-axis is the quantization axis, defined in the experiment by the photon collection optics. In this subspace, the standard formalism of a two-level systems can be applied. The basis states can be expressed as eigenstates of the Pauli operators $\hat{\sigma}_x$, $\hat{\sigma}_y$, $\hat{\sigma}_z$, also any state can be represented on the Bloch sphere as shown in Fig. 2.1.

2.3. Principle of atom-photon entanglement

In our experiment atom-photon entanglement is generated in the spontaneous decay of an exited atomic state, see Fig. 2.2. Starting with the state $|F' = 0, m_{F'} = 0\rangle$, which has a lifetime of 26 ns, the atom will decay optically into the $F = 1$ manifold. The decay into the $|1, -1\rangle$ and $|1, +1\rangle$ states leads to emission of a σ^+ or σ^- photon (left- or right-circularly polarized), respectively, while in the decay into the $|1, 0\rangle$ state a photon with π-polarization (linear, along quantization axis) is emitted. This corresponds to the conservation of angular momentum since a σ-photon carries one unit of $\hbar$ and a π-photon has an expectation value of the (internal) angular momentum equal to zero. In the case of complete degeneracy of the two qubit states both decay channels have the same energy.

The emitted light is collected by a microscope objective and coupled into a single mode optical fiber. It is important to note that this step filters out the light from the π-transition. The reason is that the spatial emission function of the π-transition (corresponding to emission of a dipole oscillating exactly along the quantization axis) is antisymmetric with respect to the quantization axis. Therefore, this light is not coupled into the optical fiber whose mode-function (Gaussian TEM_{00}) is symmetric [18]. This result is valid for any aperture size of the collecting objective.

Since the system of the atom together with the emitted photon is closed, the emission process is coherent. In particular the total system after the emission is in a pure state which is a coherent superposition of the $\sigma^{\pm}$ decay paths:

$$\left|\Psi^{+}\right\rangle = \frac{1}{\sqrt{2}}\left(\left|1,-1\right\rangle\left|\sigma^{+}\right\rangle + \left|1,+1\right\rangle\left|\sigma^{-}\right\rangle\right) \tag{2.1}$$

The phase between the two components is determined by the Clebsch-Gordan coefficients of the optical transition [29]. The restriction to the two decay channels leads to the generation of a perfectly entangled state between the atomic qubit encoded in the spin and the polarization of the photon. This generation process is probabilistic because the spontaneous emission is not directed. The efficiency therefore depends on the numerical aperture of the collecting objective together with the coupling efficiency into the single-mode optical fiber.

2.4. A trap for single neutral atoms

For the experimental realization of atom-photon entanglement, as well as for any experiment with a single atom, the first requirement is to trap and to isolate a single atom. Furthermore the atom has to be accessible for manipulation and detection. The trap has to provide sufficient holding time and to preserve the internal atomic state. The possible candidates for trapping of single atoms are magneto-optical trap (MOT), magnetic trap and optical dipole trap. The MOT relies on forces resulting from scattering of light, and therefore does not preserve the internal state. The magnetic trap is state dependent - it uses magnetic polarization of the atom, so it can not trap both of the Zeeman states which constitute the qubit. The only available trapping principle which is capable to fulfill our requirements is based on the optical dipole force.

2.4.1. Principle of operation

The origin of optical dipole force is the well-known effect of interaction of an electrically polarizable medium with an electric field. It leads to an attraction (repulsion) of the medium into the region of the strongest electric field where its energy is the lowest (highest). In the optical case it is the interaction of the oscillating atomic electric dipole moment which is induced by the light field with the driving electric field itself. In the case of red-detuning, i.e. the frequency of the incident light ω_L being below any of the atomic transition frequencies, the driving electric field and the atomic dipole will oscillate in phase. This leads to an attractive force towards the region of highest light intensity.

In quantum mechanics this effect is called AC-Stark shift and leads to lowering of the atomic ground state energy, which is equivalent to the presence of an attractive potential. The depth of the potential depends on the light intensity I and the detuning from the resonance $\Delta := \omega_0 - \omega_L$, where ω_0 is the atomic transition frequency and ω_L the frequency of light. In the case of a two-level atom one easily gets the relation for the energy shift ΔE of the atomic states by diagonalization of the interaction Hamiltonian. For large detuning this so-called light-shift is given by

$$\Delta E = \mp\frac{\hbar\Omega^2}{4\Delta}$$

where $\Omega := \frac{1}{\hbar}\mathcal{E}\cdot d$ is the Rabi frequency which depends on the electric field amplitude $\mathcal{E}$ and the atomic dipole moment d. For red detuning, i.e. $\omega_L < \omega_0$, the ground state is lowered leading to the dipole potential $U_{dipole} \sim \frac{I}{\Delta}$, the excited state is shifted in opposite direction. In a real atom several ground and excited state exist, and the coupling of each transition to the optical field contributes to the energy shift. In the limit of large red detuning in $^{87}\mathrm{Rb}$ one considers only the coupling of the ground level $5^2S_{1/2}$ to the first two excited levels $5^2P_{1/2}$, $5^2P_{3/2}$ without sub-structure (i.e. the hyperfine structure

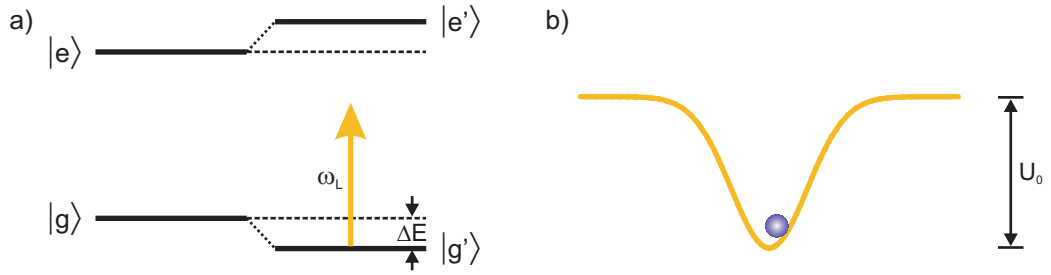

Figure 2.3.: Light-shift in a two-level atom. Interaction with light of frequency ω_L far detuned from the atomic resonance shifts the atomic states (a). In case of red-detuning this shift can be used for trapping in e.g. Gaussian light-field configuration (b). The trapping potential U_0 is proportional to the light intensity.

is not resolved). In this case the light-shift of the atomic ground level for linear light polarization is given by:

$$U_{dipole} = \Delta E = -\frac{\pi c^2}{2}\frac{\Gamma_D}{\omega_D^3}\left(\frac{1}{\Delta_{D1}} + \frac{2}{\Delta_{D2}}\right) \cdot I \tag{2.2}$$

where Γ_D are the scattering rates, ω_D the resonance frequencies and Δ_D the detunings for the $D1$ and the $D2$ transitions respectively. The factor $\frac{\Gamma_D}{\omega_D^3}$ is equal for both transitions.

In order to use this effect for atom trapping one has to create a light field configuration with (at least one) local maximum of intensity. A simple and convenient configuration is a focused Gaussian beam. The confinement depends then on the focusing parameters, i.e. on the waist w_0 of the beam and its Rayleigh range z_R. As will be shown in the following sections, the dipole trap can be arranged to capture single atoms and to provide excellent optical access for laser manipulation and detection.

2.4.2. Vacuum chamber and optics

The storage time of atoms in the dipole trap is limited mainly by collisions with the background gas, therefore the experiment has to be performed under ultra-high vacuum conditions. For this purpose we use a spectroscopy glass cell (Hellma, uncoated) which is attached to a vacuum chamber and allows a compact setup with a very good optical access. The cell has inner dimensions of $25 \times 25 \times 70\,\mathrm{mm}$ with $2.5\,\mathrm{mm}$ glass thickness. It contains a Rubidium dispenser operated at a current of $2.4\,\mathrm{A}$ providing a source of thermal Rubidium atoms. An ion-getter pump (Varian StarCell, $24\,\mathrm{l/s}$) as the final stage of vacuum pumping achieves a pressure below $10^{-11}\,\mathrm{mbar}$ providing a trap lifetime of several seconds [17].

The optics is located outside of the vacuum chamber as shown in Fig. 2.4. It consists of a commercial objective (Linos HALO) with a numerical aperture of 0.38 and a working distance of $30\,\mathrm{mm}$ (objective 1). It serves for focusing the light of the dipole trap into the glass cell and for collecting the light of the atomic fluorescence. The field of view of the observation objective is exactly overlapped with the focus of the dipole trap which allows to efficiently collect the light coming from trapped atoms. This light is then coupled into a single mode optical fiber (length: $5\,\mathrm{m}$) and guided to single-photon counting avalanche photodiodes (APDs). The light of the dipole trap is coupled into the same objective by means of a dichroic mirror. At the opposite side of the glass cell the light is collected by an identical objective (objective 2) and focused onto a photodiode used for stabilization of its intensity. This objective also serves for focusing the STIRAP beam for atomic state detection (see section

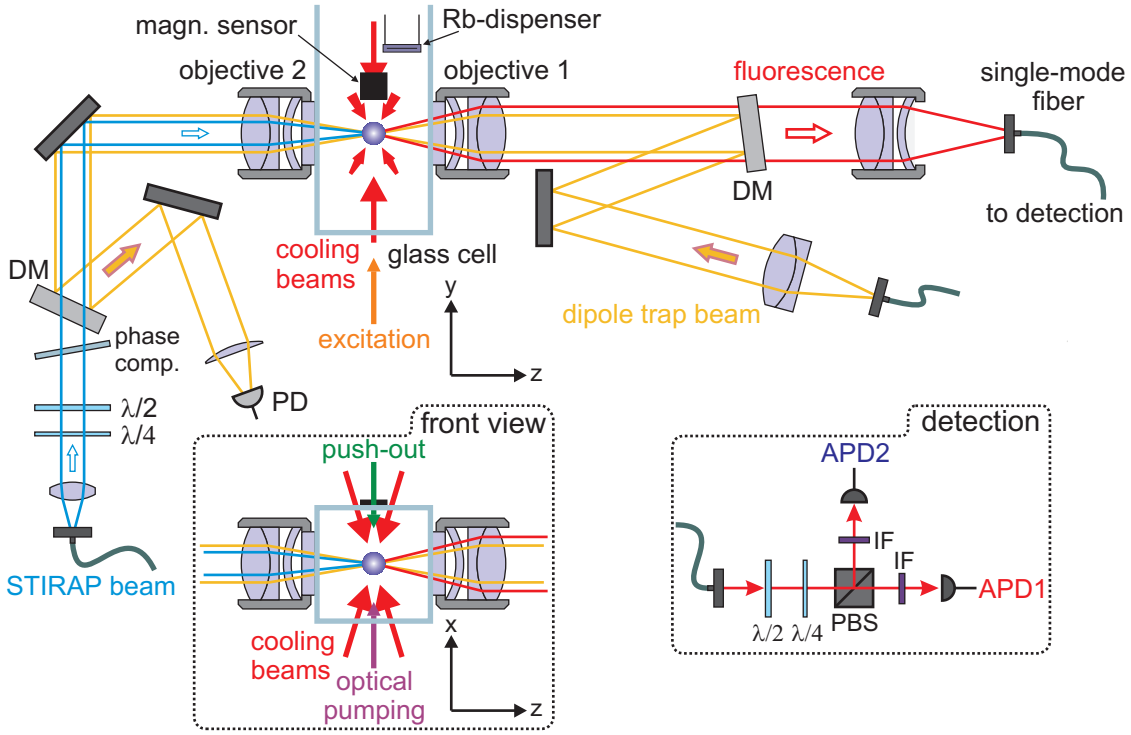

Figure 2.4.: Schematic of the main experimental setup. Shown is the top view of the glass cell and the optics. The insets show the front view of the glass cell and the photon detection part. DM - dichroic mirror; PD - photodiode; APD - avalanche photodiode; IF - interference (here band-pass) filter; PBS - polarizing beam splitter; $\lambda/2$, $\lambda/4$ - half- and quarterwave plates.

2.6.2) onto the atom.

2.4.3. Optical dipole trap

The dipole trap is operated at the wavelength of $856\,\mathrm{nm}$ having a red detuning of $76\,\mathrm{nm}$ from the $D2$-line ($780\,\mathrm{nm}$) and $61\,\mathrm{nm}$ from the $D1$-line ($795\,\mathrm{nm}$). The light for the dipole trap is generated by a single frequency mode laser diode which achieves a maximum power of $200\,\mathrm{mW}$. The beam is first coupled into a single-mode optical fiber in order to achieve a pure Gaussian mode profile at the output. The trap beam is focused to a waist $w_0 = 3.5\,\mu\mathrm{m}$ with a Rayleigh range $z_R = 45\,\mu\mathrm{m}$. For a typical light power of $30\,\mathrm{mW}$ at the position of the trap this yields a depth of the potential $U_0 = 0.65\,\mathrm{mK}$ corresponding to the ground state light-shift of $13.6\,\mathrm{MHz}$. The corresponding radial and axial trap frequencies are

$$\begin{aligned} \omega_r &= \sqrt{\frac{4U_0}{m \cdot w_0^2}} = 2\pi \cdot 22.7\,\mathrm{kHz} \\ \omega_z &= \sqrt{\frac{2U_0}{m \cdot z_R^2}} = 2\pi \cdot 1.25\,\mathrm{kHz} \end{aligned} \tag{2.3}$$

respectively. In order to keep the depth of the potential constant, the intensity of the trapping beam is continuously monitored by a photodiode (Fig. 2.4) and stabilized by means of a feedback loop.

The dipole trap is conservative, therefore it can not capture atoms directly from the background gas. For loading of the trap a friction force is necessary which is able to remove the excess kinetic energy of the atom when it enters the potential well. Additionally, for efficient loading of the microscopic

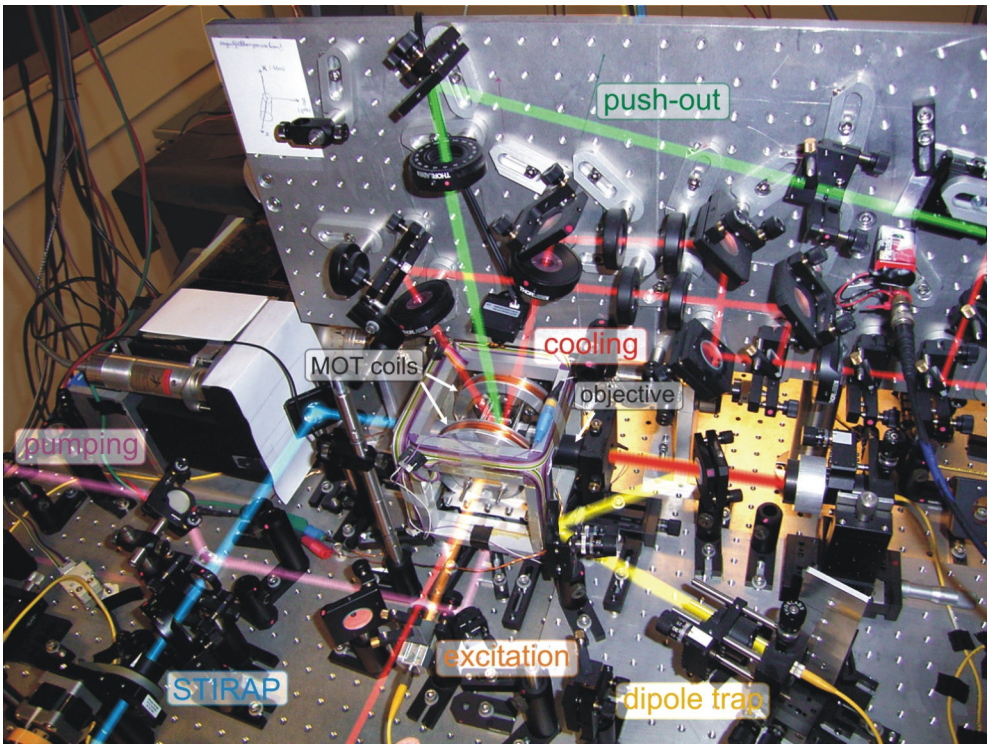

Figure 2.5.: Picture of the main experimental setup.

trap volume it is necessary to provide a high density of cold atoms ($E_{thermal} < U_0$). Both tasks can be achieved with the help of laser cooling and a magneto-optical trap as described in the following.

2.4.4. Magneto-optical trap and loading of atoms

In order to create locally a high density of cold atoms we use a magneto-optical trap (MOT). The MOT is created by overlapping three pairs of counter-propagating beams which are red detuned with respect to an atomic transition. The Doppler effect leads in this case to a predominant scattering of light from the direction opposite to the motion of the atom [30, 31]. This results in slowing, i.e. cooling of atoms. A proper choice of the polarization of the counter-propagating beams together with an applied magnetic quadrupole field leads also to a spatial confinement of the atoms [32]. To achieve continuous cooling the laser is tuned to the red of the closed atomic transition[1] $5^2S_{1/2}\,|F=2\rangle \rightarrow 5^2P_{3/2}\,|F'=3\rangle$.

The quadrupole magnetic field for the magneto-optical trap is produced by a pair of coils in anti-Helmholtz configuration. These are operated at $0.5..1\,\mathrm{A}$, providing gradients of magnetic field of typically $2.5..5\,\mathrm{G/cm}$. Together with three pairs of counter-propagating cooling beams (see Fig. 2.4) we hereby create a cloud of Rb atoms with a diameter of about $1\,\mathrm{mm}$. The cloud contains several ten thousand atoms at a temperature of about $105\,\mu\mathrm{K}$ [18]. This temperature is below the limit achievable

[1] Closed transition means that from the $5^2P_{3/2}\,|F'=3\rangle$ level the atom should always decay back to the $5^2S_{1/2}\,|F=2\rangle$ level and thus stay in the cooling cycle. This is not exactly true as there is a small probability of excitation of the $5^2P_{3/2}\,|F'=2\rangle$ level from which a decay to $5^2S_{1/2}\,|F=1\rangle$ is possible. If this happens, the atom stops scattering light and therefore cooling breaks down. To avoid this the atom is put back into the cooling cycle by applying an additional "repump" laser tuned to the $5^2S_{1/2}\,|F=1\rangle \rightarrow 5^2P_{3/2}\,|F'=2\rangle$ transition.

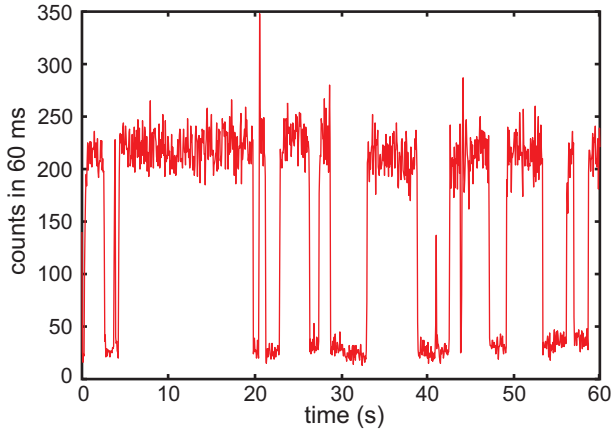

Figure 2.6.: Fluorescence observed from the single-atom dipole trap loaded from a MOT and continuously illuminated by cooling light. In this selected trace a two-atom loading event can be observed where both atoms stay in the trap long enough that an increased fluorescence level can be detected (peak near $t = 21\,\mathrm{s}$).

with ordinary laser cooling (Doppler limit for $^{87}\mathrm{Rb}$ is $146\,\mu\mathrm{K}$) due to the effect of polarization-gradient cooling [33].

The loading of atoms into the dipole trap is accomplished by operating the magneto-optical trap and the optical dipole trap simultaneously. The position of the MOT is adjusted such that its center coincides with the focus of the dipole trap. In this case the MOT provides a high local density of cold atoms and a friction force (cooling) which allows to capture atoms in the conservative dipole potential. Fig. 2.6 shows a typical trace of fluorescence coming from the dipole trap during its loading from the MOT. The loading process is supervised by a computer control program which continuously records the counts from the photon detectors and adjusts the experimental parameters. After a step-like increase in fluorescence is detected, indicating the presence of the atom in the dipole trap, the computer control switches off the quadrupole fields of the MOT. The atom is further illuminated by the cooling light until it is lost from the trap. We observe a lifetime of $2..4\,\mathrm{s}$ depending on cooling parameters. Under real experimental conditions, where different steps of optical pumping, excitation and cooling are applied, the lifetime reduces to $1.5..2\,\mathrm{s}$ which is still completely sufficient for all experiments.

It is important to note that the trap captures only one atom at a time. This "collisional blockade" effect [34] is based on light-induced two body collisions which prevent loading of more than one atom in presence of cooling light. Here two excited Rb atoms attract each other in a long-range molecule potential which after spontaneous emission converts a part of the absorbed energy into kinetic energy. Both atoms thereby leave the trap typically within few milliseconds. For a single focused Gaussian beam trap this effect can be observed for trap waists below $4\,\mu\mathrm{m}$. For our experiment this mechanism is very convenient since we do not have to apply additional effort to ensure the presence of only a single atom in the trap. This effect was also verified by measuring the photon statistics in a Hanburry-Brown-Twiss arrangement [35].

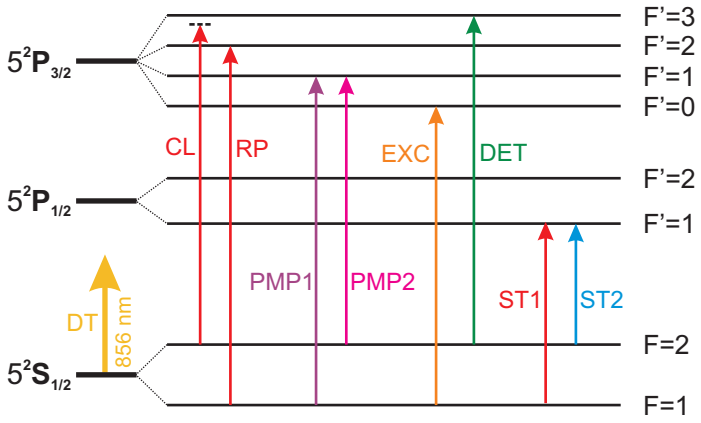

Figure 2.7.: Overview of laser frequencies used in the experiment. All frequencies are derived from diode lasers by means of acousto-optical modulators. DT - dipole trap; CL - cooling laser; RP - repump laser; PMP1, PMP2 - optical pumping; EXC - excitation for entanglement generation; DET - hyperfine state detection push-out beam; ST1, ST2 - STIRAP.

2.4.5. Lasers

The laser frequencies used in the experiment are generated by 6 diode lasers. Except for the dipole trap laser, all of them are set up with an external diffraction grating in Littrow configuration. The stabilization of the frequency is performed either directly to an atomic resonance line via FM saturation spectroscopy[41, 42] in a Rb gas cell, or indirectly to an already stabilized laser using the frequency offset lock technique. We achieve a laser stability of about 700 kHz short-term (coming from the fast phase noise of the laser diode) and about 2 MHz long-term. The long-term stability is limited by temperature drifts of the laser diodes and of the stabilizing electronics. Our laboratory is equipped with a common split air conditioner keeping the temperature constant to $1°..2°$C. Altogether the stability of the lasers allows measurement times without human interrogation of up to 24 hours.

The exact frequencies and pulse shapes are generated by means of acousto-optical modulators (AOMs). They allow to shift the frequency of the incoming light by up to ± 300 MHz and to switch it on and off within ~ 10 ns. Most of the AOMs are set up in the so-called double-pass configuration where the light is sent through the modulator twice. This allows to achieve an isolation (suppression of residual light power) of better than 100 dB. The control of the AOMs on the slow timescale ($\sim$ ms) is performed by a computer. For the time-critical parts of the experimental sequence a programmable pattern generator [43] is used, which has a time resolution of 20 ns.

2.4.6. Photon detection

The detection is performed by two single-photon counting modules (Perkin-Elmer SPCM AQR-14 Si avalanche photodiodes with a circuit for active avalanche quenching). They have a quantum efficiency of 0.6 and dark count rates of 70..100 cps. The detectors are protected from unwanted light by band-pass interference filters. The overall efficiency for detection of the emitted photons is composed of the collection efficiency of the objective and coupling into the single-mode fiber $\eta_{coupl} \approx 0.63\%$, transmission of the optical components (glass cell, objective, dichroic mirror, fiber, interference filters) $\eta_{trans} \approx 53\%$ and finally detection efficiency of the APDs $\eta_{det} \approx 60\%$. This gives altogether $\eta \approx 0.2\%$. For our cooling parameters the fluorescence of a single atom in the dipole trap produces a count

rate of $\sim 3200\,\mathrm{cps}$ on the detectors (Fig. 2.6) which allows to detect the presence of an atom within few tens of ms.

In order to analyze the polarization of the emitted photons we use a polarizing beam-splitter (PBS), see inset in Fig. 2.4. The selection of the photonic measurement basis is done by means of a halfwave- and a quarterwave-plates mounted on motorized precision rotation stages. For a faithful analysis it is crucial to preserve the polarization of the photon on its way to the detectors. However, the birefringence of certain elements - the glass-cell, the dichroic mirror and the optical fiber changes the polarization depending on mechanical stress and ambient temperature. In order to compensate these effects, reference light of two complementary polarizations (V and $+45^\circ$) was sent through the glass cell and coupled into the collection objective. By using a manual fiber polarization controller the output polarization was adjusted to be equal to the input (extinction of the wrong polarization of $1:1000$ and better). For the short ($5\,\mathrm{m}$) optical fiber which is fixed to the optical table and stable temperature conditions in the laboratory this procedure has to be repeated once in several weeks. An automatic version of this procedure, which enables us to distribute entanglement over a $300\,\mathrm{m}$ long optical fiber, is presented in chapter 5.

2.5. Generation of atom-photon entanglement

After the atom has been loaded into the dipole trap, the experimental entanglement sequence is initialized. It consists of three steps.

1. **Preparation of the initial state.** For efficient optical excitation the atom is first prepared in the $|F=1, m_F=0\rangle$ state by optical pumping, Fig. 2.8(a). This is done by applying π-polarized light resonant with the $F=1 \rightarrow F'=1$ transition (pumping1), for which the transition $|F=1, m_F=0\rangle \rightarrow |F'=1, m_{F'}=0\rangle$ is forbidden. In order to empty the $F=2$ state we additionally apply light which is resonant with the $F=2 \rightarrow F'=1$ transition (pumping2) together with cooling light. For this light configuration the population gets "trapped" [36] in the dark state $|F=1, m_F=0\rangle$. This procedure has an efficiency of about 65% mainly limited by polarization errors and residual magnetic fields. The time required for the optical pumping depends on the initial state of the atom. During repeated excitation cycles the population stays in $F=1$ level and is efficiently pumped into $|F=1, m_F=0\rangle$ state within about $2.6\,\mu\mathrm{s}$. After the cooling cycle, however, the population is in the $F=2$ level. Due to the presence of two dark states for the pumping2 light this level can not be completely emptied by this light alone. In order to empty the dark states, cooling light is used in addition, allowing to pump into the $|F=1, m_F=0\rangle$ state in $4.4\,\mu\mathrm{s}$.

2. **Optical Excitation.** The atom is excited into the $|F'=0, m_{F'}=0\rangle$ state by an optical π-pulse, Fig. 2.8(b). For this purpose a $20\,\mathrm{ns}$ long pulse resonant with the $|F=1, m_F=0\rangle \rightarrow |F'=0, m_{F'}=0\rangle$ transition is applied. Its intensity is adjusted such that within its duration the atom undergoes half of a Rabi-cycle and ends up in the $|F'=0, m_{F'}=0\rangle$ state. The efficiency of this process is about 95%.

3. **Observation of the spontaneously emitted photon.** The excited state has a lifetime of $26\,\mathrm{ns}$ and decays emitting a photon thereby generating an entangled atom-photon state, as was described in section 2.3. Figure 2.8(c) shows the time histogram of detected photons. Clearly visible is the excitation by the π-pulse followed by an exponential decay. The overall efficiency of detecting the emitted photon is given by the collection efficiency (about 0.2%) together with

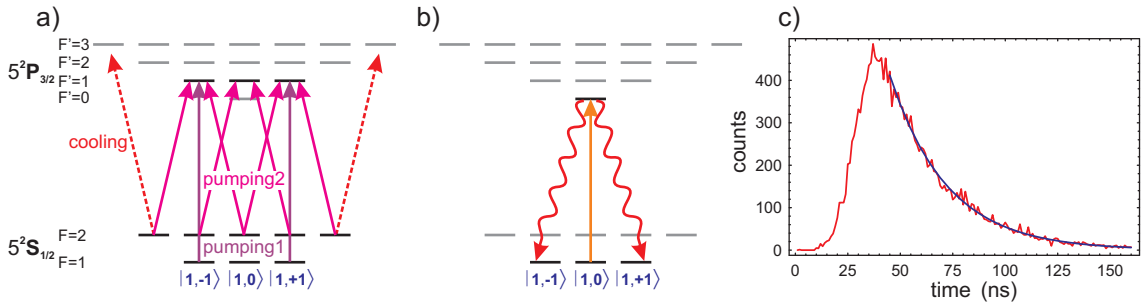

Figure 2.8.: The entanglement sequence. In the first step (a) the atom is prepared in the $|F = 1, m_F = 0\rangle$ state by optical pumping. This is done by applying two pumping lasers assisted by the cooling laser, the only dark state for this configuration is the desired state. After optical excitation (b), the spontaneously emitted photon is detected. c) Time histogram of spontaneously emitted photons. The exponential fit (blue curve) gives a lifetime of $27.2\,\mathrm{ns}$, which is in a good agreement with the theoretical value of $26.2\,\mathrm{ns}$ of the $D2$ transition.

the efficiency of preparation of the initial state and the excitation (about 60%). Altogether the efficiency to detect a single photon from the entanglement process is $\eta = 0.12\%$.

The polarization state of the photon can be conveniently analyzed by means of a polarizing beam splitter (PBS) together with a halfwave-plate and a quarterwave-plate. It allows to perform a projective measurement in any basis. To achieve the same ability for the atomic spin state, a rather elaborate method is required, which is described in section 2.6.

2.6. Detection of the atomic state

In order to analyze the entanglement of the atom with the photon or to perform any quantum-information protocol on the atom one needs the ability to analyze the atomic qubit in any desired measurement basis. In our case we have to distinguish between selected superpositions of the states in the $\{|1,-1\rangle, |1,+1\rangle\}$ subspace with high efficiency. Conventional spectroscopy as, e.g., the shelving method known from experiments with trapped ions [37, 38] is not applicable here since it relies on scattering of photons on a closed transition. For this procedure the light has to be applied from a defined direction thereby inducing a directed force. The relatively deep potential of an ion trap is sufficient to prevent the ion from being pushed out during the detection process. However, in the much weaker potential of a dipole trap the light pressure leads to the loss of the atom before it can scatter sufficient amount of photons for detection. Thus a novel detection method had to be developed which is compatible with the shallow potential of a dipole trap.

The fact that resonant light pressure pushes the atom out of the trap can be applied for an efficient way to distinguish two different hyperfine levels, here $F = 1$ and $F = 2$ (see section 2.6.1). In order to adapt this technique for our experiment we first need a way to transfer a certain superposition from our analyzed subspace of $F = 1$ to $F = 2$. This can be done very efficiently using the so-called tripod STIRAP technique [39, 40, 16] which is described in section 2.6.2.

The whole state-detection procedure is a two-step process. In the first step a selected superposition of the qubit states is transferred to the $F = 2$ level while the orthogonal superposition stays in $F = 1$.

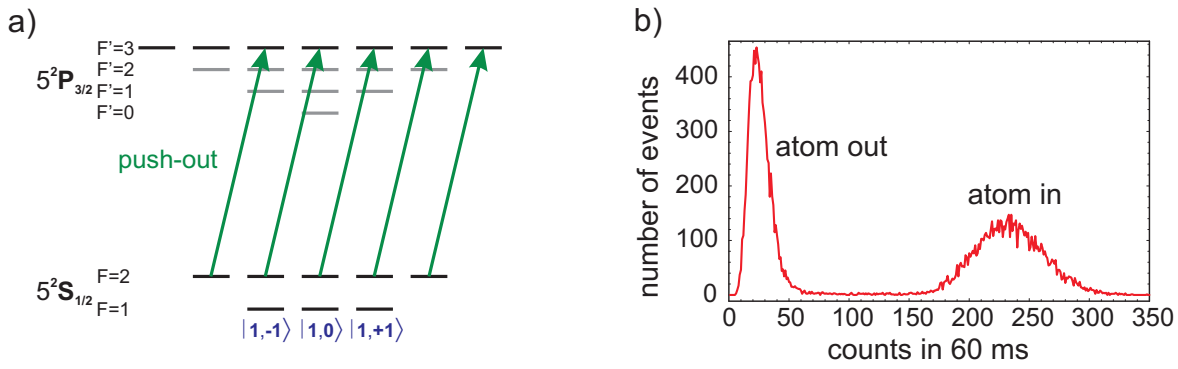

Figure 2.9.: Hyperfine state detection. By applying light resonant to $F = 2 \rightarrow F' = 3$ transition the population in $F = 2$ level is pushed out of the trap (a). In the subsequent illumination of the trap with cooling light it is possible to distinguish whether the atom has left the trap or not by counting fluorescence photons (b).

In the second step the population in $F = 2$ is removed from the trap. By observing the fluorescence from the trap it is then possible to decide whether the atom was removed or not, and thereby to infer in which superposition it was. In the following I will describe the state detection method in more detail.

2.6.1. Hyperfine level detection

The hyperfine level detection procedure uses resonant light pressure in order to remove population in the $F = 2$ level out of the trap. It consists of a $10\,\mu$s long σ^+- polarized "detection pulse" which is resonant with the $F = 2 \rightarrow F' = 3$ transition, Fig. 2.9(a). The atom in the $F = 2$ state scatters light on this closed transition and is pushed out of the trap. At the same time the atom in the $F = 1$ level does not scatter because of the large detuning ($6.8\,$GHz) and thus remains in the trap. After the pulse the cooling and repump light of the MOT is switched on and the presence or absence of the atom is verified. Fig. 2.9(b) shows the histogram of fluorescence collected in $60\,$ms after this procedure. The two events "atom out of the trap" and "atom still in the trap" are clearly separated. However, there is a final probability for the atom which survived the push-out to get lost during the fluorescence detection due to background collisions, etc. In order to reduce the errors of discrimination arising from such losses, the fluorescence collection time is reduced to $20 - 25\,$ms. The discrimination accuracies (i.e. the probabilities to identify the $F = 1$ and $F = 2$ levels correctly) were determined [18] to be

$$\begin{aligned} F = 1\text{:} &\ \geq 96.3 \pm 0.2\% \\ F = 2\text{:} &\ \geq 99.3 \pm 0.1\% \end{aligned} \tag{2.4}$$

2.6.2. STIRAP

Given an efficient method for discrimination of the hyperfine levels $F = 1$ and $F = 2$, the remaining problem is to distinguish between arbitrary superpositions in the qubit subspace $\{|1,-1\rangle, |1,+1\rangle\}$. In particular a method is needed which transfers a selected superposition to the $F = 2$ level without affecting the other one. This task can be performed by using the so-called tripod STIRAP technique, which will be presented in the following.

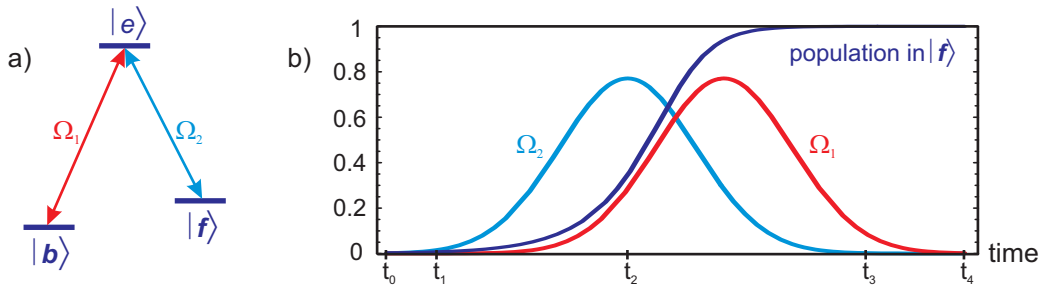

Figure 2.10.: Principle of STIRAP. a) The initial state $|b\rangle$ and the final state $|f\rangle$ are coupled to an excited state $|e\rangle$ by two fields with Rabi frequencies Ω_1 (historically called pump) and Ω_2 (Stokes). b) By variation of the Rabi frequencies the population is adiabatically transferred from $|b\rangle$ to $|f\rangle$.

STIRAP (stimulated Raman adiabatic passage) is a method for efficient transfer of population between two states. It can be explained on a 3-level system with two ground states $|b\rangle$, $|f\rangle$ and one exited state $|e\rangle$, see Fig. 2.10(a). The levels are coupled resonantly by two light fields $STIRAP1$ and $STIRAP2$ with respective Rabi frequencies Ω_1 and Ω_2. The Hamiltonian in the interaction picture (without spontaneous decay) is given in the $\{|b\rangle, |f\rangle, |e\rangle\}$-basis by

$$\widehat{H}_{int} = \frac{\hbar}{2}\begin{pmatrix} 0 & 0 & \Omega_1 \\ 0 & 0 & e^{i\beta}\Omega_2 \\ \Omega_1 & e^{-i\beta}\Omega_2 & 0 \end{pmatrix}$$

where β is the starting phase between the two fields. For given values of the Rabi frequencies, the eigenstates of the interacting system are

$$\begin{aligned} |\Psi_1\rangle &= \tfrac{1}{\sqrt{\Omega_1^2+\Omega_2^2}}\left(\Omega_2|b\rangle - \Omega_1 e^{i\beta}|f\rangle\right) \\ |\Psi_2\rangle &= \tfrac{1}{\sqrt{2}\sqrt{\Omega_1^2+\Omega_2^2}}\left(\Omega_1|b\rangle + e^{i\beta}\Omega_2|f\rangle + \sqrt{\Omega_1^2+\Omega_2^2}|e\rangle\right) \\ |\Psi_3\rangle &= \tfrac{1}{\sqrt{2}\sqrt{\Omega_1^2+\Omega_2^2}}\left(\Omega_1|b\rangle + e^{i\beta}\Omega_2|f\rangle - \sqrt{\Omega_1^2+\Omega_2^2}|e\rangle\right) \end{aligned}$$

The state $|\Psi_1\rangle$ is especially interesting because it contains no contribution from the exited state $|e\rangle$, therefore it is not affected by spontaneous emission. The ratio of populations of $|b\rangle$ and $|f\rangle$ in $|\Psi_1\rangle$ is equal to $\frac{\Omega_1^2}{\Omega_2^2}$.

The adiabatic theorem of quantum mechanics states that if a system is initially in an eigenstate of a Hamiltonian and if this Hamiltonian changes slowly compared to the dynamics of the system (given in our case by Ω_1 and Ω_2) then the system will follow the change of the eigenstate. By tailoring the (time-dependent) Hamiltonian in a proper way it becomes possible to steer the system between different states with very high efficiency. In our case one has to adiabatically vary the ratio $\frac{\Omega_1}{\Omega_2}$ between 0 and ∞.

We start with the system in the initial state $|b\rangle$ and both coupling fields off, i.e. $\Omega_1(t_0) = 0 = \Omega_2(t_0)$ (Fig. 2.10(b)). Then the second field Ω_2 is adiabatically switched on while Ω_1 stays zero, therefore $|\Psi_1\rangle(t_1) = |b\rangle$. In the next phase the first field is also switched on, $|\Psi_1\rangle$ becomes a superposition of $|b\rangle$ and $|f\rangle$ with the amplitude ratio $\frac{\Omega_1}{\Omega_2}$. At the time t_2 Ω_2 reaches its maximum while Ω_1 continues growing. By adiabatically reducing Ω_2 to zero this ratio becomes infinity, i.e. $|\Psi_1\rangle(t_3) = |f\rangle$. Finally

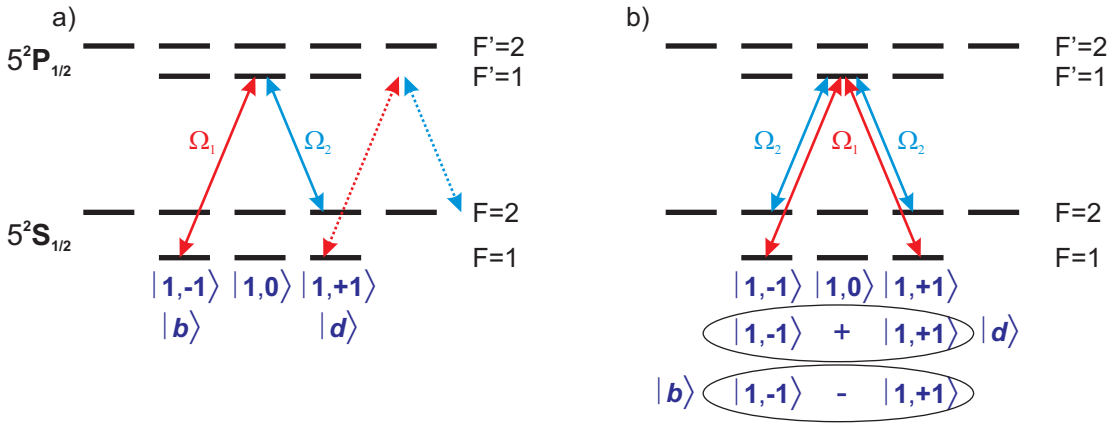

Figure 2.11.: State selectivity of the STIRAP process for the cases of circular polarization (a) and linear polarization (b) of the STIRAP light. For each polarization of the applied STIRAP light there exist a bright state $|b\rangle$, which is transferred, and a dark state $|d\rangle$, whose transfer is forbidden.

Ω_1 can also be switched off, the system stays in $|f\rangle$. By these means the population is adiabatically transferred from $|b\rangle$ to $|f\rangle$. Note that as long as the adiabaticity condition is satisfied, the state $|e\rangle$ only mediates the coupling but is not populated during this process. Also the initial phase β has no effect (except a phase in the eigenstates), however it must remain constant during the process, i.e. the two fields have to be coherent for the duration of the transfer. Under ideal conditions the transfer efficiency is equal to unity and is not influenced by spontaneous decay of the state $|e\rangle$.

2.6.3. State selectivity

In order to select the measurement basis of our qubit, the transferring process has to distinguish between superpositions of states in the $\{|1,-1\rangle, |1,+1\rangle\}$ space. This can be achieved by using selection rules of atomic transitions. Any polarization of the $STIRAP1$ light field can be expressed as a superposition of σ^+ and σ^- polarization. There exists a superposition of $|1,-1\rangle$ and $|1,+1\rangle$ states which couples to this field, this state is called a bright state $|b\rangle$. The orthogonal superposition does not couple to the field and is called a dark state $|d\rangle$. Under these conditions the bright state $|b\rangle$ will evolve as described in the previous section (i.e. it will be transferred) while the dark state $|d\rangle$ ideally stays unchanged (Fig. 2.11).

For the state transfer we use the $|F'=1, m_{F'}=0\rangle$ state of $5^2P_{1/2}$ as the mediating upper state $|e\rangle$. The reason to use this state is the simplicity of the $5^2P_{1/2}$ manifold which has only two levels with large separation of 817 MHz compared to the four levels with smaller separations of $5^2P_{3/2}$ (see also Fig. 2.1), this allows to reduce unwanted coupling via different upper levels. The $STIRAP1$ field is resonant with the $|F=1\rangle \rightarrow |F'=1\rangle$ transition and the $STIRAP2$ field is resonant with the $|F=2\rangle \rightarrow |F'=1\rangle$ transition.

First we consider the case where the field $STIRAP1$ giving Ω_1 is σ^+-polarized, Fig. 2.11(a). Here it is easy to see that $|d\rangle = |1,+1\rangle$ and $|b\rangle = |1,-1\rangle$. In the second case shown in Fig. 2.11(b) the $STIRAP1$ field is polarized as $H = \frac{1}{\sqrt{2}}(\sigma^+ + \sigma^-)$ (tripod STIRAP). Due to the fact that the transition amplitudes (Clebsch-Gordan coefficients) of $|1,-1\rangle \rightarrow |1',0\rangle$ and $|1,+1\rangle \rightarrow |1',0\rangle$ are of opposite sign, in this case we get $|d\rangle = \frac{1}{\sqrt{2}}(|1,-1\rangle + |1,+1\rangle)$ and $|b\rangle = \frac{1}{\sqrt{2}}(|1,-1\rangle - |1,+1\rangle)$.

Generally, for a given polarization of the $STIRAP1$ field

$$\mathbf{P} = \cos(\alpha)\sigma^{+} + e^{i\phi}\sin(\alpha)\sigma^{-} \tag{2.5}$$

we can write the dark state as ([18])

$$|\Psi_D\rangle = \cos(\alpha)\,|1,+1\rangle + e^{i\phi}\sin(\alpha)\,|1,-1\rangle\,. \tag{2.6}$$

In order to complete the picture it has to be added that the population in the $|1,0\rangle$ state (if present) is transferred to $|F=2\rangle$ for any polarization of the form (2.5), as the state $|1,0\rangle$ is only dark for π-polarization. Since the population in $|F=2\rangle$ will be removed from the trap in the next step, the whole procedure works as projection onto the dark state $|\Psi_D\rangle$. See also appendix A for the definitions of polarizations and analyzed states.

Off-resonant transitions

So far we have considered only resonant coupling to the $5^2P_{1/2}$, $|F'=1\rangle$ hyperfine level during the STIRAP process. Unfortunately, off-resonant coupling via the $|F'=2\rangle$ level is present as well. The transition amplitudes $|1,-1\rangle \rightarrow |2',0\rangle$ and $|1,+1\rangle \rightarrow |2',0\rangle$ in this case have the same sign (in contrast to the opposite sign of $|1,-1\rangle \rightarrow |1',0\rangle$ and $|1,+1\rangle \rightarrow |1',0\rangle$). This allows the transfer of the state $|d\rangle$ while forbidding the transfer of the state $|b\rangle$. Although this coupling is weaker than the resonant coupling of the $|b\rangle$ state, it can still lead to a considerable transfer efficiency as will be shown in the next section. By properly selecting the relative polarizations of $STIRAP1$ and $STIRAP2$ fields it is nevertheless possible to suppress the off-resonant two-photon transition [18]. The remaining error is then due to the imperfect preparation of the polarization of the two fields.

2.6.4. Technical realization of the STIRAP process

In order to generate the $STIRAP1$ and $STIRAP2$ fields we use two independent diode lasers spectroscopically stabilized to the corresponding transitions (see also section 2.4.5). The short-term relative stability is of the order of $700\,\mathrm{kHz}$ corresponding to a time of $\frac{1}{2\pi\cdot 700\,\mathrm{KHz}} = 227\,\mathrm{ns}$ during which the relative phase β can be considered fixed. As a well-defined phase dependence between the two fields is needed for the duration of the transfer process, the pulse sequence has to be on a much shorter time scale.

We have chosen the pulse length of $30..40\,\mathrm{ns}$. Each pulse is formed by an AOM in double-pass configuration allowing to switch the pulse on or off in about $10\,\mathrm{ns}$. The form of the rising and falling edges is smoothened by appropriate shaping of the electric signal which controls the AOMs with a low-pass filter. Fig. 2.12(a) shows the measured intensity of the pulses. The relative intensities of the pulses are chosen such that the resulting maximal Rabi frequencies are approximately equal.

Then the two pulses are combined on a beam splitter, guided through a single-mode optical fiber, and sent through an additional AOM. This step is necessary to get a sufficient on/off switching ratio for the STIRAP field, which has up to 10000 times the saturation intensity I_{sat}. The high intensity is needed in order to fulfill the adiabaticity condition. After that the pulse is coupled again into a single-mode optical fiber and guided to the main experiment (see Fig. 2.4). There it passes a quarter-wave plate and a half-wave plate in order to prepare the polarization and thus to select the atomic measurement basis. A phase compensation plate is used to eliminate the phase between H and V polarization arising upon reflection on the mirror and transmission through the dichroic mirror. Finally the STIRAP pulse is focused onto the atom with a Gaussian waist of $9\,\mu\mathrm{m}$.

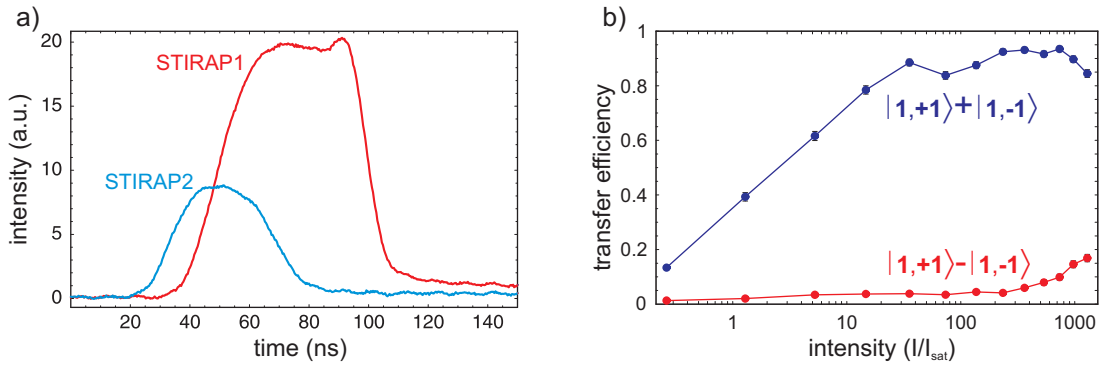

Figure 2.12.: a) The experimental STIRAP pulse sequence - intensities of $STIRAP1$ and $STIRAP2$ beams measured by a fast photodiode. b) The transfer efficiency of the STIRAP process for the bright state $\frac{1}{\sqrt{2}}(|1,+1\rangle + |1,-1\rangle)$ (blue curve) and the dark state $\frac{1}{\sqrt{2}}(|1,+1\rangle - |1,-1\rangle)$ (red curve). The polarization of both STIRAP lasers in this measurement is $V = \frac{i}{\sqrt{2}}(\sigma^+ - \sigma^-)$. The non-vanishing probability for the transfer of the dark state is due to polarization errors which allow off-resonant coupling.

In order to test the STIRAP process the states $\frac{1}{\sqrt{2}}(|1,+1\rangle \pm |1,-1\rangle)$ were prepared and the transfer efficiency was measured as a function of the intensity of the STIRAP pulse. The polarization of both STIRAP fields was $V = \frac{i}{\sqrt{2}}(\sigma^+ - \sigma^-)$, giving $|d\rangle = \frac{1}{\sqrt{2}}(|1,+1\rangle - |1,-1\rangle)$ and $|b\rangle = \frac{1}{\sqrt{2}}(|1,+1\rangle + |1,-1\rangle)$. The result is shown in Fig. 2.12(b). The bright state is being fully transferred at few hundred I_{sat}, but unfortunately at such intensities the transfer efficiency of the dark state begins to increase. Since we are interested in the optimal discrimination of the two states, the working point is chosen such, that the difference in transfer efficiencies is the largest. At this point in Fig. 2.12(b) the transfer efficiencies are

$$\begin{aligned} bright\ state&: 95.9 \pm 1.0\% \\ dark\ state&: 7.6 \pm 1.0\% \end{aligned} \tag{2.7}$$

These values include the errors of the state preparation, as e.g. excitation of wrong states ($\sim 0.5\%$) and dark counts of the detectors ($\sim 1\%$) as well as the errors of the subsequent hyperfine level detection.

2.6.5. Detection accuracy and detection efficiency

Using the result (2.7) for the efficiencies of the STIRAP transfer process and correcting for errors in the preparation we determine the accuracy of the complete atomic state detection procedure (STIRAP and hyperfine level detection):

$$\begin{aligned} bright\ state&: \approx 96.9\% \\ dark\ state&: \approx 93.3\% \end{aligned} \tag{2.8}$$

This yields an average detection accuracy of 95.1%.

It has to be stressed once again that the populations of the atomic states are inferred from the binary result “atom in the trap” or “no atom the trap”. In the experiment we estimate the probability of the atom to be in a certain analyzed (dark) state by repeating the experiment many times. In each single

realization of the experiment the atomic state detection procedure either removes the atom from the trap (bright state) or not (dark state). After N repetitions this gives the relative frequency for the events "atom in the trap" $\frac{N_{in}}{N}$ and "atom out of the trap" $\frac{N_{out}}{N}$. From these frequencies we estimate the probability p_{in} for the event "atom in the trap" as $p_{in} = \frac{N_{in}}{N}$. This number is also the estimate of the probability for the atom to be in the analyzed (dark) state. The statistical error of this estimation can be calculated by taking the standard deviation of the Bernoulli experiment $\sigma = \sqrt{\frac{1}{N} p_{in}(1 - p_{in})}$.

The binary nature of the result in the experiment has an important implication for the efficiency of the atomic state detection procedure. Especially in the context of a Bell-experiment [3] it is necessary to compare it with detection of particles in the usual sense, e.g., of photons. For the detection of the polarization of a single photon with a polarizing beam-splitter and two detectors there are three possible results: "click in detector 1", "click in detector 2", "no click". The third answer, "no click" occurs due to the finite detection efficiency of the photodetectors (dark counts are not considered). This limits the possibility of a Bell-test as a detection efficiency of at least $\frac{2}{3}$ is required [8] in order to strictly rule out hidden-variable theories ("detection loophole").

In the case of our atomic state detection scheme, there are only two possible outcomes "atom out of the trap" and "atom still in the trap" and thus the *detection efficiency* is 100%. The answer given by the detection procedure can be wrong - due to imperfections in the STIRAP and push-out procedure the *detection accuracy* is about 95.1% - but the answer is always given. In the picture of photon detection it can be compared to an imperfect PBS together with two perfect detectors. The limiting factor for the Bell-test in this case is therefore only the detection accuracy of the entangled state together with the requirement of strict locality conditions.

2.7. Experimental results

After having introduced all principal building blocks necessary for the experimental generation and detection of atom-photon entanglement I will present the whole experimental procedure together with the characterization of the entangled state.

2.7.1. Experimental sequence

The complete experimental sequence looks as following:

1. **Loading of the dipole trap.** At this stage the lasers and magnetic fields of the MOT are switched on and the computer control program continuously observes the fluorescence from the dipole trap (see also Fig. 2.6). When an atom enters the trap, the fluorescence value (i.e. number of counts) increases, which is detected by the control program. Then the MOT lasers and magnetic coils are switched off.

2. **Repeated preparation and excitation.** This sequence consists of $4.4\,\mu$s optical pumping into the $|F = 1, m_F = 0\rangle$ state, followed by an optical π-pulse into $|F' = 0, m_{F'} = 0\rangle$ (see Sec. 2.5). After excitation a single photon is expected within a time-window of $80\,$ns. The preparation-excitation cycle is repeated until a photon is detected. Since pumping and excitation lead to heating of the atom, $200\,\mu$s of laser cooling has to be performed after every 20 preparation-excitation trials. The whole process is controlled by a pattern generator [43] capable of switching lasers on a timescale of $20\,$ns as well as reacting on external events such as detection of the photon. A time-stamp unit [44] determines and stores the arrival times of all photons detected during the experiment together with synchronization signals marking the start

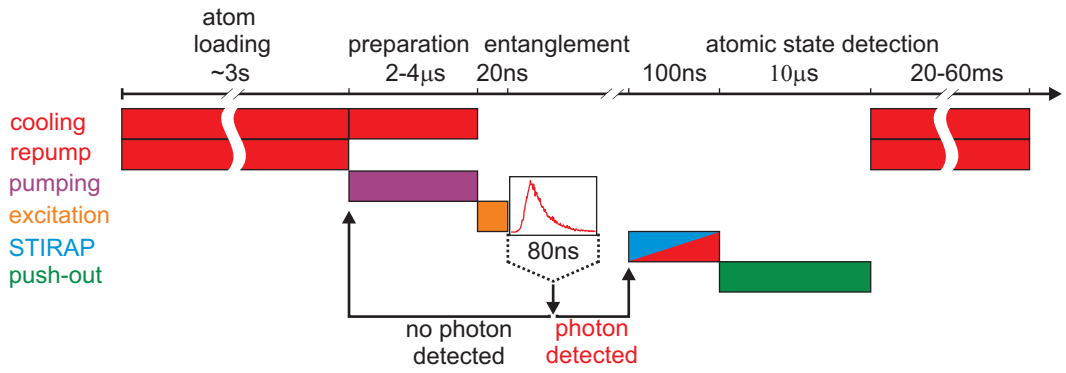

Figure 2.13.: Time diagram of the experimental sequence.

and end of a sequence. This allows later to identify in which detector the emitted photon arrived and which fluorescence counts correspond to the subsequent atomic state analysis.

3. **Detection of the emitted photon and analysis of the atomic state.** If the photon is detected during the defined time-window after excitation, the atomic state detection sequence is started (Sec. 2.6). During the detection a selected superposition of atomic qubit states is transferred to the $F = 2$ level by the STIRAP pulse sequence and then removed from the trap by the push-out laser. After that the cooling light is switched on and the fluorescence is observed in order to decide whether the atom is still in the trap or not, thereby determining the result of the atomic state analysis.

2.7.2. Atom-photon correlations

In a first experiment we analyze the correlations between the state of the detected photon with the state of the atom. For this purpose the atomic measurement basis is kept constant while the angle β of the halfwave-plate which defines the photonic measurement basis is rotated from $0°$ to $+90°$ in steps of $5.625°$. In order to understand the correlation curves we consider the states on which the photon is projected by the detection in $APD1$ and $APD2$ as a function of the angle β:

$$APD1\colon\ \cos(2\beta)\,|H\rangle - \sin(2\beta)\,|V\rangle = \cos(2\beta+\frac{\pi}{4})\,|P\rangle - \sin(2\beta+\frac{\pi}{4})\,|M\rangle$$
$$APD2\colon\ \sin(2\beta)\,|H\rangle + \cos(2\beta)\,|V\rangle = \sin(2\beta+\frac{\pi}{4})\,|P\rangle + \cos(2\beta+\frac{\pi}{4})\,|M\rangle$$

Inserting these into the entangled state from Eq. (A.1) we get the states on which the atom is projected by detection of the photon in $APD1$ and $APD2$:

$$APD1\colon\ -\sin(2\beta)\,|\downarrow\rangle_x + \cos(2\beta)\,|\uparrow\rangle_x = \cos(2\beta+\frac{\pi}{4})\,|\downarrow\rangle_y - \sin(2\beta+\frac{\pi}{4})\,|\uparrow\rangle_y$$
$$APD2\colon\ \cos(2\beta)\,|\downarrow\rangle_x + \sin(2\beta)\,|\uparrow\rangle_x = \sin(2\beta+\frac{\pi}{4})\,|\downarrow\rangle_y + \cos(2\beta+\frac{\pi}{4})\,|\uparrow\rangle_y$$

Therefore, we expect a $\sin(2\beta)^2$ and $\cos(2\beta)^2$ behavior of the population in $|\downarrow\rangle_x$ state if the photon is detected in $APD1$ or $APD2$ respectively. Fig. 2.14(a) shows the corresponding measurement, where the atomic state is projected onto $|\downarrow\rangle_x$ by using V polarization for the STIRAP pulse. The population of the analyzed atomic state clearly follows the expected sinusoidal form. Maximal correlation is

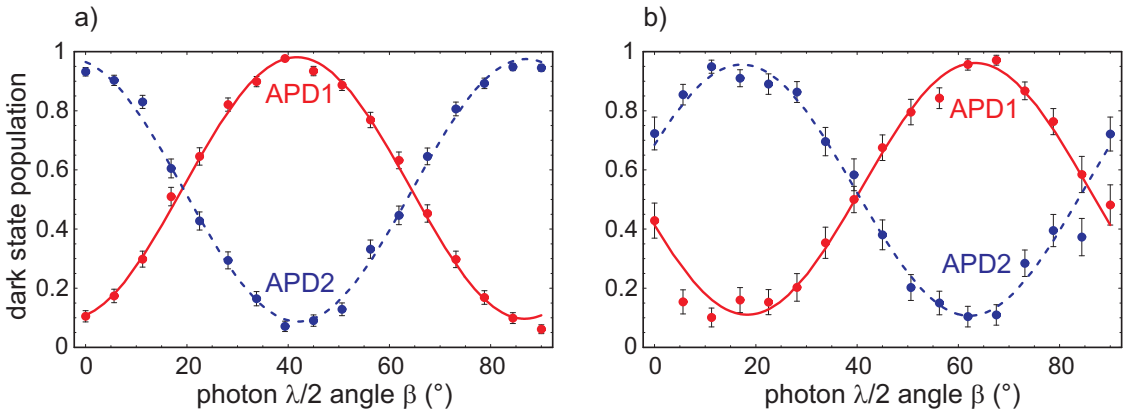

Figure 2.14.: Atom-photon correlations. Shown is the population of a selected atomic state depending on the polarization state of the photon. The halfwave plate defining the photonic measurement basis is rotated from 0° to +90°. The analyzed atomic state is $|\downarrow\rangle_x$ for (a) and $|\downarrow\rangle_y$ for (b).

observed at positions $\beta = 0°, +45°$ where the detection of a $|H\rangle$ or $|V\rangle$ photon projects the atom onto the states $|\downarrow\rangle_x$ and $|\uparrow\rangle_x$. Similarly, a $\cos(2\beta + \frac{\pi}{4})^2$ and $\sin(2\beta + \frac{\pi}{4})^2$ behavior is expected for the population in the $|\downarrow\rangle_y$ state, the corresponding measurement is shown in Fig. 2.14(b). Here the $|\downarrow\rangle_y$ state was analyzed by using STIRAP polarization $+45°$. Again strong correlations are observed, showing that the atom-photon state is entangled.

Sinusoidal functions were fitted separately onto the data for each detector. From the fit we infer the visibility (peak-to-peak amplitude) of the sine curve, as well as its phase. The mean visibility of these curves is $V_{\sigma_x} = 88.6 \pm 1.7\%$ in (a) and $V_{\sigma_y} = 84.9 \pm 3.5\%$ in (b). The additional phase-shift in Fig. 2.14(b) deviating from the expected $22.5°$ is due to the residual birefringence of the glass cell. It gives rise to an additional phase between H and V polarizations and can not be directly compensated by the procedure described in Sec. 2.4.6. This phase leads to a rotation of $\pm 45°$ polarization making it slightly elliptic. This is equivalent to a rotation of the basis of the atomic analysis which leads to the observed phase shift of $5.1°$ and a reduction of the visibility.

The presence of correlations in two complementary measurement bases proves that the system is in an entangled state. Disregarding the phase error in the σ_y- measurement and considering only its visibility (this is a worst-case assumption) we get a mean atom-photon visibility $V_{AP} = 86.8 \pm 2.8\%$. Assuming this visibility in all measurement bases (isotropy) we can estimate the fidelity of the entangled atom-photon state:

$$F_{AP} = \frac{1}{4} + \frac{3}{4} V_{AP} = 0.90 \pm 0.021. \tag{2.9}$$

2.7.3. Quantum state tomography of the entangled atom-photon state

The measurement of correlations between the photonic polarization and the atomic spin reveals information about the underlying atom-photon state. Since the state can in general be partially mixed due to unknown interaction with the environment, infidelity of detection, etc., full knowledge (in quantum mechanical sense) can only be acquired if the density matrix of the state is investigated.

The 4×4 density matrix of the atom-photon system has 15 independent real parameters. In App. B the framework is given which allows its reconstruction from values which are accessible in the

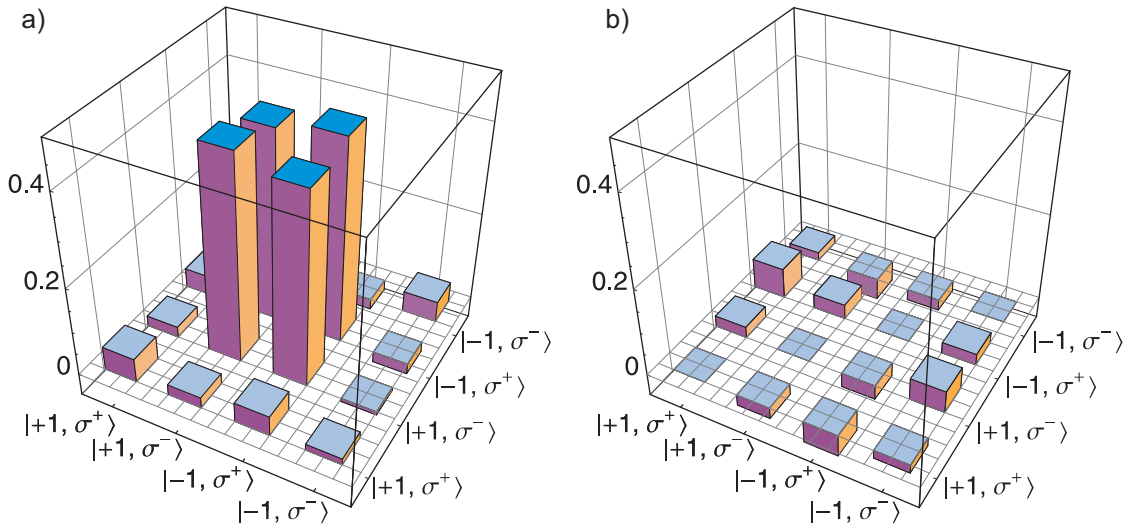

Figure 2.15.: Quantum tomography of the entangled atom-photon state. Shown is the real part (a) and the imaginary part (b) of the combined atom-photon density matrix.

experiment. The matrix can be determined by using the representation (B.3)

$$\hat{\rho} = \frac{1}{4} \sum_{j,k=0}^{3} \langle \hat{\sigma}_j \otimes \hat{\sigma}_k \rangle \cdot \hat{\sigma}_j \otimes \hat{\sigma}_k \tag{2.10}$$

where $\hat{\sigma}_j \otimes \hat{\sigma}_k$ are tensor products of Pauli operators and $\langle \hat{\sigma}_j \otimes \hat{\sigma}_k \rangle$ their expectation values, which are measured according to Eq. (B.4). This measurement requires 3×3 correlation measurements (3 conjugate bases on each side).

Fig. 2.15 shows the density matrix which was obtained by this method. The most important property of the real part of the matrix is that, first, mainly states $|1,-1\rangle|\sigma^+\rangle$ and $|1,+1\rangle|\sigma^-\rangle$ are populated, and, second, the coherences between these states are present. This clearly shows that the analyzed state is a coherent superposition of $|1,-1\rangle|\sigma^+\rangle$ and $|1,+1\rangle|\sigma^-\rangle$. The fidelity F of the entangled state is calculated as the overlap of the density matrix with the ideal state $|\Psi^+\rangle = \frac{1}{\sqrt{2}}(|1,-1\rangle|\sigma^+\rangle + |1,+1\rangle|\sigma^-\rangle)$ giving

$$F = \mathrm{trace}(\hat{\rho}\,|\Psi^+\rangle\langle\Psi^+|) = 0.87 \pm 0.01 \tag{2.11}$$

The reduced fidelity of this result compared to the one obtained from single correlation curves in Fig. 2.14 has two reasons. First, the atomic state analysis in the $|1,\pm1\rangle$ basis, which requires circularly polarized STIRAP, is slightly less accurate [18]. Second, this tomographic dataset was taken at an earlier stage of the experiment than the shown correlations. In the later measurements the fidelity was improved by using for the APDs interference filters with higher transmission (and therefore higher efficiency and smaller error due to dark counts), together with better compensation of magnetic fields.

2.7.4. Violation of Bell's inequality

The entangled state obtained in our experiment is well-suited for a test of theories with local hidden variables [1, 2] as opposed to quantum mechanics. In such an experiment one has a source of entangled

spin-$\frac{1}{2}$ particles which are sent to two independent observers. The spin σ of one particle is measured under an angle α (in the laboratory frame) and the spin of the other under an angle β. The possible outcomes of a single spin measurement are ± 1. Let $\langle \sigma_\alpha \otimes \sigma_\beta \rangle$ be the expectation value of a joint measurement on a pair. The Bell's inequality in CHSH formulation [3] states that for any theory with local hidden variables

$$S := |\langle \sigma_\alpha \otimes \sigma_\beta \rangle + \langle \sigma_{\alpha'} \otimes \sigma_\beta \rangle| + \left| \langle \sigma_\alpha \otimes \sigma_{\beta'} \rangle - \langle \sigma_{\alpha'} \otimes \sigma_{\beta'} \rangle \right| \leq 2 \tag{2.12}$$

holds for an arbitrary choice of $\alpha, \beta, \alpha', \beta'$. However, in quantum mechanics values larger than 2 are possible. For the specific choice $\alpha = 0°, \beta = -45°$, $\alpha' = 90°, \beta' = 45°$ a value of $S = 2\sqrt{2}$ is expected for a maximally entangled state[2].

In our experiment the Bell's inequality was evaluated giving $S = 2.44 \pm 0.05$ [18]. This result violates the classical threshold by more than 8 standard deviations. This is a strong indication against the local hidden variable theories, however, it is not a rigorous proof. In order to strictly rule out such theories it is necessary to fulfill two additional criteria. First, the detection efficiency on each side must exceed $\frac{2}{3}$ [8], this threshold increases in presence of background noise. This criterion is fulfilled for the atom but not for the photon ("detection loophole"). Second, it is necessary to achieve strict locality conditions, i.e. the measurement basis on each side has to be chosen randomly and independently from the other side and the measurement must be finished before any signal can reach the other side ("locality loophole"). No experiment so far has managed to close both loopholes. A possible way to achieve this is to use two entangled atoms at distance $d > c \cdot t_{det}$, where t_{det} is the detection time of the atomic state which is the overall duration of all operations described above. The entanglement can be achieved by generating an entangled atom-photon pair on each side and performing entanglement swapping by a Bell-state measurement on the photons [10]. The perfect detection efficiency possible with atoms together with locality conditions would then allow a loophole-free test of Bell's inequality.

2.8. Summary

In this chapter the principles of entanglement between the spin of an atom and polarization of a photon were shown. Based on the work presented in [17, 18] a setup was built and optimized, allowing us to experimentally generate and detect it with a high fidelity. The relatively simple and compact setup of the single beam optical dipole trap provides the ability to store a single ^{87}Rb atom and prevents loading of several atoms due to the collisional blockade mechanism. The two-step method for detection of the atomic state allows to analyze the qubit state in an arbitrary measurement basis with a high accuracy. We have measured the correlations between the photonic and atomic states which allowed us to infer the fidelity of the entangled state. The correlation measurements were also combined giving the density matrix of the atom-photon state. The achieved fidelity $F = 0.87..0.90$ is high enough, allowing to use the entanglement for further experiments. In particular, it is a promising candidate for generation of atom-atom entanglement at a distance by entanglement swapping.

[2] These angles are valid for measurement of spins, where orthogonal states enclose an angle of $180°$. If polarization of light is measured, the angles are $\alpha = 0°, \beta = -22.5°, \alpha' = 45°, \beta' = 22.5°$.

3. Remote Preparation of an Atomic Quantum Memory

3.1. Introduction

Atom-photon entanglement opens a wide range of possibilities for new experiments. In particular it represents an interface between atom-based systems and photonic communication channels. This allows to combine the advantages of atomic capabilities for storage and processing of quantum information with long distance quantum communication possible with photons. These important properties are key elements in future applications of quantum information processing.

This chapter shows the first demonstration of a quantum communication protocol between an atomic and a photonic qubit. The protocol utilizes the quantum teleportation scheme in order to remotely prepare the state of the atom. It requires a way to encode the state to be prepared onto the photon and a realization of a complete Bell-state measurement. Both requirements are fulfilled in an elegant way by using an interferometer allowing to prepare arbitrary states on the atom.

3.2. Theoretical scheme

In this section I will present the principal schemes of quantum teleportation and remote state preparation. Both protocols provide a solution to the problem of transferring the quantum state of a qubit to a remote location without sending the particle itself.

3.2.1. Quantum teleportation

Let us consider a typical situation in quantum communication: there are two separate parties (traditionally called Alice and Bob), where Alice is in possession of an unknown qubit state $|\Psi\rangle_A$ which has to be transferred to Bob. If Alice is able to send the qubit itself over some kind of quantum channel, no problem arises. However, sending of the particle directly might be either impossible or at least lead to a strong degradation of fidelity. For example moving a trapped atom to a different location represents an experimental challenge [48], even within the same apparatus. For communication on macroscopic distances a different approach is needed.

A solution by classical means would be to measure the state of the qubit and send the result to Bob who would then prepare the state on his side. Unfortunately it is not possible to acquire full information of an arbitrary quantum state with a single measurement. Together with the fact that a measurement in general changes the quantum state, it follows that it is impossible to reconstruct the state on Bob's side without losses. To infer the limit for the case of a qubit we consider a von-Neumann measurement, which is a projection onto eigenstates of a certain basis $|\downarrow\rangle$, $|\uparrow\rangle$. A general qubit state can be written in this basis as $|\Psi\rangle = e^{i\phi}\cos(\frac{\alpha}{2})\,|\uparrow\rangle + \sin(\frac{\alpha}{2})\,|\downarrow\rangle$. When this state is subject to such projective measurement, two outcomes are possible. With the probability $p_\uparrow = \cos(\frac{\alpha}{2})^2$ Alice gets the state $|\uparrow\rangle$, the fidelity for Bob is then $F_\uparrow = |\langle\uparrow|\Psi\rangle|^2 = \cos(\frac{\alpha}{2})^2$. With the probability $p_\downarrow = \sin(\frac{\alpha}{2})^2$

Alice's outcome will be $|\downarrow\rangle$, the fidelity at Bob's side in this case is $F_\downarrow = |\langle\downarrow|\Psi\rangle|^2 = \sin(\frac{\alpha}{2})^2$. The mean fidelity is determined by integrating over all states on the Bloch sphere

$$\bar{F}_{class}^{teleport} = \frac{1}{4\pi}\int_0^{2\pi} d\phi \int_0^{\pi} d\alpha \sin(\alpha)\,(p_\uparrow \cdot F_\uparrow + p_\downarrow \cdot F_\downarrow)$$
$$= \frac{1}{2}\int_0^{\pi} d\alpha \sin(\alpha)\left(\cos(\frac{\alpha}{2})^4 + \sin(\frac{\alpha}{2})^4\right) = \frac{2}{3} \quad (3.1)$$

The classical limit of fidelity for this scenario is given by the extraction of information by a quantum measurement (a general consideration of this problem is given in [49]).

The situation changes dramatically if Alice and Bob share a source of entangled pairs[1]. We will show that it is then possible to transfer the state $|\Psi\rangle_A$ with (in principle) perfect fidelity at the cost of one entangled pair shared by Alice and Bob and two bits of classical communication [47]. Consider the state of qubit A owned by Alice

$$|\psi\rangle_A = \beta\,|\uparrow\rangle_A + \gamma\,|\downarrow\rangle_A \quad (3.2)$$

where $\beta = e^{i\phi}\cos(\frac{\alpha}{2})$ and $\gamma = \sin(\frac{\alpha}{2})$. The entangled pair BC shall be in the state

$$|\Psi\rangle_{BC} = \frac{1}{\sqrt{2}}\left(|\uparrow\rangle_B\,|\downarrow\rangle_C + |\downarrow\rangle_B\,|\uparrow\rangle_C\right)$$

where the particle B is owned by Bob and particle C by Alice. The state of all three particles can then be written as

$$|\Psi\rangle_{ABC} = (\beta\,|\uparrow\rangle_A + \gamma\,|\downarrow\rangle_A) \otimes \frac{1}{\sqrt{2}}\left(|\uparrow\rangle_B\,|\downarrow\rangle_C + |\downarrow\rangle_B\,|\uparrow\rangle_C\right) \quad (3.3)$$
$$= \frac{1}{2\sqrt{2}}(\beta\,|\uparrow\rangle_B + \gamma\,|\downarrow\rangle_B) \otimes (|\uparrow\rangle_A\,|\downarrow\rangle_C + |\downarrow\rangle_A\,|\uparrow\rangle_C)$$
$$+ \frac{1}{2\sqrt{2}}(\beta\,|\uparrow\rangle_B - \gamma\,|\downarrow\rangle_B) \otimes (|\uparrow\rangle_A\,|\downarrow\rangle_C - |\downarrow\rangle_A\,|\uparrow\rangle_C)$$
$$+ \frac{1}{2\sqrt{2}}(\beta\,|\downarrow\rangle_B + \gamma\,|\uparrow\rangle_B) \otimes (|\uparrow\rangle_A\,|\uparrow\rangle_C + |\downarrow\rangle_A\,|\downarrow\rangle_C)$$
$$+ \frac{1}{2\sqrt{2}}(\beta\,|\downarrow\rangle_B - \gamma\,|\uparrow\rangle_B) \otimes (|\uparrow\rangle_A\,|\uparrow\rangle_C - |\downarrow\rangle_A\,|\downarrow\rangle_C)$$

Using the common definition of maximally entangled Bell-states

$$\left|\Psi^{\pm}\right\rangle = \frac{1}{\sqrt{2}}\left(|\uparrow\rangle\,|\downarrow\rangle \pm |\downarrow\rangle\,|\uparrow\rangle\right) \quad (3.4)$$
$$\left|\Phi^{\pm}\right\rangle = \frac{1}{\sqrt{2}}\left(|\uparrow\rangle\,|\uparrow\rangle \pm |\downarrow\rangle\,|\downarrow\rangle\right)$$

[1] The problem of distributing a set of entangled pairs with high fidelity is less complex than preserving the fidelity of the state while sending particles directly. The solution is to extract a smaller set of highly entangled pairs from a large set of pairs with lower entanglement fidelity by using entanglement purification/distillation protocol [50]. Additionally atom-photon entanglement allows to entangle distant atoms without the need to transport the atoms themselves.

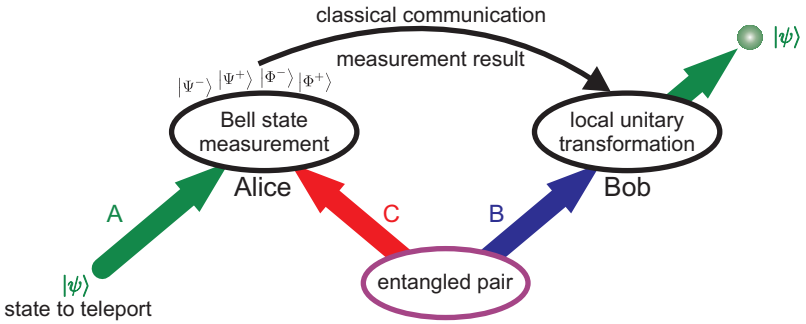

Figure 3.1.: Scheme of the teleportation protocol.

we can finally write the state of the three particles as

$$\begin{aligned}|\Psi\rangle_{ABC} = &\frac{1}{2}\left(\beta\,|\uparrow\rangle_B + \gamma\,|\downarrow\rangle_B\right) \otimes \left|\Psi^+\right\rangle_{AC} \\ &+ \frac{1}{2}\left(\beta\,|\uparrow\rangle_B - \gamma\,|\downarrow\rangle_B\right) \otimes \left|\Psi^-\right\rangle_{AC} \\ &+ \frac{1}{2}\left(\beta\,|\downarrow\rangle_B + \gamma\,|\uparrow\rangle_B\right) \otimes \left|\Phi^+\right\rangle_{AC} \\ &+ \frac{1}{2}\left(\beta\,|\downarrow\rangle_B - \gamma\,|\uparrow\rangle_B\right) \otimes \left|\Phi^-\right\rangle_{AC}\end{aligned} \tag{3.5}$$

Therefore, if Alice performs a Bell-state measurement (i.e. a projection onto the states $\left|\Psi^{\pm}\right\rangle$, $\left|\Phi^{\pm}\right\rangle$) of her particles A and C, the particle B of Bob will be projected onto one of four well-defined states according to Eq. (3.5). The first state is identical to the original one. The other three can be transformed into it using defined unitary rotations $\hat{\sigma}_x$, $\hat{\sigma}_z$ and $\hat{\sigma}_x \cdot \hat{\sigma}_z$. These rotations do not depend on the teleported state but only on the Bell-state which is observed by Alice. Alice now communicates classically the result of her measurement (4 outcomes correspond to 2 bit) to Bob who then can perform the necessary rotation thereby reconstructing the input state on his side. A schematic representation of this protocol is shown in Fig. 3.1.

The teleportation protocol was first experimentally realized using polarization-entangled photons [51, 52]. With time-bin encoded photonic qubits the protocol was demonstrated over a $2\,\mathrm{km}$ long fiber [53]. The main problem in experiments with photons is the Bell-state measurement as it requires a realization of a two-qubit CNOT-operation. With linear optics elements it is possible to deterministically detect only two of the four Bell-states[54] (using a probabilistic scheme, three Bell-states can be detected [55]). For neighboring ions in a trap, where two-qubit operations are well-established, the protocol was implemented with detection of all four Bell-states [56, 57]. A realization using continuous variables, such as quadratures of the electromagnetic field, was also reported [58]. Recently a realization involving a spin-wave in an atomic ensemble and a non-classical state of electromagnetic field was demonstrated [59].

3.2.2. Remote State Preparation

A similar problem to the transfer of an unknown quantum state between two parties is the transfer of a known state to a remote location (remote preparation). In this case Alice could in principle tell Bob which state to prepare, avoiding the problem of measuring an unknown state. However, the amount of information which has to be transferred classically is infinitely large since two real numbers (α, ϕ) are required to completely specify the state of a qubit.

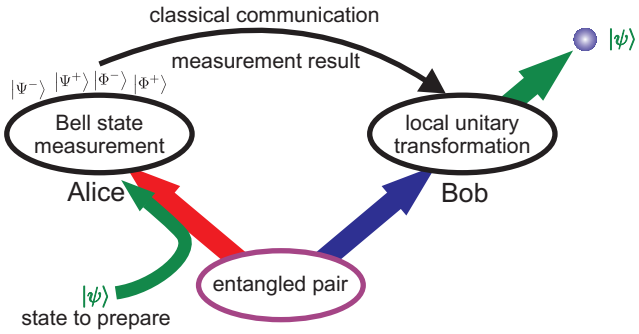

Figure 3.2.: Scheme of remote state preparation.

With the help of quantum mechanics the problem can be solved if a source of entangled pairs is shared by Alice and Bob. A straightforward method for Alice is to measure her half of the entangled pair in a basis which contains the state to be transferred. Since the measurement outcomes of Alice and Bob are correlated (e.g. for the entangled state $|\Psi^-\rangle$ Bob's particle is always projected onto the state which is orthogonal to Alice's) this measurement prepares the input state on Bob's side with probability of 0.5. In the case of complementary outcome in Alice's measurement, Bob's state is orthogonal to the required one and can not be rotated into it by a predefined operation (a universal NOT-operation does not exist) - the protocol fails. The procedure has to be repeated until Alice gets the right measurement outcome which is then reported to Bob (one bit of classical communication). A general consideration of this scenario for many qubits and different input resources is done in [60]. Implementations of this scheme with entangled photons [61], light beams [62] and nuclear magnetic spins [63] have been reported[2].

We consider the performance of a "classical remote state preparation" scheme which can be performed in absence of entanglement with two bits of classical communication. The best way to use this information is to agree on four selected states which are known to both parties. Alice then determines which of these four states is the next to the one to be prepared and sends this information (2 bits) to Bob who prepares it on his side. As the four states have to be optimally distributed on the Bloch sphere, the best choice are vertices of a tetrahedron. This classical protocol has unit fidelity only if the state which has to be sent coincides with one of the four selected states. For all other states the preparation on the other side is only an approximation. The fidelity is then given by the projection of the state onto the nearest of the selected four. The average fidelity is calculated by integrating this state-dependent fidelity, giving an analytic expression

$$\bar{F}^{RSP}_{class} = \frac{\sqrt{3}}{\sqrt{2}}\frac{1}{\pi}\arctan(\sqrt{2}) + \frac{1}{2} = 0.872 \tag{3.6}$$

However, by using the teleportation protocol it is possible to achieve both the fidelity and success probability of unity. The requirement of detection of all four Bell-states can be solved in an elegant way by using an additional degree of freedom of the entangled particle C in order to imprint the known state $|\Psi\rangle_A$ [64]. This expansion of the Hilbert space allows to simplify the Bell-state analysis in that case taking place between two degrees of freedom of the same particle. The rest of the protocol is identical to teleportation, see Fig. 3.2. The state imprinted onto the particle C is projected onto Bob's particle up to a unitary rotation depending on the detected Bell-state. First experimental realizations

[2] In principle, such preparation is performed implicitly in any correlation measurement of an entangled pair. In our experiment we use this procedure e.g. to prepare initial states for the study of the time evolution, see Sec. 4.6.1.

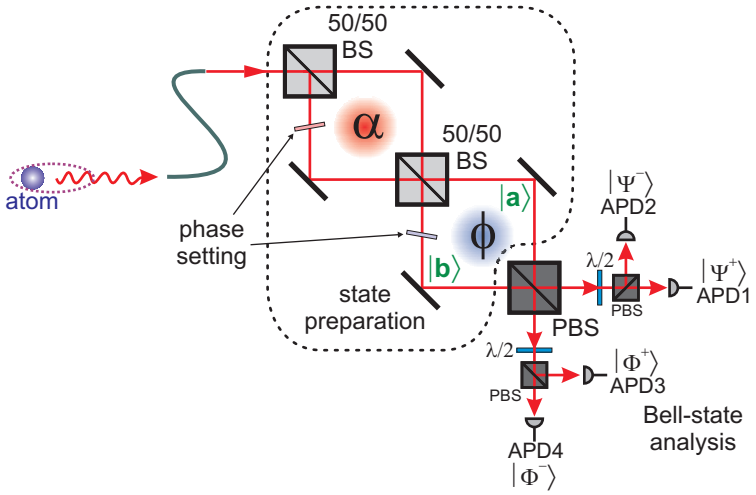

Figure 3.3.: Schematic of the interferometric setup realizing the remote state preparation protocol. The state to be prepared on the atom is encoded into the spatial modes $|a\rangle$ and $|b\rangle$ of an interferometer and is completely defined by the interferometer phases (α, ϕ). The full Bell-state analysis is realized by interference of the two modes on a polarizing beam splitter with subsequent polarization analysis in $|\pm 45°\rangle$-basis.

with polarization-entangled photons were reported in [52] (where it was called teleportation) and in [65]. As will be shown in the following this scheme can be conveniently adopted to our experiment allowing to remotely prepare the state on the atom.

3.3. Experimental Realization

The goal of this section is to use the polarization entanglement between the atom and the photon in order to prepare the atomic state over a distance. The state which has to be prepared is encoded into the spatial degree of freedom of the photon using an interferometer. The required Bell-state measurement between the polarization and the spatial degree of freedom of the photon can then be realized by relatively simple means.

Consider the scheme shown in Fig. 3.3. In the first step the photon is coherently split into two spatial modes $|a\rangle$ and $|b\rangle$ by means of a polarization-independent Mach-Zehnder interferometer, resulting in the spatial state $\cos(\frac{\alpha}{2})\,|a\rangle + \sin(\frac{\alpha}{2})\,|b\rangle$. The phase α is determined by the optical path-length difference between the two interferometer arms. The first interferometer serves as a variable beam-splitter which controls the amplitudes in the modes $|a\rangle$ and $|b\rangle$. Next, the two spatial modes acquire an additional phase difference ϕ in a second interferometer, resulting in the state

$$|\Psi\rangle_A = \mathrm{e}^{i\phi}\cos(\frac{\alpha}{2})\,|a\rangle + \sin(\frac{\alpha}{2})\,|b\rangle \tag{3.7}$$

of the photonic qubit. This state shall be prepared at Bob's side (the atom). It is completely controlled by the two phases (α, ϕ) of the double interferometer.

The next step is the Bell-state measurement in the joint polarization/spatial-mode Hilbert space of the photon. This is done by combining the two modes $|a\rangle$ and $|b\rangle$ on a polarizing beam-splitter and analyzing the photon polarization in each output port. The polarization analyzer detects $|\pm 45°\rangle =$

$\frac{1}{\sqrt{2}}(|H\rangle \pm |V\rangle)$ polarized photons (APD1..4). Since the PBS transmits horizontal $|H\rangle$ and reflects vertical $|V\rangle$ polarization, a coherent superposition of orthogonal polarizations from both modes is necessary to obtain $|\pm 45°\rangle$ in the output of the PBS. For example the $|+45°\rangle$ polarization state detected by APD1 (Fig. 3.3) is composed from $|H\rangle$ polarization which is transmitted by PBS from mode $|b\rangle$ and $|V\rangle$ polarization which is reflected from mode $|a\rangle$. This corresponds to the Bell-state

$$\left|\Psi^{+}\right\rangle = \frac{1}{\sqrt{2}}(|V\rangle\,|a\rangle + |H\rangle\,|b\rangle)$$

Accordingly, the $|-45°\rangle$ polarization (APD2) corresponds to the state $|\Psi^{-}\rangle = \frac{1}{\sqrt{2}}(|V\rangle\,|a\rangle - |H\rangle\,|b\rangle)$, while in the other output of the PBS the states $|\Phi^{\pm}\rangle = \frac{1}{\sqrt{2}}(|H\rangle\,|a\rangle \pm |V\rangle\,|b\rangle)$ are detected.

For a given phase setting (α, ϕ) of the interferometer, detection of the photon projects the atom similar to Eq. (3.5) onto one of the states

$$\begin{aligned}
|\Phi_1\rangle &= \mathrm{e}^{i\phi}\cos(\frac{\alpha}{2})\,|\uparrow\rangle_x + \sin(\frac{\alpha}{2})\,|\downarrow\rangle_x \\
|\Phi_2\rangle &= \mathrm{e}^{i\phi}\cos(\frac{\alpha}{2})\,|\uparrow\rangle_x - \sin(\frac{\alpha}{2})\,|\downarrow\rangle_x \\
|\Phi_3\rangle &= \mathrm{e}^{i\phi}\cos(\frac{\alpha}{2})\,|\downarrow\rangle_x - \sin(\frac{\alpha}{2})\,|\uparrow\rangle_x \\
|\Phi_4\rangle &= \mathrm{e}^{i\phi}\cos(\frac{\alpha}{2})\,|\downarrow\rangle_x + \sin(\frac{\alpha}{2})\,|\uparrow\rangle_x
\end{aligned} \tag{3.8}$$

depending on which Bell-state was detected ($|\Phi_1\rangle$ .. $|\Phi_4\rangle$correspond to APD1..APD4, respectively). Since qubit rotations can not be performed with our present setup, the success of the state transfer will be shown by performing a complete quantum tomography of the atomic state after the Bell-state measurement.

3.3.1. Double interferometer setup

The experimental realization of the presented scheme requires a double interferometer for single photons emitted by the atom in order to prepare the state $|\Psi\rangle_A$ from Eq. (3.7). It has to allow a reliable setting of the phases (α, ϕ), furthermore interferometric stability is required for the duration of the experiment. The interferometer was designed with regard to two main criteria. First it has to be compact since small dimensions make the interferometer less sensitive to external influences and thus simplify its stabilization. Second, it has to be polarization independent: for correct implementation of the protocol the polarization of the photon has to be preserved during encoding of the quantum state into the spatial mode degree of freedom. This guarantees that the spatial degree of freedom where the input state is encoded does not couple to the polarization of the photon.

The setup is shown in Fig. 3.4. After the photon is entangled with the atom, it is coupled into a single-mode optical fiber and guided into the interferometer where it follows the path shown by the thick red line. First the photon impinges on a $50\colon 50$ beam splitter (BS) and is coherently split into two arms. After reflection by retroprism1 and retroprism1' it interferes again on the same beam splitter. As the result of this interference the photon is coherently split into two spatial modes $|a\rangle$ and $|b\rangle$. Here the phase α (given by the path-length difference of the first interferometer) determines the quantum mechanical amplitudes of the modes $|a\rangle$ and $|b\rangle$. In the second interferometer the two spatial modes $|a\rangle$ and $|b\rangle$ of the photon acquire a relative phase ϕ. Herewith an arbitrary spatial state of the photon (Eq. (3.7)) can be prepared by setting the phases α and ϕ. For the control of the arm length one retroprism in each interferometer is mounted on a translation stage which is additionally equipped

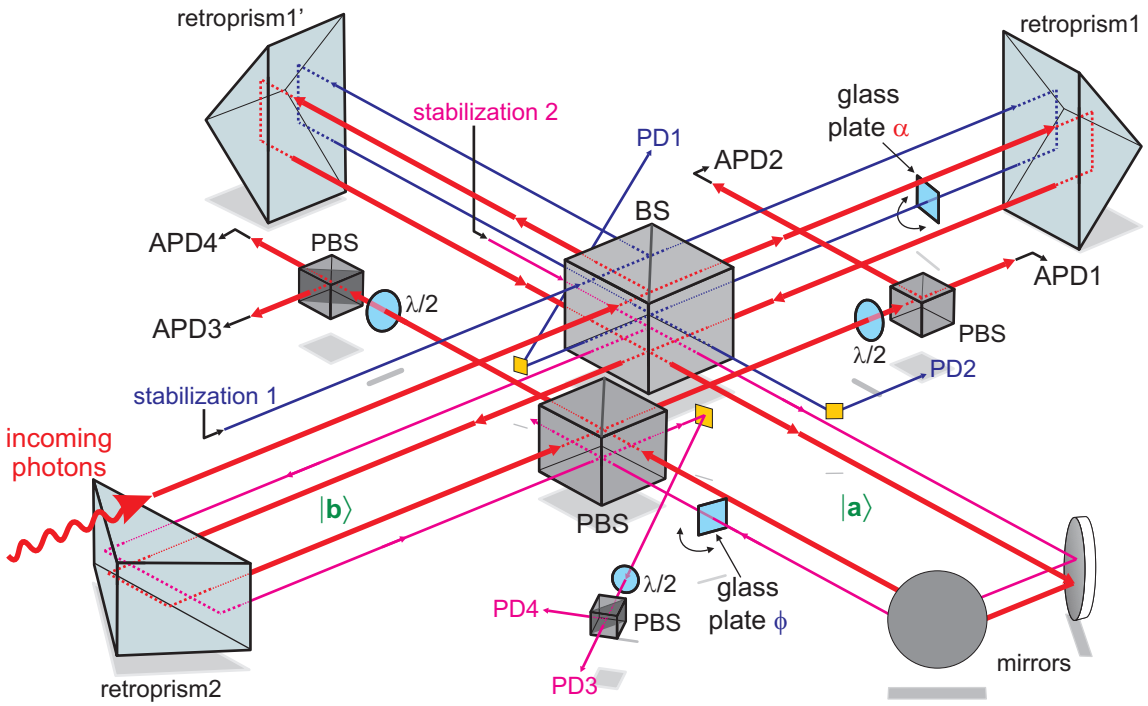

Figure 3.4.: Isometric view of the double interferometer setup. Thick red line shows the path of the single photons. The stabilization beams (thin blue and magenta lines) are at the same height as the main "beam". APD1-APD4: single photon counting avalanche photodetectors (located outside of the interferometer box), PD1-PD4: analog photodiodes for stabilization purposes. The dimensions of the arms are $15.5\,\mathrm{cm}$ in the first interferometer and $25.5\,\mathrm{cm}$ in the second.

with a piezo-element allowing coarse as well as fine positioning. For the Bell-state analysis the modes are recombined on a polarizing beam splitter (PBS). The two outputs of the PBS are analyzed in $|\pm 45°\rangle$ basis by means of a $\frac{\lambda}{2}$-plate rotated by $22.5°$ and a PBS each. Finally the four outputs of the polarization analysis are coupled into multi-mode optical fibers and guided to four single photon counting avalanche photodetectors (APD1..APD4). The detection of the photon in one of the detectors signals the projection onto the corresponding Bell-state.

As it is not possible to perform adjustments using the signal from single photons only, we have additionally coupled reference light into the interferometer. This light comes out of the same fiber and is thus perfectly mode-matched with the single photons. It allows to perform adjustments, to characterize the performance and to calibrate the phases of the interferometer before the experiment is started. The power of the reference light is few μW, sufficient for detection with analog photodiodes.

A note has to be taken on the symmetry of the arms in each interferometer. Since the coherence length of the photons emitted by the atom is about $7.8\,\mathrm{m}$, it is not necessary to ensure that both arms have exactly equal length. However, an imbalance of arm lengths Δs leads to a dependence of the interferometer phase on the frequency of the light: $\alpha, \phi \propto \frac{\Delta s}{c}\omega$. This is especially important if the phase is calibrated with light of different frequency than the frequency of the single photons in the experiment (see Sec. 3.3.3, Eq. (3.11)). In order to minimize the residual arm-length difference we have applied the following procedure for each interferometer: The frequency of the reference laser

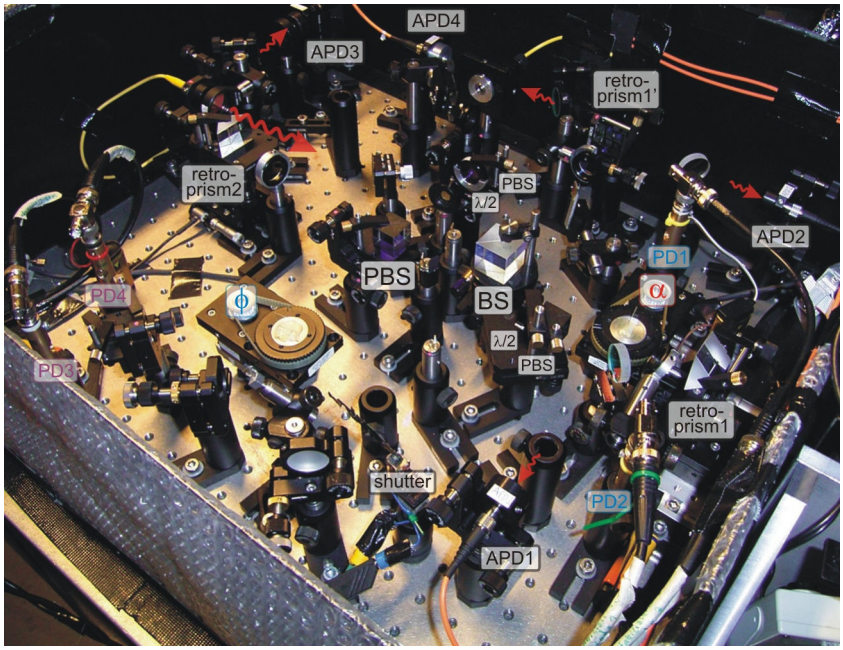

Figure 3.5.: Picture of the interferometer setup.

was periodically varied by few GHz and the modulation of the intensity in the outputs were observed giving a measure for the variation of the interferometer phase. This modulation was minimized by moving the retroprism with the translation stage. Although the used criterion is not very precise, we estimate the residual difference of the arm lengths of $\leq 1\,\mathrm{mm}$. This leads to a negligible error in the calibration of the interferometer phases as will be discussed in Sec. 3.3.3.

The most important characteristic of any interferometer is the degree of interference. For the remote preparation protocol it determines the purity of the prepared state. For example, in the first interferometer the pure states $|a\rangle$ or $|b\rangle$ can be achieved only in presence of perfect interference where the photon is directed completely into one of the modes. A figure of merit for the quality of interference is the contrast ratio, defined as $C := \frac{I_{max}-I_{min}}{I_{max}+I_{min}}$, where I is the intensity in an output port as function of the interferometer phase. Ideally it should be possible to achieve complete extinction ($I_{min} = 0$) in any of the outputs. However, this requires exactly equal reflection and transmission coefficients of the beam splitter BS ($T \stackrel{!}{=} R$), together with perfect spatial mode overlap of the beams coming from the two input ports. The (specially selected) BS used in this experiment has an intensity splitting ratio ($T\colon R$) of $49\colon 51$ allowing a maximal contrast of 0.9996[3]. The contrast can be measured by periodically varying the position of the retroprism, resulting in a change of the interferometer phase and therefore in modulation of intensity in the outputs. The prisms were mounted on tilt-stages allowing to adjust the spatial overlap. The achieved contrast in the first interferometer was typically $C_1 \geq 0.99$ with a maximally observed value of 0.998.

For the adjustment of the spatial mode overlap in the second interferometer, one arm of the first

[3]The two outputs of a Mach-Zender interferometer have different contrast ratios. In one output the beam which is reflected two times interferes with the beam which is transmitted two times, the minimal intensity is given by $|R-T|^2$. In the other output each beam is reflected and transmitted once, the minimal intensity is $\left|\sqrt{RT}-\sqrt{TR}\right|^2 = 0$. Therefore, the contrast ratio in one output depends on parameters of the beam splitter while the other output can always achieve perfect extinction.

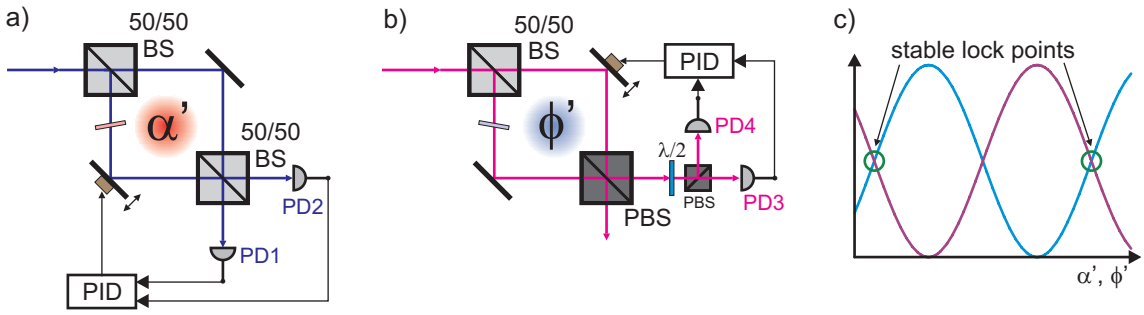

Figure 3.6.: Principle of interferometer stabilization. An additional stabilization beam passes the interferometer, the dependence of output intensities on the interferometer phase is used for generation of the feedback signal. This signal is fed via a PID-controller to a piezo translation stage moving one of the prisms. In the first interferometer (a) the outputs show directly sinusoidal dependence on phase α'. In the second interferometer (b) the polarization state of the outputs depends on phase ϕ', giving sinusoidal dependence in $\pm 45^\circ$ basis. c) Illustration of the signal on the photodiode pairs as a function of the phases α', ϕ'. The feedback system locks to points where the two intensities are equal and have the right sign of the slope.

interferometer was blocked. This gives a constant and approximately equal intensity of reference light in the two arms of the second interferometer. In order to observe complete interference on the PBS the beam has to be $\pm 45^\circ$ polarized. By periodically changing the position of the retroprism one can again observe intensity modulation in the outputs, the spatial overlap can be adjusted conveniently by two mirrors. Typically the contrast measured this way was $C_2 = 0.985$.

Finally we have analyzed the combined contrast of both interferometers together. The retroprism of the second interferometer was periodically displaced while the first interferometer remained unchanged. Maximal contrast can be observed if the phase of the first interferometer is $\alpha = \frac{\pi}{2}$ which can be set by manually translating its prism. We have observed a combined contrast of $C \sim 0.96$.

3.3.2. Interferometer stabilization

In order to perform the remote preparation experiment with single photons at relatively low rate (10..20 events per minute) it is necessary to ensure the stability of the interferometer for long periods of time. This requires proper screening of influences from the environment. To reduce the influence of air flow and temperature changes which come from the air conditioning system the setup is enclosed in a box, however, the phase stability achieved this way is not sufficient. Therefore, an active stabilization system is required.

The principle of active stabilization of the first interferometer is shown in Fig. 3.6(a). To measure a change of the interferometer phase one uses the phase dependence of the output intensities. A laser beam (wavelength $\lambda = 795\,\mathrm{nm}$, power of several μW) is coupled into the interferometer parallel to the path of single photons and at the same height (Fig. 3.4, thin blue line). After the interference on the BS the two outputs are coupled out by small gold mirrors and their intensities are measured with analog photodiodes (Fig. 3.4 PD1 and PD2). The two measured voltages depend on the interferometer phase α' as $\cos(\frac{\alpha'}{2})^2$ and $\sin(\frac{\alpha'}{2})^2$. The voltages are put to a feedback (integrating PID) controller. The output of the controller is amplified and fed to the piezo element of the translation stage which

moves one of the retroprisms according to this feedback signal. A stable point of such feedback loop is where the intensities of the two stabilization output ports are equal, small deviations lead to a change of the control voltage which moves the prism to counteract the perturbation. Each period of $\cos(\frac{\alpha'}{2})^2$ vs $\sin(\frac{\alpha'}{2})^2$ oscillation has one such point, therefore there are infinitely many stable points. Since the wavelength used for the stabilization is different from that of single photons (this is needed to eliminate background of the stabilizing light on single photon detectors with interference filters), the phase $\alpha \neq \alpha'$ remains unknown. This requires a calibration procedure to measure and set the interferometer phase which will be discussed in section 3.3.3.

The stabilization method for the second interferometer works similarly (schematic in Fig. 3.6(b), real beam path in Fig. 3.4, thin magenta line), however, here the phase dependence of the output polarization is used. For $+45°$ input polarization the state of the outputs depends on the phase ϕ' as $\frac{1}{\sqrt{2}}(H \pm e^{i\phi'}V)$. Therefore, if the polarization in the output is analyzed in $\pm 45°$ basis (Fig. 3.4 PD3 and PD4), the results are again sinusoidal functions of opposite phase. These signals are used for stabilization of the second interferometer.

Performance of the stabilization system

There are two main characteristics of the stabilization system which define its performance and shall be considered here. The first point is the stability with respect to fast fluctuations such as acoustics, vibrations and air turbulence. The bandwidth of the feedback system is limited by the speed of the piezo-driven translation stage. As the retroprism together with its mount and the platform of the translation stage have a large mass, the overall bandwidth is about $5\,\mathrm{Hz}$. The box which encloses the whole interferometer arrangement strongly damps the external vibrations and airflow. During the fully automatic measurement no persons need to be present in the lab, and the influence of acoustic vibrations was shown to be negligible. For the remaining slow drifts the bandwidth of the feedback system is sufficient.

The second point is the robustness with respect to the drifts of the ambient temperature. In our lab the air temperature is controlled by a common split air conditioner cooling the air in periods of $20..60\,\mathrm{min}$. The stability of air temperature depends on outside weather conditions and is typically $1..2°\mathrm{C}$. In order to characterize the phase drifts, reference laser was coupled into the stabilized first interferometer and the intensities in the output ports were observed. It was found that the stability of the interferometer phase strongly depends on the position of the stabilization beam with respect to the path of single photons. In the first design of the interferometer, the stabilization beam was located $10\,\mathrm{mm}$ below the main path. As the phase of the stabilizing beam is kept constant by the feedback system, thermal expansion/contraction of the table and of mechanical elements, as well as global changes of the air density, are exactly compensated. However, thermally induced bowing of the optical table affects beams on different heights differently, see Fig. 3.7(a), (b). For the height difference d and bowing angle ϵ the path length difference between the two beams is $\Delta s = d \cdot \tan(\epsilon)$. Taking $\Delta s := \frac{\lambda}{2} = 390\,\mathrm{nm}$ and $d = 10\,\mathrm{mm}$ we get $\epsilon = 3.9 \cdot 10^{-5}\,\mathrm{rad}$. The drift of the phase for the considered configuration is shown in Fig. 3.7(c). The operation cycles of the air conditioner are directly visible in this graph together with a general phase drift. In order to avoid this effect the stabilization beam was put at the same height as the path of the single photons. This leads to a strong suppression of the phase drifts, Fig. 3.7(d), but a slow residual drift remained depending on ambient conditions. This residual error is eliminated by periodically performing re-calibration of interferometer phases as described in the next section.

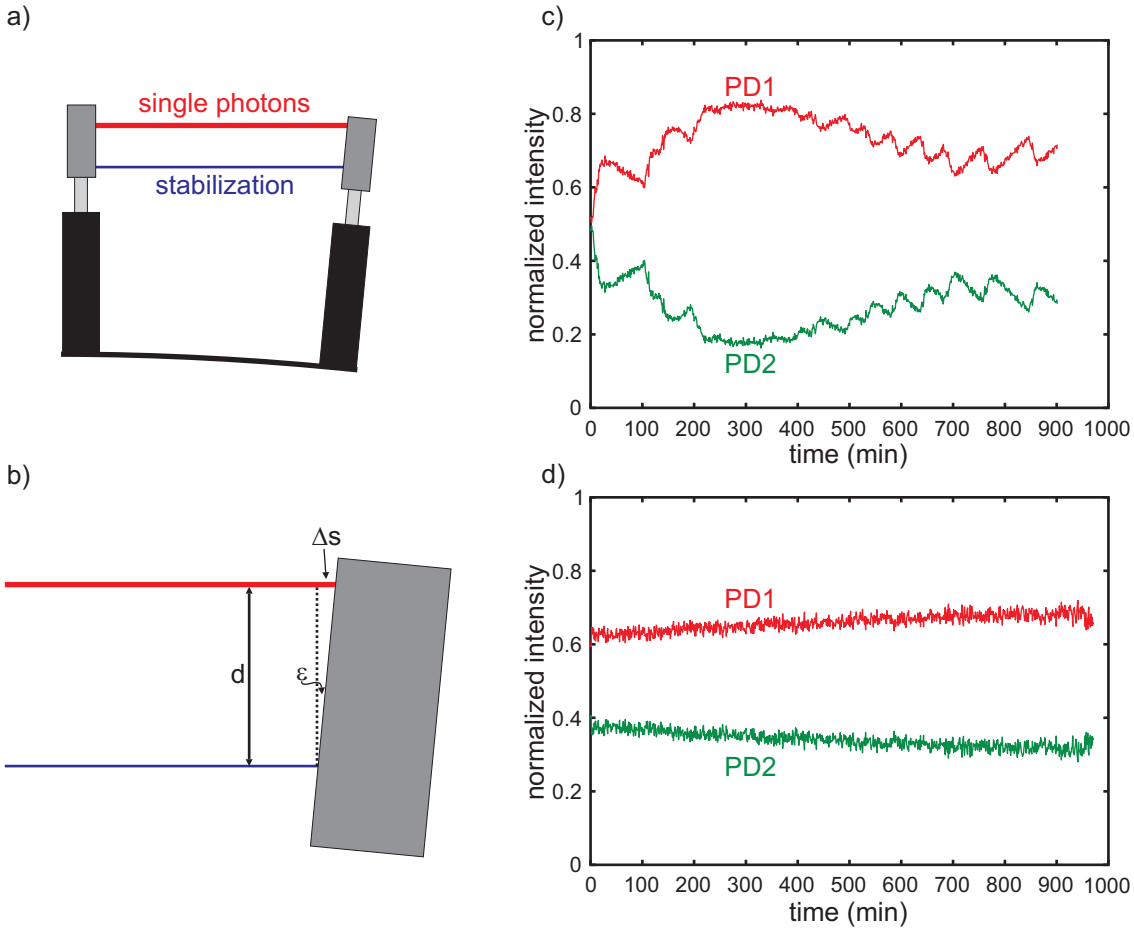

Figure 3.7.: Drifts of the interferometer phase induced by changes in the ambient temperature. a), b) Thermal bowing of the optical table leads to a length difference between the path of single photons and of the stabilization beam if these are located at different heights. c), d) Measurement of the phase drift. For the reference laser which exactly follows the path of single photons in the stabilized first interferometer, the intensities in the two output ports are measured. Graph c) shows the behavior of normalized intensities where the stabilization beam is below the main path by $d = 10\,\mathrm{mm}$, in d) the stabilizing beam is at the same height.

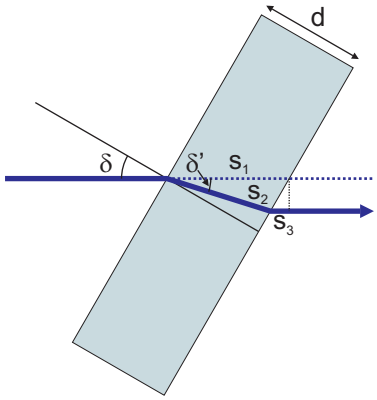

Figure 3.8.: Effect of a glass plate on the optical path of a beam.

3.3.3. Control of the interferometer phase

The stabilization system is capable of keeping the interferometer phases $(\alpha,\ \phi)$ constant, but it does not directly provide a possibility to measure these phases or to control them.

In order to control the phases, two thin glass plates were put into the stabilization beams of the interferometers (see Fig. 3.4). By rotating these plates the optical path length for the stabilization beam in one arm can be changed, the stabilization system responds by moving the retroprism. This movement restores the interferometer phase for the stabilization beam but changes the phase for single photons. The effect of the glass plate on the optical path length can be calculated as follows. Fig. 3.8 shows the geometry of the problem: the beam impinges at an angle δ upon the glass plate of thickness d and refractive index n. The path of the beam is modified by refraction: instead of following the path s_1 in air the beam follows the path s_2 in glass at an angle δ', together with a small additional segment s_3 in air. Therefore, the total effect of the glass plate is

$$\begin{aligned}\Delta s &= n \cdot s_2 + s_3 - s_1 \\ &= n \cdot \frac{d}{\cos(\delta)} + d\sin(\delta)\left(\tan(\delta) - \tan(\delta')\right) - \frac{d}{\cos(\delta')}\end{aligned} \tag{3.9}$$

The refraction angle δ' follows Snell's law $n \cdot \sin(\delta') = \sin(\delta)$. Since $\delta = 0°$ is a local extremum for the optical path length, we have chosen $\delta = 10°$ as the initial position. The glass plates in our experiment have $d = 0.135\,\mathrm{mm}$ and $n = 1.513$. We get $\Delta s(10°) = 69.9\,\mu\mathrm{m}$ and $\Delta s(15°) = 70.8\,\mu\mathrm{m}$, thus rotating the plate by $5°$ changes the optical path length by $900\,\mathrm{nm}$ which is sufficient to vary the phase by more than 2π.

The calibration procedure of the interferometer phases $(\alpha,\ \phi)$ is the following. It is performed with reference light of $+45°$ polarization which is attenuated to a level that can be counted with single photon APDs (count rate of several ten thousand per second). To get the phase α of the first interferometer, one arm of the second interferometer is blocked with a mechanical shutter (without affecting the stabilization beam). The intensity in the outputs of the whole interferometer is then proportional to the output of the first interferometer. The angle of the glass plate δ_1 of the first interferometer is rotated by $5°$ in steps of $\frac{1}{5}°$ and the count rate of one APD is recorded. The dependence of the phase α on δ_1 is determined by fitting[4] the function

$$A_1 \cos(\Delta\alpha(\delta_1) + \alpha_0) + B_1 \tag{3.10}$$

[4]The fit routines are provided by the GNU Scientific Library GSL http://www.gnu.org/software/gsl/ .

to the interference fringe, where A_1, B_1 are the amplitude and offset, $\Delta\alpha(\delta_1) = 2\pi\frac{\Delta s(\delta_1)}{\lambda}$ includes the non-linear response of the glass plate rotation given by Eq. (3.9) .

For the calibration of the second interferometer the phase of the first interferometer is set to $\alpha = \frac{\pi}{2}$ such that its outputs have equal amplitudes, assuring maximal interference contrast. The shutter block is removed and the angle δ_2 is varied by 5° in steps of $\frac{1}{5}^\circ$ while measuring the count rate on one APD. Again the function $A_2\cos(\Delta\phi(\delta_2) + \phi_0) + B_2$ is fitted to the obtained interference fringe providing the dependence $\phi(\delta_2)$. The whole procedure is fully automatic and takes about one minute, this time is mainly given by acquisition of APD counts (1 s per point) and rotation of the motors. It is repeated after every experimental run ($12\,\mathrm{min}$) and counteracts the phase drift resulting from changes in the ambient temperature (see Fig. 3.7(d)).

Performance of the phase calibration

In order to estimate the limits of the phase calibration method we consider the main points contributing to the error in the phase setting. The first is the error of typically $1^\circ..2^\circ$ in the fit which extracts the phase from the motor position. The second error comes from the fact that the reference light used for calibration of the phase has not exactly the same frequency as the single photons in the experiment. For a given path-length difference between the two interferometer arms Δs the interferometer phase is given by

$$\alpha = 2\pi\frac{\Delta s}{\lambda_l} = \frac{\omega_l}{c}\Delta s \tag{3.11}$$

where λ_l and ω_l are the wavelength and angular frequency of the light respectively. From this relation the difference in the phase for differing light frequencies can be easily calculated. For the frequency difference in our experiment ($\Delta\omega = 2\pi \cdot 51\,\mathrm{MHz}$ due to technical reasons) and an estimated global path-length difference of $\Delta s \leq 1\,\mathrm{mm}$ the error of the phase is $\leq 0.06^\circ$ and can be neglected.

By periodically performing the phase calibration procedure the long-term stability is only limited by mechanical drift of the components which leads to a misalignment of the beams and a reduction of the contrast. During the fully automatized measurements we were able to continuously operate the experiment for time periods as long as 24 hours.

3.3.4. Effects of birefringence in the setup

The preservation of photon polarization, which is necessary for the implementation of the remote preparation protocol, turned out to be one of the biggest difficulties in the experimental realization. In general the polarization changes on reflection at any component (beam splitter, retroprism, mirror). As long as all reflections take place in the horizontal or vertical plane, H and V polarizations (corresponding to $s-$ and $p-$) are not changed, however, a phase is introduced between H and V. This phase results from different penetration depths on reflection at boundaries between different media. Additionally the glue, which is used to stick together the prisms in beam splitters, can be birefringent due to mechanical stress. The polarization errors induced this way disturb the preparation procedure and have to be avoided or compensated.

The first step was to define a common vertical/horizontal basis for all components. This was done with a polarizing filter (extinction ratio better than $1:5000$), whose scale was independently calibrated with respect to the optical table. The critical elements like the BS and the polarization analyzers were aligned such that their eigen-axes coincided with the so-defined vertical/horizontal directions.

For compensation of the phases between H and V a birefringent plate was installed in each arm of the two interferometers. The eigen-axes of the plates were aligned such that H and V polarizations

remained unchanged, however, the refractive index is different for these two polarizations thereby inducing a phase. By tilting the plate this phase can be changed in a controlled way. However, the procedure of compensation is quite complex since it is not possible to distinguish the phases from different sources. For example each arm of the first interferometer is split into two arms of the second interferometer, therefore changing the birefringent phase there influences two outputs at the same time. On top of this, the errors of polarizing beam splitters in the interferometer and polarization analyzers ($\sim 0.5\%..1\%$) effectively introduce additional polarization rotations. Thus, the procedure of compensating each polarization error individually has shown to be inefficient, a better method is to characterize and compensate the errors of the setup as a whole.

The best way we found for characterizing the compensation of the complete setup was to observe the signals of all four outputs of the polarization analyzers simultaneously. Reference light of defined polarizations ($H, V, \pm 45^\circ$) was sent into the interferometer and the intensities of the four outputs were measured with analog photodiodes. By varying the phase in one of the interferometers, sinusoidal intensity oscillations are observed in the outputs depending on the polarization of the input light and the phase of the remaining interferometer. The phase and amplitude dependence of the different outputs for the ideal case can be calculated and represents the ultimate criterion for adjusting the compensation plates. The compensation procedure was iterated for all four input polarizations and for scanning of both interferometer phases in order to minimize the phase errors in the outputs. It was possible to find a compromise for the phase errors which ranged between $0^\circ..8^\circ$.

Finally the birefringence of the vacuum glass cell (see also Sec. 2.4.6 and 2.7.2) had to be compensated. Since both walls of the glass cell are birefringent, however, the emitted photon passes only one, it can not be measured directly. This birefringence induces a phase in the atom-photon correlations (Fig. 2.14) and also changes the prepared state. In order to eliminate this effect an additional birefringent plate was inserted at the input of the interferometer. The required tilt angle was found experimentally by performing the complete preparation experiment for different interferometer phases. The birefringence leads to a measurable phase shift in the prepared states which was then minimized down to $\sim 1^\circ..2^\circ$.

3.4. Analysis of the experimental results

In this section the experimental results will be shown and an analysis of the performance will be presented.

3.4.1. Tomography of prepared states

In order to characterize the performance of the remote state preparation experiment, different states were prepared and analyzed. Ideally, for a given phase setting (α, ϕ) of the interferometer, the atom is projected onto one of the well-defined states from Eq. (3.8), depending on which Bell-state was detected. For the analysis of the atomic state we have performed quantum state tomography (App. B) by measuring populations of eigenstates in three conjugate bases $\hat{\sigma}_x$, $\hat{\sigma}_y$, $\hat{\sigma}_z$. This allows to reconstruct the density matrix of the prepared state.

In a first measurement run we set $\alpha = 90^\circ$ while rotating ϕ from 0° to 330° in steps of 30°. Conditioned on the detection of the photon in one of the four detectors APD1..APD4, corresponding to projection on one of the four Bell-states, the populations p of eigenstates $|\uparrow\rangle_z$, $|\downarrow\rangle_x$, and $|\uparrow\rangle_y$ were

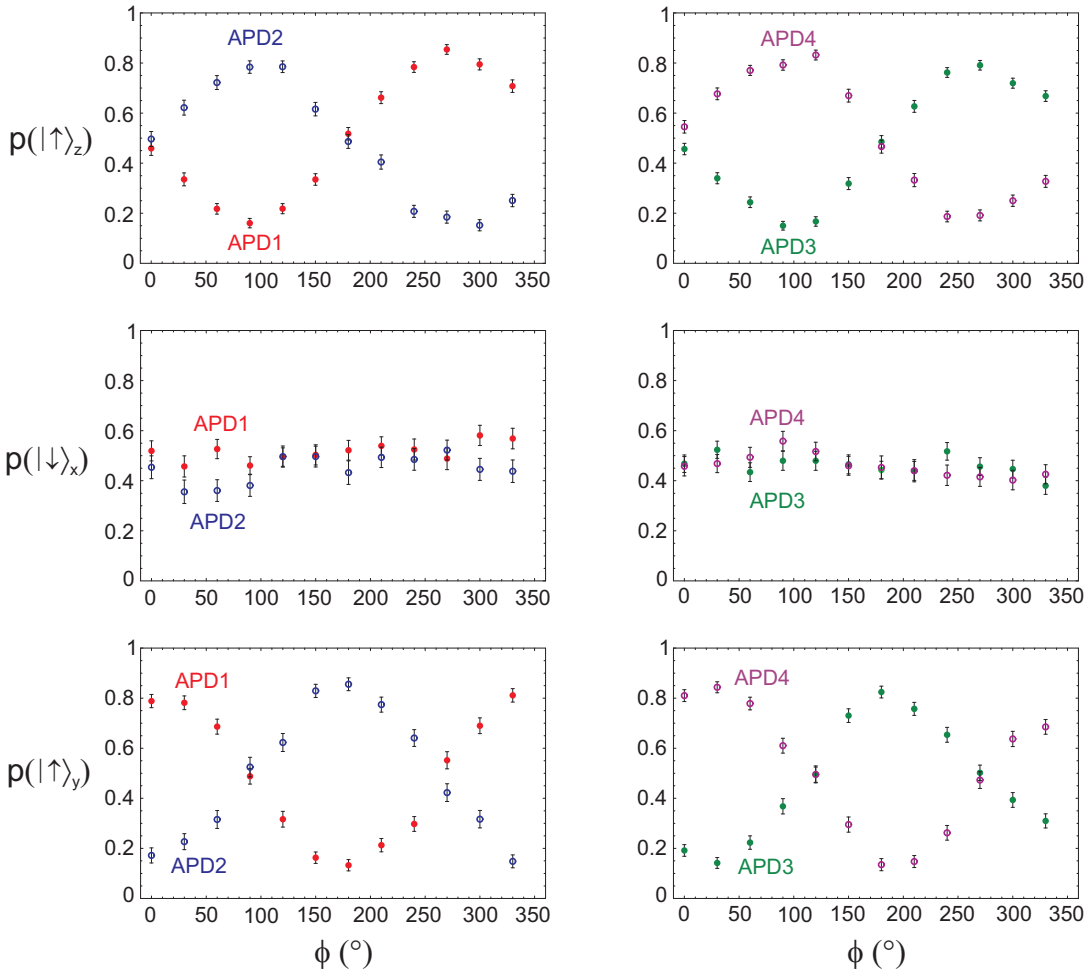

Figure 3.9.: Tomographic dataset for different prepared atomic states ($\alpha = 90°$, $\phi = 0..330°$). The graphs show the projections of the prepared states onto eigenstates of three conjugate bases ($|\uparrow\rangle_z$, $|\downarrow\rangle_x$, and $|\uparrow\rangle_y$) depending on the phase setting and the detected Bell-state. The acquisition of the full dataset was realized within approximately three days at an event rate of $10..20$ per minute.

measured (see Fig. 3.9). For the photon event in detector APD1 the state prepared is given by

$$\begin{aligned} |\Phi_1\rangle &= \cos(\frac{1}{2}(\phi+\frac{\pi}{2}))\,|\uparrow\rangle_z + i\cdot\sin(\frac{1}{2}(\phi+\frac{\pi}{2}))\,|\downarrow\rangle_z \\ &= \frac{1}{\sqrt{2}}(\mathrm{e}^{i\phi}\,|\uparrow\rangle_x + |\downarrow\rangle_x) \\ &= \cos(\frac{1}{2}\phi)\,|\uparrow\rangle_y + i\cdot\sin(\frac{1}{2}\phi)\,|\downarrow\rangle_y \end{aligned} \tag{3.12}$$

For the population of eigenstates in $\hat{\sigma}_z$ and $\hat{\sigma}_y$ bases we therefore expect a sinusoidal dependence on the phase ϕ while the population of eigenstates in $\hat{\sigma}_x$ should be constant and equal 0.5. The corresponding measurement in Fig. 3.9 clearly approves the expected behavior. The prepared states are visualized on the Bloch sphere (Fig. 3.11, blue points) and lie on a circle in the y-z plane.

By measuring the atomic qubit in $\hat{\sigma}_x$, $\hat{\sigma}_y$, $\hat{\sigma}_z$ bases we have reconstructed the density matrices for each phase setting. The preparation fidelity is calculated as the projection of the measured state onto the ideal expected state from Eq. (3.8). This procedure was performed for all 12 phase settings and all four detected Bell states, yielding an average preparation fidelity $F = 82.6\% \pm 0.40\%$.

For complete characterization of the remote state preparation we performed four sets of measurements preparing different atomic states. The density matrices for one of these measurements are exemplarily shown in Fig. 3.10. In this picture one can clearly observe the evolution of the off-diagonal elements during the rotation on the Bloch sphere. Starting with the state $|\uparrow\rangle_x$ where the off-diagonal elements are positive, they change the sign at $|\uparrow\rangle_z$ and become negative for the state $|\downarrow\rangle_x$. The reversed evolution happens between $|\downarrow\rangle_x$ and $|\downarrow\rangle_z$ finishing at $|\uparrow\rangle_x$.

For each phase setting (α, ϕ) the preparation fidelity was averaged over the four detected Bell-states $|\Psi^{\pm}\rangle, |\Phi^{\pm}\rangle$. These fidelities are shown in Fig. 3.11 together with a Bloch-sphere representation of the prepared states. The average fidelity for each of the measurement sets is summarized in Tab. 3.1. A remarkable property of the achieved preparation fidelity is its uniformity, i.e. the realization works almost equally well for any phase setting (α, ϕ). The average fidelity for all four measurements is 82.2%.

#	α	ϕ	F
1	$90°$	$0..330°$	$82.6\% \pm 0.40\%$
2	$0..330°$	$0°$	$79.7\% \pm 0.65\%$
3	$0..330°$	$90°$	$84.2\% \pm 0.45\%$
4	$109.5°$	$0..330°$	$82.2\% \pm 0.46\%$

Table 3.1.: Summary of the experimental results. The table shows the fidelity F, i.e. the probability of a successful state transfer, averaged over the 4 detected Bell-states and all 12 points within one measurement set.

The additional difficulties in performing this experiment compared to measurements in Sec. 2.7.2 were the reduced photon event rate due to losses in the interferometer and dark counts of 4 single photon detectors. The overall transmission of the interferometer including reflection losses on optical components and coupling into the multi-mode optical fibers is 60%. Together with the increased dark count rate this lead to a total fraction of 10.6% wrong events. The event rate of the experiment of $10..20$ events per minute is given by the loading time of the atomic trap. The acquisition of sufficient statistics ($150..350$ events per point) of a typical data set containing 48 measurements (analysis of 4

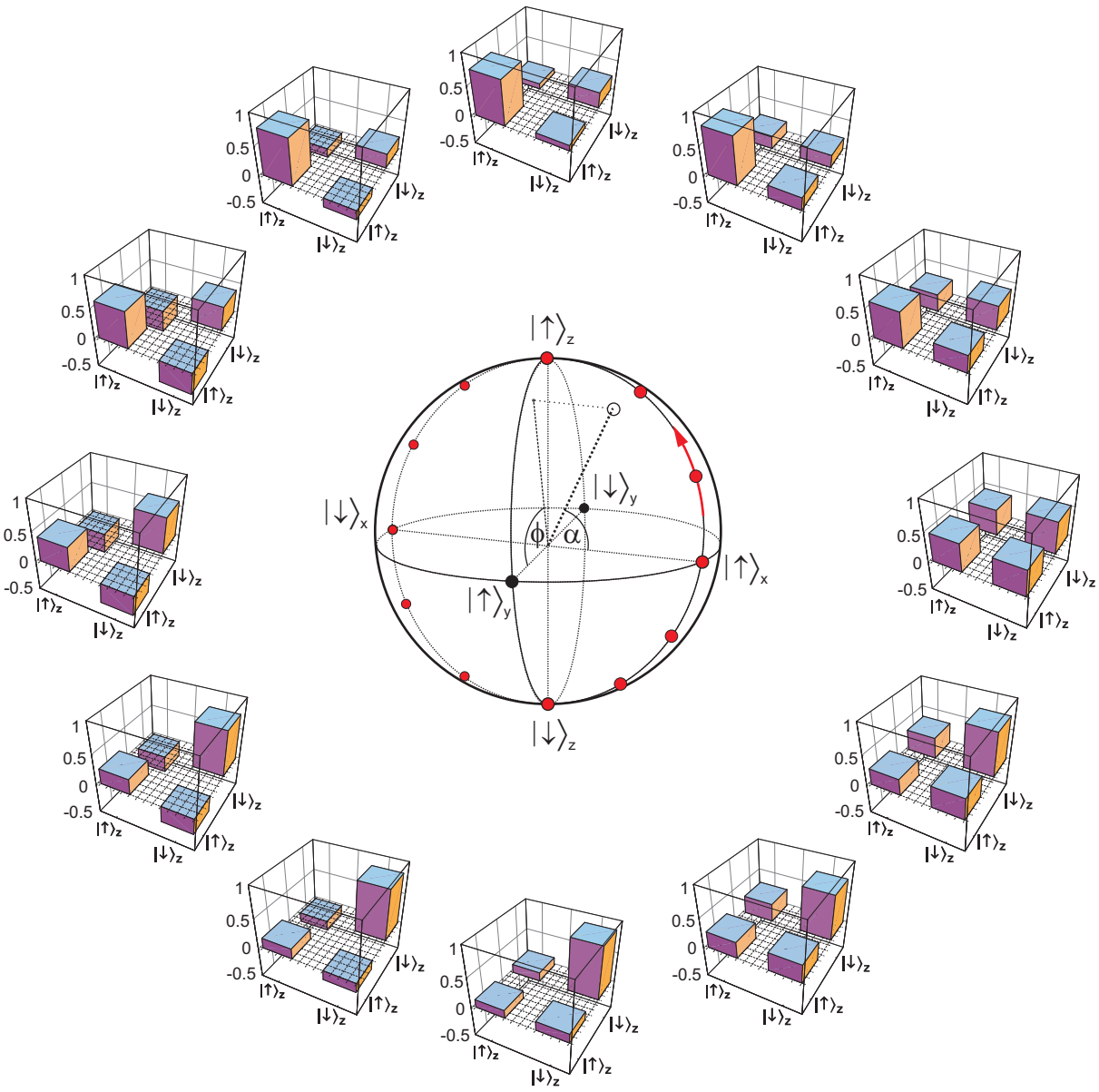

Figure 3.10.: Density matrices (real part) of the states prepared for phase settings $\alpha = 0..330°$, $\phi = 90°$ and detected Bell-state $|\Psi^+\rangle$ (APD1). The behavior of the off-diagonal elements changing the sign between $|\uparrow\rangle_x$ and $|\downarrow\rangle_x$ can be clearly observed. In the middle a Bloch-sphere representation of the target (pure) states is shown.

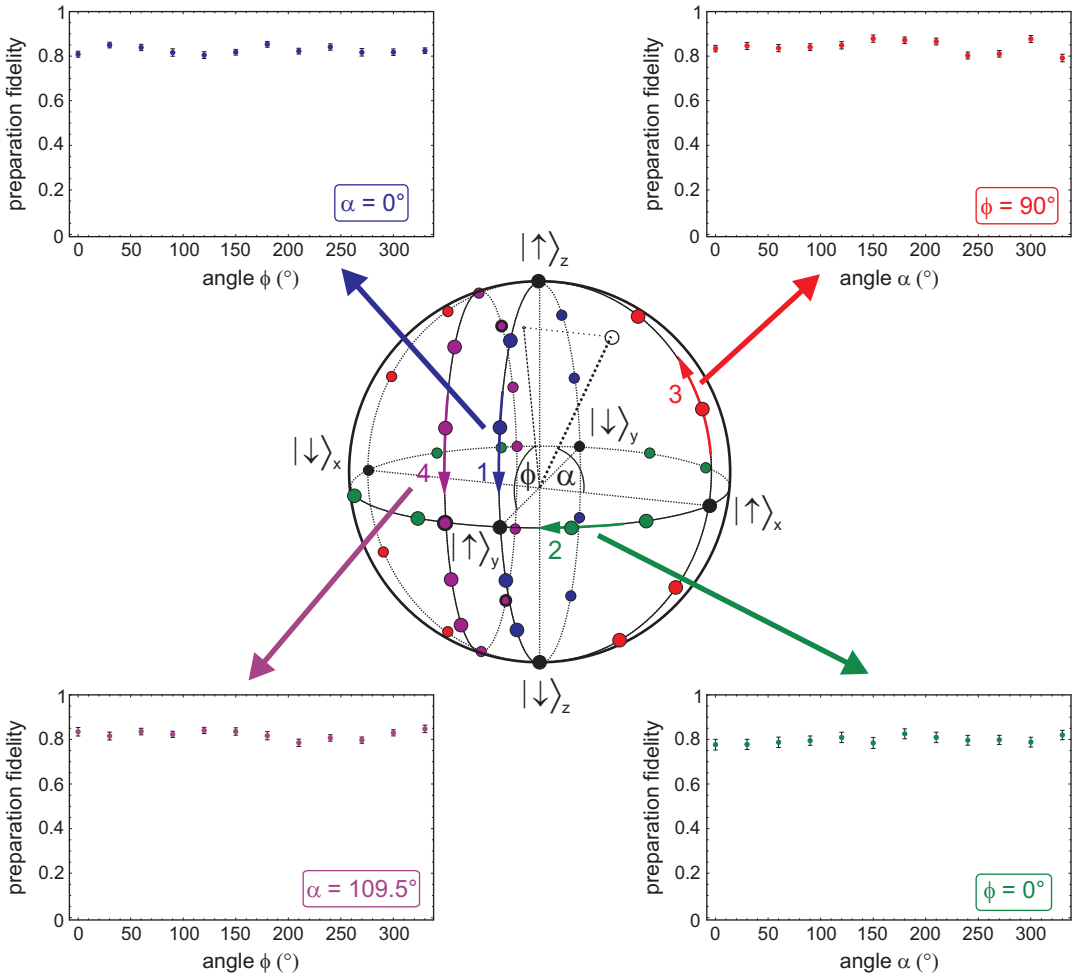

Figure 3.11.: Bloch-sphere representation of the remotely prepared atomic states. The graphs show the preparation fidelity for each phase setting (α, ϕ) averaged over the four detected Bell-states.

prepared atomic states corresponding to the 4 detected Bell-states for each of the 12 phase settings (α, ϕ)) took $12..24$ hours for each atomic measurement basis.

After correcting for errors in the preparation of the entangled state (0.5%), atomic state detection accuracy (93%) and dark counts of the detectors (10.6%) we get a corrected fidelity for the remote state preparation of 93.8%. The remaining errors are due to the limited contrast of the interferometer (96%) , phase calibration error and drift ($1\%..2\%$) and residual birefringence of the setup ($1\%..1.5\%$). The corrected fidelity is clearly above the classical limit of 87.2% given by Eq. (3.6). To compare the implemented protocol with the classical scheme, we additionally consider three states prepared in the measurement set #4 (marked by black circles) together with the prepared sate $|\uparrow\rangle_x$. The (corrected) fidelity for these four points, which correspond to vertices of a tetrahedron, of 94.6% is clearly higher than the classical limit.

3.5. Summary

This chapter presents the first experimental realization of the remote state preparation protocol between a single photon and a single atom. It allows to transfer a quantum state previously encoded on the photon onto the atomic spin. The chosen interferometric solution encodes the information in the spatial degree of freedom of the photon and allows a complete Bell-state analysis. A method for active stabilization and automatic calibration of interferometer phases was implemented allowing continuous operation of the setup for periods as long as 24 hours. The prepared atomic states were analyzed using quantum state tomography revealing an average preparation fidelity of 82.2%.

4. Coherence Properties of the Atomic Qubit

4.1. Introduction

The ability to store quantum states is an important requirement for performing any quantum information processing schemes. Here the main figure of merit is the time for which a certain quantum state remains stable. This time has to be longer than the time needed for completion of the experiment (e.g. of the quantum algorithm). For our experiment it also defines the maximal distance which the photon can be effectively communicated for further processing. For example for the planned entanglement swapping over 300 meters the atomic state has to be preserved for at least $1.5\,\mu$s without loss of fidelity of more than 1%. Therefore, the stability of the atomic quantum state is a crucial prerequisite for long-distance applications of atom-photon entanglement.

The longest history in studying coherence times in quantum systems has the field of nuclear magnetic resonance (NMR), which was developed since the 1930-ies [66]. This system was also the first one where principles of quantum computation were experimentally studied [67]. NMR is based on the interaction of an ensemble of polarized nuclear spins with magnetic fields. Each spin has two (eigen-)states $|\downarrow\rangle$, $|\uparrow\rangle$ corresponding to its orientation along the field. For the storage of quantum information, several timescales are important. The states $|\downarrow\rangle$, $|\uparrow\rangle$ show the longest relaxation time because these are eigenstates of the interaction Hamiltonian with a relatively large energy separation (typically several $100\,\mathrm{MHz}$). In this case a relatively large amount of energy has to be exchanged with the environment (e.g. with the neighboring spins in a liquid) in order to change the spin orientation. The corresponding $\frac{1}{e}$ decay time of the magnetic polarization is called the l*ongitudinal relaxation time* T_1. On the other hand, superposition states like $\frac{1}{\sqrt{2}}\left(|\downarrow\rangle + e^{i\phi}|\uparrow\rangle\right)$ are most fragile as the phase evolution of the superposition depends on the energy difference of the eigenstates, which can be subject to fluctuations (instability or inhomogeneity of the magnetic field). This leads to the loss of the phase relationship, i.e. dephasing, on a timescale called (reversible) *transversal relaxation time* T_2^*. This effect can be partially suppressed by introducing well-defined spin-flips, which reverse the phase evolution of the ensemble. The resulting re-phasing is called a spin-echo [68] and can be used for increasing the useful coherence time for certain applications. This technique works very well as long as the field value during the rephasing period is the same as during the dephasing. Field changes which are faster than the rephasing period still lead to relaxation. The corresponding time constant is the transversal relaxation time T_2. Usually the relaxation times behave like $T_2^* < T_2 < T_1$.

The principles known from NMR experiments are well applicable to the quickly evolving field of quantum information processing with single ions and atoms [69, 70, 71]. The achievable coherence times depend on the choice of the states used for encoding the qubit. As the atomic states typically have a magnetic moment (of the order of Bohr's magneton μ_B), a typical limit of few $100\,\mu$s is given by the stability of the ambient magnetic fields. If special care is taken for the shielding of magnetic fields or if magnetically insensitive (clock) states are used, the coherence time increases to ms or even several seconds [72, 73].

In our case the qubit is formed by the two hyperfine Zeeman states $|F = 1,\, m_F = \pm 1\rangle$ of the $F = 1$ hyperfine ground level in ^{87}Rb. As this system has overall angular momentum 1, the additional Zeeman state $|F = 1,\, m_F = 0\rangle$ makes the temporal dynamics of such "qutrit" more complex

compared to a spin-$\frac{1}{2}$ system. This chapter studies the properties of this system, its dynamics, and the mechanisms leading to decoherence.

4.2. Mechanisms leading to dephasing

In this section I will consider the effects which influence the atomic qutrit, i.e. the Zeeman substates of the $F = 1$ hyperfine ground level. These effects lead to a change of the quantum state and ultimately to the loss of coherence. One has to distinguish the decoherence in the common sense [75], i.e. entanglement of the system with the environment, from dephasing, which is due to classical fluctuations. Under conditions of our experiment the dephasing will be the dominating effect, mainly caused by external magnetic fields and interaction with the light of the dipole trap.

Scattering of the dipole trap light

Despite the far off-resonant frequency of the dipole trap light, the atom has a finite probability to scatter photons. In general this would lead to a change in the atomic state and thus to decoherence. However, due to a destructive interference effect of the $D1$ and $D2$ transitions, the incoherent (state-changing) scattering probability is strongly suppressed. It can be calculated using second-order perturbation method (originally Kramers-Heisenberg formula) and adding up all relevant transition amplitudes for the state-changing transitions [76]. It turns out that the sum of transition amplitudes for the $D1$ and $D2$ line have an equal magnitude, but opposite sign. The residual incoherent scattering rate arises from the difference of detunings and is given by :

$$\Gamma_{incoh} = \frac{3c^2\omega^3}{4\hbar}\left(\frac{\Gamma_D}{\omega_D^3}\right)^2 \left|\frac{1}{\Delta_{D1}} - \frac{1}{\Delta_{D2}}\right|^2 \cdot I \tag{4.1}$$

where ω is the angular frequency of the dipole trap light, I its intensity, Γ_D/ω_D^3 is the ratio of the natural line-width to the third power of the transition frequency (this ratio is equal for the $D1$ and $D2$ transition), and $\Delta_D = \omega_D - \omega$ are the detunings of the dipole trap light frequency with respect to the corresponding atomic transition. For our trapping parameters ($\lambda = 856\,\mathrm{nm}$, $I = 1.56 \cdot 10^9\,\mathrm{W/m^2}$) this gives $0.11\,\mathrm{Hz}$ for an atom at the bottom of the trap. This has to be compared to the total scattering rate

$$\Gamma_{total} = \frac{3c^2\omega^3}{4\hbar}\left(\frac{\Gamma_D}{\omega_D^3}\right)^2 \left|\frac{1}{\Delta_{D1}} + \frac{2}{\Delta_{D2}}\right|^2 \cdot I \tag{4.2}$$

giving $17.8\,\mathrm{Hz}$. Thus the scattering is predominantly state-preserving and does not limit the coherence in our experiment. The effect of hyperfine state coherence being larger than expected from the scattering rate was first demonstrated in [77]. The scattering gives rise to what is called decoherence in its original sense, as in this case the incoherently scattered photon carries information about the atomic state (its wavelength and/or polarization is changed). This leads to entanglement of the atomic system with the environment (whose state is in general unknown) and therefore the state of the atomic system becomes mixed.

Zeeman energy shift

The substates which form the atomic qubit are susceptible to magnetic fields (Zeeman effect). They possess a magnetic moment $\mu = \mu_B \cdot g_F \cdot m_F$, where $\mu_B = \hbar \cdot 2\pi \cdot 1.4\,\mathrm{MHz/G}$ is the Bohr magneton

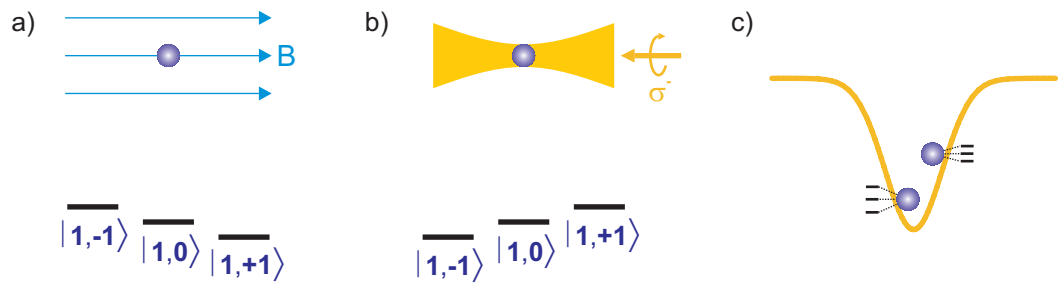

Figure 4.1.: Effects which induce energy splitting of the Zeeman sublevels. a) A magnetic field induces state-dependent Zeeman shift. b) Circularly polarized dipole trap light leads to a state-dependent light-shift, which also depends on the position in the trap (c).

and $g_F = -1/2$ is the Landé factor of the $F = 1$ level. For a magnetic field applied along the quantization axis this leads to a Zeeman energy shift

$$\Delta E_{Zeeman} = \mu_B \cdot g_F \cdot m_F \cdot B_z \tag{4.3}$$

For example a magnetic field $B_z = 10\,\mathrm{mG}$ (this is the order of magnitude for the typical fields in the experiment) gives rise to an energy splitting between the $|F = 1,\, m_F = \pm 1\rangle$ states of $14\,\mathrm{kHz}$. The magnetic field leads to time evolution (Larmor precession) of the atomic spin which will be studied in section 4.3.

Vector light-shift

The dipole trap is based on the light-induced energy shift of the atomic ground levels. For trapping light detuned far from any atomic transition this energy shift is given by

$$\Delta E_d(\vec{x}) = -\frac{\pi c^2}{2}\frac{\Gamma_D}{\omega_D^3}\left(\frac{1 - \mathcal{P} g_F m_F}{\Delta_{D1}} + \frac{2 + \mathcal{P} g_F m_F}{\Delta_{D2}}\right) I(\vec{x}) \tag{4.4}$$

where $\mathcal{P} = 0$ for π-polarization (linear along quantization axis) and $\mathcal{P} = \pm 1$ for $\sigma^{\pm}$ polarization (right- or left-circular). For linear (π) polarization this energy shift is equal for all substates of the ground level and is therefore ideally suited as a (state-independent) trapping potential (see Eq. (2.2)). However, in the experiment it is not possible to ensure ideal linear polarization of the dipole trap light (in our case mainly due to the birefringence of the vacuum glass-cell). A certain circular admixture is present leading to a state-dependent energy shift (vector light-shift) which is given by

$$\Delta E_\sigma(\vec{x}) = \mathcal{P}\frac{\pi c^2}{2}\frac{\Gamma_D}{\omega_D^3}\left(\frac{1}{\Delta_{D1}} - \frac{1}{\Delta_{D2}}\right) g_F \cdot m_F \cdot I_\sigma(\vec{x}) \tag{4.5}$$

with $I_\sigma(\vec{x})$ being the (local) intensity of circularly polarized light. This expression is equivalent to the effect of a magnetic field oriented along the quantization axis z. In contrast to an external magnetic field which can be considered constant over the volume of the dipole trap, the energy shift depends on the local light intensity. Thermal motion of the atom in the trap will thus lead to an oscillation of the light-shift. Further details considering this important effect are given in section 4.4.4 and appendix C.

4.3. Evolution of a spin-1 system in an effective magnetic field

The atomic state evolution, which is induced by the external field, is an important factor in the experiment. While evolution in a constant field is predictable and does not lead to uncontrolled dephasing, field fluctuations will lead after a certain time to a completely random state. In order to quantify these effects it is necessary to study the details of the evolution.

The relevant dynamics in the $F = 1$ subspace is given by the evolution in an *effective magnetic field* which is composed of the real external magnetic field and the effect of the circularly polarized dipole trap light:

$$\vec{B}_{eff}(\vec{x}) = \vec{B} + \mathcal{P} \cdot \frac{1}{\mu_B} \frac{\pi c^2}{2} \frac{\Gamma_D}{\omega_D^3} \left(\frac{1}{\Delta_{D1}} - \frac{1}{\Delta_{D2}} \right) \cdot I_\sigma(\vec{x}) \cdot \vec{\mathrm{e}}_z \tag{4.6}$$

The Hamiltonian is given by the interaction of the magnetic moment of the system with the (effective) magnetic field $\vec{B}_{eff}$:

$$\hat{H} = \vec{B}_{eff} \cdot \frac{\mu_B g_F}{\hbar} \hat{\vec{F}} \tag{4.7}$$

where $\hat{\vec{F}}$ is the operator of the (hyperfine) angular momentum for the $F = 1$ space. We write the components of the field

$$\vec{B}_{eff} = B_{eff}(b_x \vec{\mathrm{e}}_x + b_y \vec{\mathrm{e}}_y + b_z \vec{\mathrm{e}}_z)$$

and set for convenience

$$b_x = \sqrt{1 - b_z^2}\cos(\phi), \quad b_y = \sqrt{1 - b_z^2}\sin(\phi).$$

Then we get the effective field Hamiltonian in the basis $\{|1,+1\rangle_z, |1,0\rangle_z, |1,-1\rangle_z\}$[1]:

$$\begin{aligned} \hat{H} = B_{eff} \cdot \mu_B g_F \begin{pmatrix} b_z & \frac{1}{\sqrt{2}}(b_x - ib_y) & 0 \\ \frac{1}{\sqrt{2}}(b_x + ib_y) & 0 & \frac{1}{\sqrt{2}}(b_x - ib_y) \\ 0 & \frac{1}{\sqrt{2}}(b_x + ib_y) & -b_z \end{pmatrix} = \\ = \hbar\omega_L \begin{pmatrix} b_z & \frac{1}{\sqrt{2}}\sqrt{1-b_z^2}e^{-i\phi} & 0 \\ \frac{1}{\sqrt{2}}\sqrt{1-b_z^2}e^{i\phi} & 0 & \frac{1}{\sqrt{2}}\sqrt{1-b_z^2}e^{-i\phi} \\ 0 & \frac{1}{\sqrt{2}}\sqrt{1-b_z^2}e^{i\phi} & -b_z \end{pmatrix} \end{aligned} \tag{4.8}$$

where $\omega_L := \frac{1}{\hbar}\mu_B g_F B_{eff}$ is the *Larmor frequency*. The eigenstates of this Hamiltonian are

$$\begin{aligned} |\Phi_{+1}\rangle &= \begin{pmatrix} \frac{1}{2}(1+b_z)e^{-i\phi} \\ \frac{1}{\sqrt{2}}\sqrt{1-b_z^2} \\ \frac{1}{2}(1-b_z)e^{i\phi} \end{pmatrix} \\ |\Phi_0\rangle &= \begin{pmatrix} -\frac{1}{\sqrt{2}}\sqrt{1-b_z^2}e^{-i\phi} \\ b_z \\ \frac{1}{\sqrt{2}}\sqrt{1-b_z^2}e^{i\phi} \end{pmatrix} \\ |\Phi_{-1}\rangle &= \begin{pmatrix} \frac{1}{2}(1-b_z)e^{-i\phi} \\ -\frac{1}{\sqrt{2}}\sqrt{1-b_z^2} \\ \frac{1}{2}(1+b_z)e^{i\phi} \end{pmatrix} \end{aligned} \tag{4.9}$$

[1] The subscript identifies the quantization axis. For states without subscript the standard quantization axis z is assumed.

with corresponding eigenvalues $+\hbar\omega_L$, 0, $-\hbar\omega_L$ respectively.

The time evolution of the eigenstates for constant $\vec{B}_{eff}$ is given by $|\Phi_{\pm1}\rangle \rightarrow |\Phi_{\pm1}\rangle\, e^{\mp i\omega_L t}$, whereas $|\Phi_0\rangle$ acquires no phase. Therefrom the evolution of a state $|\Psi\rangle\,(0) = c_{-1}\,|\Phi_{-1}\rangle + c_0\,|\Phi_0\rangle + c_{+1}\,|\Phi_{+1}\rangle$ is given by

$$|\Psi\rangle\,(t) = c_{-1}\,|\Phi_{-1}\rangle\, e^{i\omega_L t} + c_0\,|\Phi_0\rangle + c_{+1}\,|\Phi_{+1}\rangle\, e^{-i\omega_L t} \tag{4.10}$$

This allows to calculate the time evolution for any state in a (constant) field pointing in an arbitrary direction. An obvious property of this result is that the evolution is periodic with the period $T = \frac{2\pi}{\omega_L}$.

To illustrate the precession of the spin-1 system we consider the case $|\Psi\rangle\,(0) = |1,+1\rangle_z$ and field along x-axis ($b_x = 1$, $b_y, b_z = 0$, $\phi = 0$). The state after time t is given by

$$|\Psi\rangle\,(t) = \frac{1}{2}(\cos(\omega_L t) + 1)\,|1,+1\rangle_z - \frac{i}{\sqrt{2}}\sin(\omega_L t)\,|1,0\rangle_z + \frac{1}{2}(\cos(\omega_L t) - 1)\,|1,-1\rangle_z$$

After quarter of the period the state becomes $|\Psi\rangle\,(\frac{T}{4}) = \frac{1}{2}\,|1,+1\rangle_z - \frac{i}{\sqrt{2}}\,|1,0\rangle_z - \frac{1}{2}\,|1,-1\rangle_z = |1,-1\rangle_y$. In the same way one can show $|\Psi\rangle\,(\frac{T}{2}) = |1,-1\rangle_z$ and $|\Psi\rangle\,(\frac{3}{2}T) = |1,+1\rangle_y$. The spin performs a rotation around the field axis in complete analogy to precession of a classical magnetic dipole. This process can be observed experimentally, see Fig. 4.12(a) in Sec. 4.6.1.

4.4. A model for dephasing

The time evolution described in the previous section assumes a single realization of the experiment under well-defined conditions, in particular a constant effective magnetic field B_{eff}. However, such conditions can hardly be achieved in the experiment. Depending on how quickly the field varies, two scenarios are possible. If the field fluctuations are slow, the field can be considered constant for the duration of a single experiment ($100\,\mathrm{ns}..200\,\mu\mathrm{s}$) and the atomic state will evolve according to Eq. (4.10). However, the field will change from experiment to experiment which leads to different final states. The observed average of final states washes out (shot-to-shot dephasing). For fast field fluctuations, where the field changes within a single realization of the experiment, the evolution of the state will deviate from the mean trajectory following the change of the field. With increasing frequency of the fluctuations the deviation will decrease. This section considers two analytic models which account for the scenarios of slowly and quickly varying field.

4.4.1. Static field model

We consider a model where the effective field $\vec{B}_{eff}$ is constant during a single realization of the experiment but differs between repeated experimental shots (which is a realistic situation for a slowly varying field). Let $p_j(B_j)$, $j \in \{x, y, z\}$ be the normalized distributions for the components of the field. At the beginning of each experiment a certain state is prepared. It evolves in the field $\vec{B}_{eff}$ according to Eq. (4.10) during time t into the state $\left|\Psi_{\vec{B}}(t)\right\rangle$. At the end of each experiment the projection of the final state $\left|\Psi_{\vec{B}}(t)\right\rangle$ onto a certain state $|\Psi_a\rangle$ is measured. The measured population $p(|\Psi_a\rangle)$ is then an average of all possible evolutions given by the effective field distributions:

$$p(|\Psi_a\rangle)(t) = \int dB_x dB_y dB_z \left(p_x(B_x)p_y(B_y)p_z(B_z)\left|\left\langle\Psi_a|\Psi_{\vec{B}}(t)\right\rangle\right|^2\right) \tag{4.11}$$

In most cases the integral in (4.11) is not analytic but can be calculated numerically.

First let us consider the case of fluctuations only along the quantization axis z with the mean value of the field equal to zero (i.e. $B_x = B_y = 0$, $\bar{B}_z = 0$). Then the time evolution of an initially prepared superposition state $|\Psi\rangle(0) = \frac{1}{\sqrt{2}}(|1,-1\rangle + |1,+1\rangle)$ is given by

$$|\Psi\rangle(t) = \frac{1}{\sqrt{2}}\left(|1,-1\rangle + e^{i2\omega_L t}|1,+1\rangle\right) \tag{4.12}$$

with $\omega_L = \frac{1}{\hbar}\mu_B g_F B_z$ being the Larmor frequency for a given B_z. The projection of the resulting state onto the initially prepared one ($|\Psi_a\rangle = \frac{1}{\sqrt{2}}(|1,-1\rangle + |1,+1\rangle)$) is then

$$|\langle\Psi_a|\Psi_B(t)\rangle|^2 = \frac{1}{4}\left|1 + e^{i2\omega_L t}\right|^2 = \frac{1}{2}(1+\cos(2\omega_L t)) \tag{4.13}$$

Averaging over many experimental shots according to the distribution of B_z gives

$$p(|\Psi_a\rangle)(t) = \frac{1}{2} + \frac{1}{2}\int dB_z p_z(B_z)\cos(2\omega_L(B_z)t)$$

If we now assume a Gaussian distribution of the magnetic field

$$p_z(B_z) = \frac{1}{\sqrt{\pi}\Delta B_z}\exp\left(-\frac{B_z^2}{\Delta B_z^2}\right)$$

the average projection becomes

$$\begin{aligned} p(|\Psi_a\rangle)(t) = \frac{1}{2} + \frac{1}{2\sqrt{\pi}\Delta B_z}\int dB_z \exp\left(-\frac{B_z^2}{\Delta B_z^2}\right)\cos(\frac{2}{\hbar}\mu_B g_F B_z t) \\ = \frac{1}{2} + \frac{1}{2}\exp\left(-\left(\frac{1}{\hbar}\mu_B g_F \Delta B_z t\right)^2\right) \end{aligned} \tag{4.14}$$

The projection onto the initially prepared state (i.e. the fidelity) drops as a function of time like a gaussian, approaching a final value of 0.5 (see Fig. 4.2). This means that on average the superposition state loses its phase relation when observed over many repetitions - it dephases. This process happens on the timescale which is determined by the width of the effective field distribution ΔB_z. From this one gets the $\frac{1}{e}$ dephasing time for one-dimensional fluctuations along the quantization axis

$$T_2^* = \frac{\hbar}{\mu_B g_F}\frac{1}{\Delta B_z} \tag{4.15}$$

which is equivalent to the transversal coherence time in an NMR-system. In this case the spin-1 system behaves like a spin-$\frac{1}{2}$ system, the states $|1,-1\rangle$ and $|1,+1\rangle$ remain unchanged as they are eigenstates of the field Hamiltonian and the evolution is confined in the subspace $\{|1,-1\rangle, |1,+1\rangle\}$.

In a second example let us consider the evolution of the state $|1,+1\rangle$ in a field fluctuating along the x-axis. Similar to the previous example, the projection of the final state after evolution in the field onto the initial state is given by

$$\left|\langle\Psi_a|\Psi_{\vec{B}}(t)\rangle\right|^2 = \frac{1}{4}(\cos(\omega_L t)+1)^2 \tag{4.16}$$

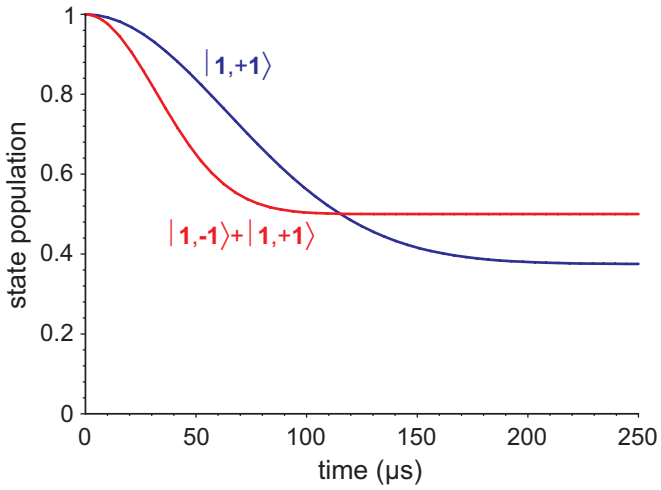

Figure 4.2.: Dephasing of a quantum state caused by fluctuations of the magnetic field. Red line: population of the state $\frac{1}{\sqrt{2}}(|1,-1\rangle + |1,+1\rangle)$ as a function of time in a fluctuating field oriented along the z-axis (gaussian distribution, full-width at $\frac{1}{e}$: $2\Delta B_z = 10\,\mathrm{mG}$). Blue line: dephasing of the state $|1,+1\rangle$ in a fluctuating field oriented along the x-axis (gaussian distribution, full-width at $\frac{1}{e}$: $2\Delta B_z = 10\,\mathrm{mG}$).

By averaging over the gaussian distribution of B_x we find

$$p(|\Psi_a\rangle)(t) = \frac{1}{4\sqrt{\pi}\Delta B_x}\int dB_x \exp\left(-\frac{B_x^2}{\Delta B_x^2}\right)(\cos(\frac{1}{\hbar}\mu_B g_F B_x t)+1)^2$$
$$= \frac{3}{8} + \frac{5}{8}\exp\left(-\left(\frac{1}{2}\frac{1}{\hbar}\mu_B g_F \Delta B_x t\right)^2\right) \quad (4.17)$$

The state population decays here half as fast and approaches the final value of $\frac{3}{8}$ as the evolution leaves the subspace $\{|1,-1\rangle, |1,+1\rangle\}$ (Fig. 4.2).

4.4.2. Dynamic field effects

The previous consideration assumed a constant magnetic field during each realization of the experiment. Under realistic conditions field fluctuations can be present which are considerably fast, therefore it is important to consider what happens if the magnetic field changes during a single experiment.

We consider the evolution of a superposition state $|\Psi\rangle(0) = \frac{1}{\sqrt{2}}(|1,-1\rangle + |1,+1\rangle)$ in an effective magnetic field along the quantization axis (z) which is sinusoidally modulated at a single frequency Ω, i.e. $B(t) = \bar{B} + \delta B_\Omega \sin(\Omega t + \phi_0)$. This leads to a modulation of the Larmor frequency

$$\omega_L(t) = \bar{\omega}_L + A_\Omega \sin(\Omega t + \phi_0) \quad (4.18)$$

where $\bar{\omega}_L$ is the average Larmor frequency, $A_\Omega = \frac{1}{\hbar}\mu_B g_F \delta B_\Omega$ is the amplitude of the modulation and ϕ_0 its phase offset. During the time t the initially prepared state will evolve as

$$|\Psi\rangle(t) = \frac{1}{\sqrt{2}}\left(|1,-1\rangle + e^{i\Phi(t)}|1,+1\rangle\right)$$

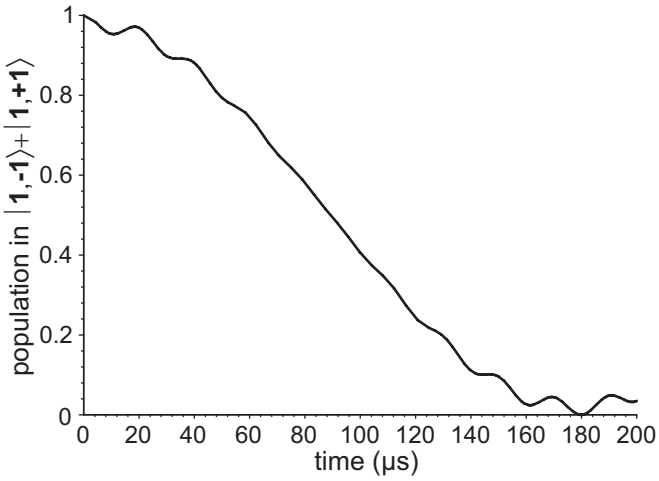

Figure 4.3.: Effect of modulated Larmor frequency. The state $\frac{1}{\sqrt{2}}(|1,-1\rangle + |1,+1\rangle)$ undergoes Larmor precession in a field along the z-axis with an average value $\bar{B}_z = 2\,\mathrm{mG}$. The amplitude of the modulation is $\delta B_z = 10\,\mathrm{mG}$, the modulation frequency $\Omega = 2\pi \cdot 50\,\mathrm{kHz}$ giving together $\frac{A_\Omega}{\Omega} = 0.14$.

with the phase $\Phi(t)$ given by

$$\Phi(t) = 2\int_0^t dt' \omega_L(t') = 2\left(\bar{\omega}_L t - \frac{A_\Omega}{\Omega}\big(\cos(\Omega t + \phi_0) - \cos(\phi_0)\big)\right) \tag{4.19}$$

As the phase offset ϕ_0 is in general unknown and different for each realization of the experiment, one has to average over ϕ_0 to get the expected population in the analyzed state $|\Psi_a\rangle = \frac{1}{\sqrt{2}}(|1,-1\rangle + |1,+1\rangle)$:

$$\begin{aligned} p(|\Psi_a\rangle)(t) &= \frac{1}{2\pi}\int_0^{2\pi} d\phi_0 \frac{1}{4}\left|1 + e^{i\Phi(t)}\right|^2 \\ &= \frac{1}{4\pi}\int_0^{2\pi} d\phi_0 \left[1 + \cos\left(2\Big(\bar{\omega}_L t - \frac{A_\Omega}{\Omega}\big(\cos(\Omega t + \phi_0) - \cos(\phi_0)\big)\Big)\right)\right] \end{aligned}$$

This integral is not analytic, but for small modulation amplitudes $\frac{A_\Omega}{\Omega} \ll 1$ it can be expanded into Taylor series up to the order 2 giving

$$\begin{aligned} p(|\Psi_a\rangle)(t) &= \frac{1}{4\pi}\int_0^{2\pi} d\phi_0 \Big[1 + \cos(2\bar{\omega}_L t)\big(1 - \frac{1}{2}\Big(2\frac{A_\Omega}{\Omega}\big(\cos(\Omega t + \phi_0) - \cos(\phi_0)\big)\Big)^2\big) \\ &\qquad + \sin(2\bar{\omega}_L t)\Big(2\frac{A_\Omega}{\Omega}\big(\cos(\Omega t + \phi_0) - \cos(\phi_0)\big)\Big)\Big] = \\ &= \frac{1}{2}\left(1 + \cos(2\bar{\omega}_L t)\Big(1 - 2\frac{A_\Omega^2}{\Omega^2}\big(1 - \cos(\Omega t)\big)\Big)\right) = \frac{1}{2}\left(1 + \cos(2\bar{\omega}_L t)\Big(1 - \big[2\frac{A_\Omega}{\Omega}\sin(\frac{\Omega t}{2})\big]^2\Big)\right) \end{aligned}$$

The system undergoes Larmor precession at expected frequency $2\bar{\omega}_L$ with small oscillations around the main trajectory (Fig. 4.3). Despite the fact that the phase ϕ_0 is unknown, the modulation of the Larmor frequency ω_L leads to a periodic modulation of the measured state population at frequency Ω.

The magnitude of these deviations scales as $\left(\frac{A_\Omega}{\Omega}\right)^2$, in particular it drops with increasing modulation frequency. The response of the system to a change of the external field happens at the timescale of the Larmor frequency and can not follow fluctuations which are faster.

The modulation at a single frequency Ω does not lead to dephasing (since the oscillation is periodic), but rather to small and reversible deviations from the expected trajectory. If now a spectrum of modulation frequencies is present, the oscillations at different frequencies will wash out on average in a single realization of the experiment. However, the strong suppression of the dynamic effect with increasing modulation frequency Ω and the typically small magnitude of fast field fluctuations in the experiment make this dynamic dephasing negligible compared to that caused by the (quasi-)static fields.

4.4.3. The role of a magnetic guiding field

As was described in previous sections, external magnetic fields give rise to an (in general unwanted) evolution of the atomic quantum state. Therefore, the ordinary mode of operation of the experiment is to compensate the external fields. Additionally, for the generation of polarization entanglement between the atom and the photon, the energy splitting of the qubit states $|1, \pm 1\rangle$ has to be small compared to the natural linewidth of the $D2$ transition. This condition is ideally fulfilled in absence of a magnetic field, where the qubit states are degenerate. Unfortunately in this case the system is sensitive to field fluctuations from any direction.

However, if a strong magnetic field is applied from a certain direction the situation changes. Fluctuations along the field axis will not change the direction of the field and the absolute value will behave as $B \rightarrow B + \Delta B_\parallel$ (see Fig. 4.4(a)). In the same way the Larmor frequency will be modified. On the other hand fluctuations orthogonal to the guiding field slightly rotate the field axis while the absolute value behaves as $B \rightarrow \sqrt{B^2 + \Delta B_\perp^2}$. The stronger the guiding field B the smaller is the effect of transversal fluctuations. We conclude that the sensitivity of the system to field fluctuations orthogonal to the guiding field axis gets strongly suppressed, while the sensitivity to fluctuations along the field axis remains unchanged. Another view of this effect is that the eigenstates of the field Hamiltonian depend only on the direction of the field which gets more stable with increasing B.

The stabilizing effect of a guiding field gives an option for increasing the stability of the atomic state by applying a field e.g. along the quantization axis. In this case the qubit states $|1, \pm 1\rangle$ are eigenstates of the field Hamiltonian and therefore the system can not leave the qubit subspace. The magnitude of the guiding field has to be larger than the fluctuations, however, the energy splitting

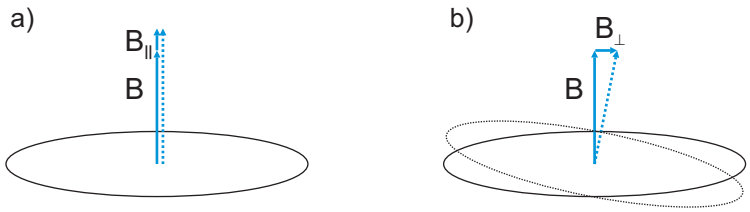

Figure 4.4.: Guiding magnetic field. a) Fluctuations along the guiding field axis add linearly, the effect is independent of the magnitude of the guiding field. b) Fluctuations orthogonal to the guiding field axis add quadratically and rotate the vector of the field, the effect gets smaller with increasing magnitude of the guiding field.

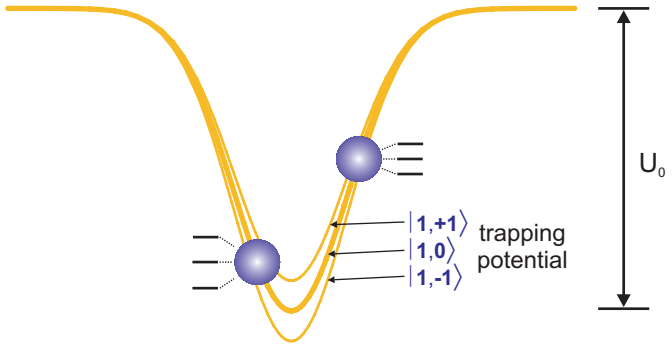

Figure 4.5.: A circular admixture of dipole trap light induces a position-dependent energy shift of the Zeeman states $|1,0\rangle$,$|1,\pm1\rangle$.

$2\Delta E$ of the qubit states $|1,\pm1\rangle$ has to be small compared to the natural linewidth. The disadvantage of the application of a guiding field is the continuous Larmor precession of the superposition states $\frac{1}{\sqrt{2}}\left(|1,-1\rangle + e^{i\phi}\,|1,+1\rangle\right)$.

An interesting point is, how the energy splitting between the qubit states influences the time evolution of the entangled atom-photon state $|\Psi^+\rangle = \frac{1}{\sqrt{2}}\left(|1,-1\rangle\,|\sigma^+\rangle + |1,+1\rangle\,|\sigma^-\rangle\right)$. For any energy splitting $2\Delta E$ the phase evolution of the atomic terms ($|1,\pm1\rangle\,e^{\pm i\Delta E t}$) exactly cancels the evolution of the photonic terms ($|\sigma^\pm\rangle\,e^{\mp i\Delta E t}$). Therefore, for constant ΔE the entangled state shows no time evolution. As a consequence, the guiding field does not influence the entangled state as long as no measurement is performed on the atom or the photon. After the state of the photon is measured, however, the state of the remaining atom will undergo Larmor precession.

4.4.4. Effect of the dipole trap upon the atomic state

As was already introduced in section 4.2, circularly polarized light of the dipole trap induces a state-dependent energy shift which is equivalent to a magnetic field applied along the quantization axis. Due to its finite temperature the atom moves in the dipole trap. This leads to a distribution of the induced energy shifts and therefore to dephasing comparable to a fluctuating magnetic field. The magnitude of this effect depends on two parameters.

The first parameter is the fraction of the circularly polarized light in the trap region. Due to the birefringence of the vacuum glass cell and polarization rotation on reflection at optical components, the uncertainty of the final beam polarization is of the order of $1\%..2\%$. Additional polarization effects arise from the tight focusing of the dipole trap beam (see App. D).

The second parameter is the distribution of the effective magnetic field caused by the motion of the atom in the trap. For typical experiments, which are much shorter than the transversal oscillation period ($\sim 45\,\mu$s for our trap parameters), the atom can be considered static at a certain position in the trap. This leads to a non-ergodic behavior where the average value of the light-shift is not representative and the exact distribution which includes the details of atomic motion must be considered.

We note that the optically induced magnetic field at a given position in the dipole trap is directly proportional to the potential energy of the atom. This results from the fact that the state-independent energy shift (constituting the trapping potential), as well as the state-dependent energy shift (which generates the effective magnetic field) are both proportional to the trapping light intensity at the position of the atom. Therefore the distribution of the effective magnetic field is the same as the potential

energy distribution. As the oscillation of the atom in the trap can be considered harmonic in good approximation, the distribution of potential energy $p(U)$ can be calculated explicitly (see App. C). For an atom in thermal equilibrium in a 3-dimensional harmonic trap the result is given by Eq. (C.4):

$$p(U) = \frac{2}{\sqrt{\pi}(k_B T)^{3/2}} \sqrt{U} \exp(-\frac{U}{k_B T})$$

where the zero point of the (non-negative) potential energy U is assumed at the bottom of the trap, T is the temperature of the atom, and k_B is the Boltzmann constant. In order to get the relation between the potential energy and the resulting effective magnetic field we calculate the maximal optically induced magnetic field at the bottom of the trap according to Eq. (4.5):

$$B_{\sigma,0} = \frac{1}{\mu_B} \frac{\pi c^2}{2} \frac{\Gamma_D}{\omega_D^3} \left(\frac{1}{\Delta_{D1}} - \frac{1}{\Delta_{D2}} \right) F_\sigma I_0 \tag{4.20}$$

where I_0 is the maximal intensity of the trapping light and $F_\sigma = I_\sigma / I$ is the fraction of the circular polarization. Using the maximal potential depth U_0 induced by the linearly polarized trap light we get

$$B_\sigma = B_{\sigma,0} \frac{U_0 - U}{U_0}$$

The distribution of the optically induced magnetic field for an atom in thermal equilibrium is then

$$p(\Delta B_\sigma) = \frac{2}{\sqrt{\pi}(\frac{B_{\sigma,0}}{U_0})^{3/2}(k_B T)^{3/2}} \sqrt{\Delta B_\sigma} \exp(-\frac{\frac{U_0}{B_{\sigma,0}} \Delta B_\sigma}{k_B T}) \tag{4.21}$$

with $\Delta B_\sigma = B_{\sigma,0} - B_\sigma$. It is exactly valid for experimental duration shorter than the transversal oscillation period of $\sim 45\,\mu$s. For longer experimental times which are still shorter than the longitudinal oscillation period ($\sim 800\,\mu$s) transition takes place into a regime where the distribution of the optically induced magnetic field is governed by one-dimensional non-ergodic distribution Eq. (C.2) and the transversal oscillation induces a modulation of state as described in Sec. 4.4.2. This behavior shall not be considered here.

Using the distribution (4.21) it is possible to simulate the dephasing effects induced by the dipole trap. For the initially prepared superposition state $\frac{1}{\sqrt{2}} \left(|1,-1\rangle + e^{i\phi} |1,+1\rangle \right)$ one can explicitly calculate the time evolution in presence of such field fluctuations. After the evolution within time t the probability to find the atom in the initial superposition is given by

$$p(|\Psi_a\rangle)(t) = \int_0^\infty dB_\sigma p(\Delta B_\sigma) \cos(\omega_L (\Delta B_\sigma + B_z))^2$$

where B_z is the (constant) offset field along the quantization axis.

As an example we assume an atomic temperature $T = 0.15\,\mathrm{mK}$ and maximal trap depth $U_0 = 0.6\,\mathrm{mK}$. For a fraction of circularly polarized light of $F_\sigma = 1\%$ the distribution of the effective magnetic field is shown in Fig. 4.6(a). The evolution of a superposition state for two different offset fields is shown in Fig. 4.6b) and c). It is important to note that an offset field along the quantization axis z has no stabilizing effect upon the dephasing time. The apparently faster dephasing in the case of zero offset field is misleading as the projection onto the original state is not always a sufficient measure for the coherence. In this case, parallel to dephasing, a rotation into conjugate states $\frac{1}{\sqrt{2}} \left(|1,-1\rangle \pm e^{i\phi \pm \frac{\pi}{2}} |1,+1\rangle \right)$ takes place on a similar timescale, which makes it difficult to distinguish Larmor precession from dephasing. In presence of an offset field, Fig. 4.6(c), the oscillation is

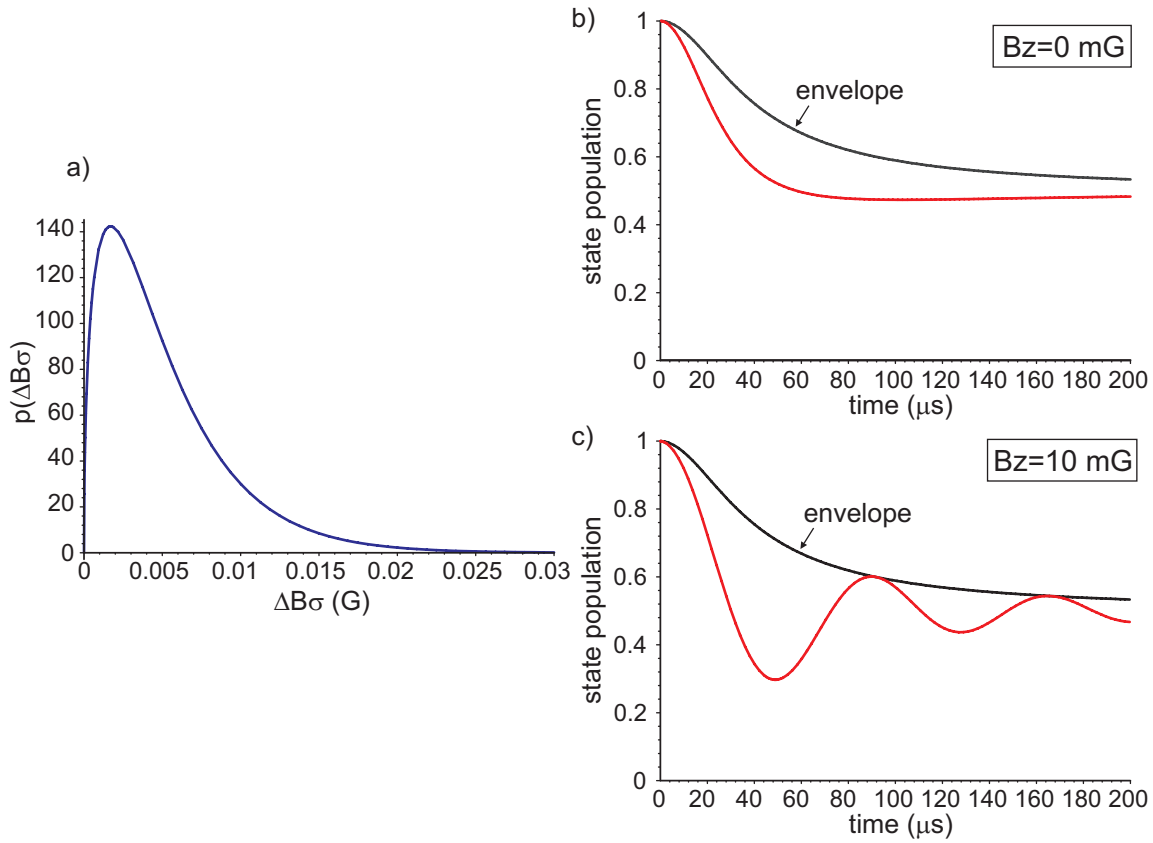

Figure 4.6.: Effect of the fluctuating effective magnetic field caused by the motion of the atom in the trap in presence of circularly polarized trap light. a) Thermal distribution of the effective magnetic field ΔB_σ (assumed parameters: maximal trap depth $U_0 = 0.6\,\mathrm{mK}$, atomic temperature is $T = 0.15\,\mathrm{mK}$, fraction of circularly polarized light $F_\sigma = 1\%$). b) Time evolution of the state $\frac{1}{\sqrt{2}}\left(|1,-1\rangle + e^{i\phi}\,|1,+1\rangle\right)$ under described conditions without offset field. c) The same in presence of an offset field $B_z = 10\,\mathrm{mG}$. The envelope which is equal for both cases is shown as the black line.

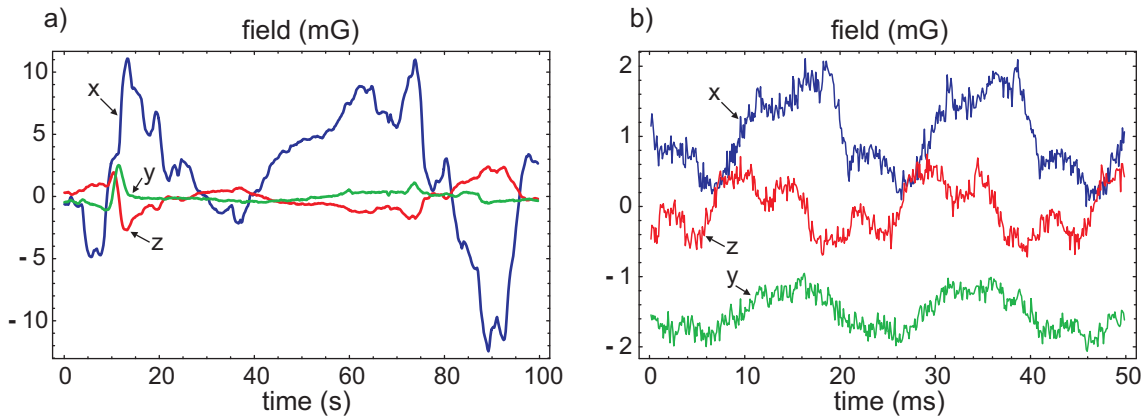

Figure 4.7.: Measurement of the ambient magnetic field in the vicinity of the atomic trap during daytime. The three axes of the field are measured simultaneously, blue: x-axis, green: y-axis, red: z-axis. a) Measurement of $100\,\mathrm{s}$, each point was averaged for $0.2\,\mathrm{s}$. b) Measurement of $50\,\mathrm{ms}$ showing short-time fluctuations, taken at an effective bandwidth of $60\,\mathrm{kHz}$. The offsets of the individual channels were arbitrarily chosen to ensure good readability of the picture.

faster than dephasing and allows to observe the decay of the envelope. The envelope of the oscillation in the considered case is given by

$$A_{env}(t) = \frac{1}{2}(1 \pm r(t)) \tag{4.22}$$

where r is the purity parameter which can be calculated from the density matrix $\hat{\rho}$ (see App. B, Eq. (B.9) and following). The resulting envelope is shown in Fig. 4.6(b),(c) as a black line and is identical in both cases as expected. This clearly shows that under typical experimental conditions the residual Larmor precession can lead to an under-estimation of the dephasing time.

4.5. Measurement and active control of magnetic fields

In the preceding sections it was shown that the quantum state of the atom is sensitive to magnetic fields. In order to quantify and to compensate the ambient magnetic fields a magnetic field probe is needed. For this purpose we use a 3-axis magneto-resistive sensor (Honeywell HMC 1053). This device incorporates three orthogonal Wheatstone bridges with embedded magneto-resistive elements. When a magnetic field is applied, the resistance of these elements changes causing an imbalance of the bridge which produces a measurable voltage difference ($10\,\mu\mathrm{V/mG}$ if the bridge is operated at $10\,\mathrm{V}$). By amplifying this signal by a factor of 100 we achieve a sensitivity of $1\,\mathrm{mV/mG}$. The important advantage of this device is its compact size ($7.4 \times 7.4 \times 2.8\,\mathrm{mm}$), which allows to position the sensor very close to the center of the atomic trap.

The sensor was placed directly on the upper surface of the glass cell, such that the vertical beams of the MOT and the push-out beam were not affected (see Fig. 2.4 and Fig. 4.9). The center of the sensor is therefore located $16\,\mathrm{mm}$ above the position of the trap and additionally displaced by $9\,\mathrm{mm}$ along the cell axis (y).

Fig. 4.7 shows a typical measurement of the ambient magnetic fields. On the long timescale (a) the most prominent feature are the strong aperiodic fluctuations on the x-axis, which are also visible

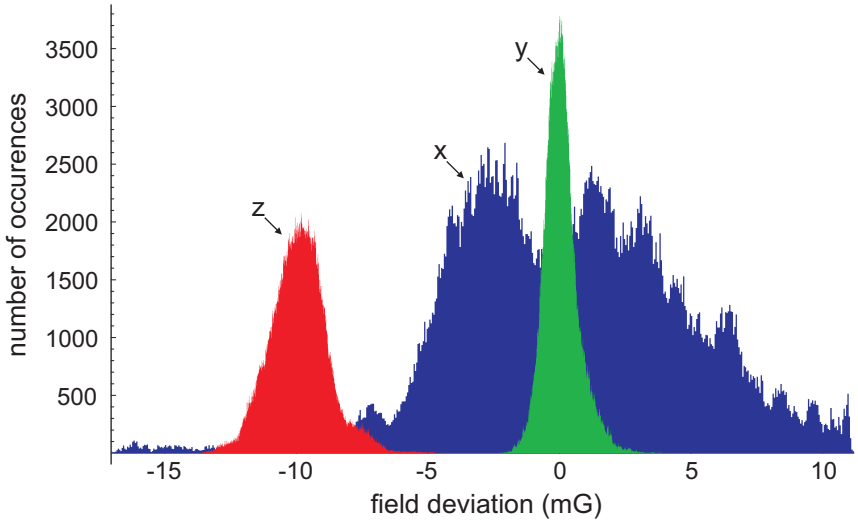

Figure 4.8.: Histogram of the magnetic field fluctuations taken from a trace of $1000\,\mathrm{s}$ during daytime. The x-, y- and z-axes are color-coded as blue, green, and red respectively. The histogram for z-axis is displaced by $10\,\mathrm{mG}$ for better readability.

on the y,z-axes, however, with smaller amplitude and inverse sign. These fluctuations are due to the currents drawn by trains of the Munich underground line. The line is located at about $60\,\mathrm{m}$ distance and about $12\,\mathrm{m}$ below the level of the laboratory. The currents are drawn from the supply line which goes parallel to the track at about $0.7\,\mathrm{m}$ distance and go back to the supply station via the (grounded) track itself. For acceleration a single train draws about $2500\,\mathrm{A}$ and gives the current back during deceleration. For a current I flowing in opposite directions over two infinitely long, parallel wires which have a separation Δr, the magnetic field at the distance r is

$$B = \frac{\mu_0}{2\pi}\left(\frac{1}{r} - \frac{1}{r+\Delta r}\right) I \approx \frac{\mu_0}{2\pi}\frac{\Delta r}{r^2} I \tag{4.23}$$

Taking $r = 61.2\,\mathrm{m}$, $\Delta r = 0.7\,\mathrm{m}$ and $I = 2500\,\mathrm{A}$ we estimate $B \approx 0.93\,\mathrm{mG}$. The total current flowing through the supply line and the track is composed of currents from several trains (depending on the number and positioning of the power supply stations it can be even all trains on the line). Since the line is heavily loaded with trains going every 5 minutes in both directions, the measured fluctuations of about $20\,\mathrm{mG}$ peak-to-peak are well explained[2]. As the field lines form closed circles around the current-carrying wire, the ratio of amplitudes between the z- and the x-axis has to correspond to the ratio of the horizontal and vertical distances between the laboratory and the underground line. This ratio ($\sim 1:5$) can be clearly seen in the graph. The y-axis, which is oriented approximately along the line, is practically unaffected.

On the short timescale, Fig. 4.7(b), the strongest contribution to the fluctuations results from the $50\,\mathrm{Hz}$ power line of the laboratory with peak-to-peak amplitudes of $1..2\,\mathrm{mG}$. The standard deviations are $0.54\,\mathrm{mG}$, $0.27\,\mathrm{mG}$ and $0.37\,\mathrm{mG}$ for the x,y,z-axes respectively. The noise with higher frequencies originates partly from the laboratory electronics and cables.

Fig. 4.8 shows the histograms of the magnetic field fluctuations. The FWHM widths of these

[2]During the night between about $1:45\,am$ and $4:00\,am$, where there is no regular traffic, the fluctuations are significantly smaller.

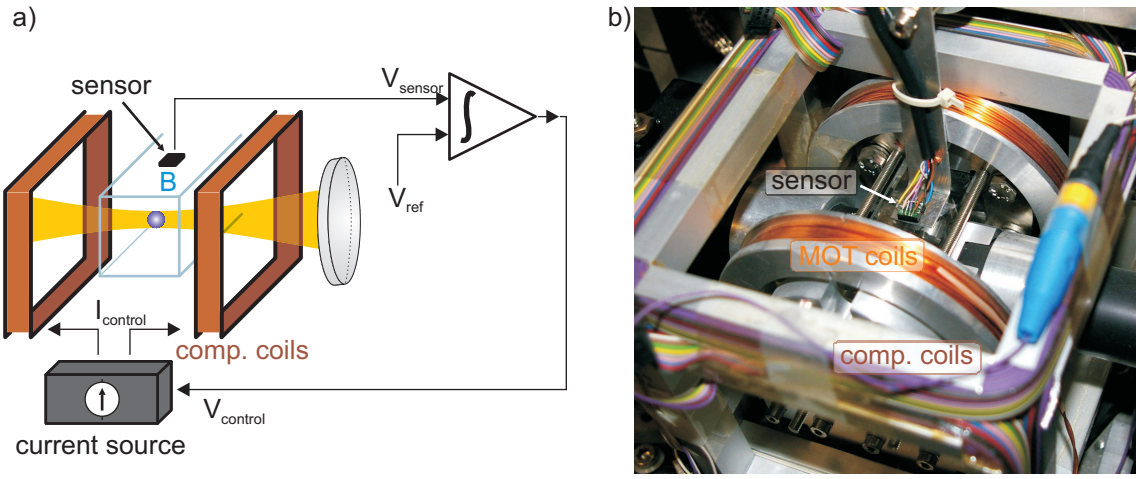

Figure 4.9.: Schematic of the active magnetic field stabilization. a) The value of the sensor is compared with the given reference, an integrating feedback circuit generates a control voltage for the current source which supplies the compensation coils. b) Picture of the setup showing the sensor located on the surface of the glass cell.

distributions are approximately $10\,\mathrm{mG}$, $1.2\,\mathrm{mG}$ and $2\,\mathrm{mG}$ for the x-, y- and z-axes respectively. Since the field fluctuations lead to dephasing of the atomic quantum state (see e.g. Fig. 4.12), and also the Larmor precession of the state has to be controlled well (already a field of $5\,\mathrm{mG}$ leads to an oscillation period of $140\,\mu\mathrm{s}$), exact control of the magnetic field is required.

4.5.1. Active control of magnetic fields

The problem of fluctuating ambient magnetic fields can be solved in two different ways. Passively one could use μ-metal shielding, i.e. a metal with a high magnetic permeability μ. Such materials prevent the magnetic field lines from entering the enclosed volume. Depending on the quality and number of the shield layers as well as positioning within the shielded volume, a suppression of external fields by a factor of 10 up to few 100 can be achieved. However, shielding of an experiment which requires good optical access is a quite complicated and expensive task.

A widely used way to avoid the influence of the magnetic field of the power-line is to trigger the experiment with its frequency ($50\,\mathrm{Hz}$ or $60\,\mathrm{Hz}$). This ensures that a certain phase of the experiment happens during a well-defined phase of the power-line oscillation. Unfortunately, this technique is only applicable in experiments where the repetition rate is smaller than the power line frequency, while in our experiment it is several orders of magnitude higher.

Our method of choice is to actively compensate the external fluctuations. This approach requires three principal components: the sensor, which measures the actual value of the field; the feedback circuit, which evaluates the deviation of the actual value from the desired value and produces a signal fed to the coils; finally the coils produce a magnetic field which compensates the deviation.

The self-made feedback circuit derives its error signal from the difference between the measured voltage of the sensor and the desired value, which is set externally by a potentiometer. This error signal is electronically with integrating time constant $\frac{1}{RC} = 1\,\mathrm{ms}$. This allows to stabilize slow drifts as well as the fluctuations due to the power line including its harmonics up to $\sim 200\,\mathrm{Hz}$. The resulting signal is fed back to the compensation coils using a controllable current source. The active control

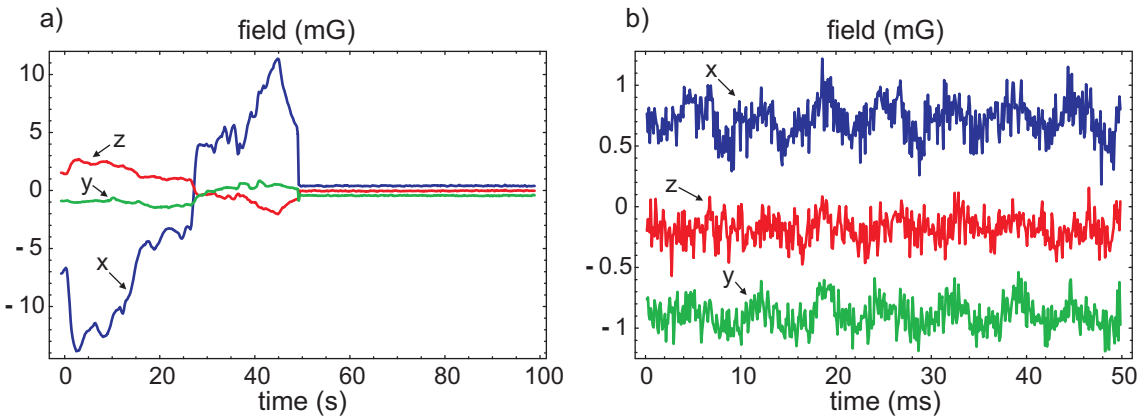

Figure 4.10.: Measurement of fluctuations of the magnetic fields in the vicinity of the atomic trap with integrated active stabilization (in-loop signal). a) Measurement of 100 s, the stabilization was switched on after 50 s. b) Measurement over 50 ms, stabilization is on. The remaining oscillation at 200 Hz are higher harmonics of the power-line frequency.

can be electronically switched on and off, it is deactivated during the atom loading stage.

Fig. 4.10 shows the field fluctuations when the active stabilization is used. The fields here are measured with the same sensor which is used for stabilization (in-loop signal). The remaining fluctuations on the long timescale (a) are negligible. On the short timescale (b) there are residual fluctuations at frequencies above $\sim$ 200 Hz, with standard deviations of 0.2 mG, 0.15 mG, 0.15 mG for x,y and z-axes respectively. Further improvement can be achieved by further modifying the time constant of the integrator (the current source which drives the compensation coils allows a bandwidth of up to 10 kHz). The implemented active feedback system has proven to be very effective, however, certain limits have to be considered.

Reproducibility of the sensor value

The major disadvantage of the magneto-resistive sensor material is that it requires a certain magnetic polarization for its function. Strong external magnetic fields can permanently change this magnetization which influences the output value and leads to a loss of sensitivity. Already a field of 6..8 G leads to a change of the zero-field value by 1..3 mG. Fields over 20..30 G permanently saturate the sensor disabling its function. In order to reverse this effect, three coil-straps are integrated into the sensor allowing to re-polarize the sensitive areas. For this purpose two current pulses of opposite directions (current $\sim$ 1 A, duration 10 μs) are sent through the straps. For two of the channels it was possible to achieve a reproducibility of the zero field value of few mG even after a complete magnetization of the sensor with a strong permanent magnet. For the third channel the value changed by several hundred mG depending on the orientation of the saturating field. However, the maximal field from the quadrupole coils of the MOT is below 10 G at the position of the sensor, therefore all three channels can be reset to original values with a residual error below 1 mG. If only small currents (below 1 A) are used for the quadrupole coils, as is done in a typical experiment, the field at the sensor is below 5 G and the reset procedure is in principle not necessary.

Gradients of the magnetic field

Another limitation of the achievable stability results from the fact that it is not possible to measure the field at the position of the trapped atom inside the vacuum cell. In our case the sensor is situated at $25\,\mathrm{mm}$ distance from the trap center. Therefore, even if the stability of the field at the position of the sensor itself is high, at the location of the dipole trap the situation can be different.

Gradients of external fields can be neglected, as all noise-producing devices are located at least $1\,\mathrm{m}$ away from the trap region. E.g., for a single wire at $1\,\mathrm{m}$ distance producing a field of $5\,\mathrm{mG}$ at the position of the trap, the gradient is $\frac{\partial B}{\partial r} = 5\,\mathrm{mG/m}$. For a distance of $25\,\mathrm{mm}$ between the atom and the sensor the resulting error (i.e. the difference between the value measured at the position of the sensor and the value at the position of the atom) is of the order of $0.1\,\mathrm{mG}$. Stronger gradients are produced by the permanent magnet of the ion-getter pump. In the vicinity of the glass cell the field strength is $300..1000\,\mathrm{mG}$ with gradients of the order of $2..5\,\mathrm{mG/mm}$. However, as long as the field of the magnet stays constant it does only affect the offset of the sensor setting.

The most important limitation results from the gradients of the compensating coils. Due to their compact dimensions (the size of a single coil and the distances between coils are all of the order $120..130\,\mathrm{mm}$), the displacement of the sensor with respect to the trap center leads to a deviation between the field measured by the sensor and the real field at the position of the trapped atom. Using the given geometry of the coils and the known displacement of the sensor ($16\,\mathrm{mm}$ along x-axis and $9\,\mathrm{mm}$ along y-axis) the deviation was calculated. For the x-axis it gives a deviation of 5% between the field at the sensor and the position of the trap and for the y-axis the deviation is 1%. Additionally, a field in z-direction occurs at the position of the sensor when applying a current to the coils which compensate the field along x-axis. The magnitude of this effect is 3.2%. Similar crosstalk of 3.5% exists from y- to the x-axis. Finally, for the z-axis a deviation of 4% occurs in the z-field between the sensor and the trap sites, there is no crosstalk to the other axes.

From these considerations the following conclusion can be drawn on the ultimate limit of the active stabilization system. As fluctuations of the order of $20\,\mathrm{mG}$ (peak-to-peak) have to be compensated on the x-axis, the stabilization will have a deviation of up to $1\,\mathrm{mG}$ on the x-axis and it will induce about $0.64\,\mathrm{mG}$ fluctuations on the z-axis due to the crosstalk. In principle such systematic errors can be reduced by increasing the size of the coils or incorporating the model of the coil gradients directly into the feedback circuit. For the time being the achieved stability is fully sufficient for our purposes.

4.6. Experimental results

4.6.1. Measurement of the state evolution

In order to measure the time evolution and to characterize the dephasing of the atomic state we use the procedure which is sketched in Fig. 4.11. First, the initial state is prepared by entangling the atom with the photon and measuring the photon in a selected basis (a). This measurement projects the atom onto one of two well-defined states $|\Psi_1\rangle$, $|\Psi_2\rangle$. Then the prepared states evolve for a certain time τ (b), and, finally, are analyzed using the regular state detection procedure (c).

In the initial experiments the control over the period of free evolution τ was done with the help of an analog electronic delay (variable RC). This delay allowed us to adjust τ in the range between $400\,\mathrm{ns}$ and $6\,\mu\mathrm{s}$ which was sufficient for the first measurements[18]. In order to increase the flexibility and range of accessible time periods a digital delay was developed which is synchronized with the pattern generator. The step size can range between $40\,\mathrm{ns}$ and $64\,\mathrm{ms}$. The delay is programmed over the parallel port and gives the possibility to count a given number of steps ($0..255$) allowing us to cover

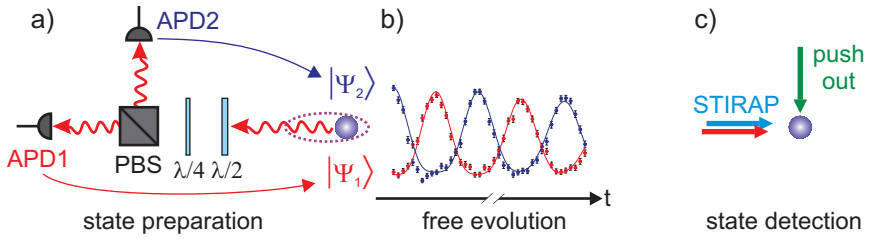

Figure 4.11.: Sequence for measuring the time evolution of the atomic state.

any relevant time scale with practically any necessary resolution.

Fig. 4.12(a) shows an example of such measurement. Here the states $|1,+1\rangle$ and $|1,-1\rangle$ are prepared and evolve in a field of about $150\,\mathrm{mG}$ applied along the x-axis. The atomic analysis procedure projects onto the state $|1,+1\rangle$. For the case without fluctuations of the field the analytic model in Eq. (4.10) predicts for the measured population $p_{|1,\pm1\rangle}(|1,+1\rangle)(t)$ the following behavior

$$p_{|1,+1\rangle}(|1,+1\rangle)(t) = \frac{1}{4}\left|(1+b_z^2)\cos(\omega_L t) + (1-b_z^2) - 2ib_z\sin(\omega_L t)\right|^2 \tag{4.24}$$
$$p_{|1,-1\rangle}(|1,+1\rangle)(t) = \frac{1}{4}\left(1-b_z^2\right)^2(1-\cos(\omega_L t))^2$$

The observed oscillation agrees very well with the theoretical model (see Eq. (4.11)) which additionally incorporates fluctuations of the field along the y-axis. The evolution of the superposition states $\frac{1}{\sqrt{2}}(|1,-1\rangle \pm |1,+1\rangle)$ is shown in Fig. 4.12(b). Here the magnetic field was compensated such that no oscillation could be observed. According to the model of Eq. (4.10) one would expect in case of no field fluctuations for the measured population $p_{\frac{1}{\sqrt{2}}(|1,-1\rangle\pm|1,+1\rangle)}(\frac{1}{\sqrt{2}}(|1,-1\rangle - |1,+1\rangle))(t)$

$$p_{\frac{1}{\sqrt{2}}(|1,-1\rangle-|1,+1\rangle)}(\frac{1}{\sqrt{2}}(|1,-1\rangle - |1,+1\rangle))(t) = \left(b_x^2 + (1-b_x^2)\cos(\omega_L t)\right)^2 \tag{4.25}$$
$$p_{\frac{1}{\sqrt{2}}(|1,-1\rangle+|1,+1\rangle)}(\frac{1}{\sqrt{2}}(|1,-1\rangle - |1,+1\rangle))(t) = (-b_x b_y(1-\cos(\omega_L t)) + b_z\sin(\omega_L t))^2$$

However, due to fluctuations of the magnetic field the states show a complete dephasing on a timescale of about $10\,\mu\mathrm{s}$. The model which incorporates fluctuations of the field along the x- and y-axes (external fields) as well as optically induced magnetic field of the dipole trap was fitted to the experimental data. It allows to estimate a volume of the circularly polarized admixture of the dipole trap light of about 5% and additionally $30\,\mathrm{mG}$ fluctuations orthogonal to the quantization axis at a residual average field strength of $B \leq 15\,\mathrm{mG}$. In contrast, the states $|1,\pm1\rangle$ in 4.12(a) remain stable for a longer time since they are not sensitive to fluctuations along the quantization axis and also due to the presence of a strong magnetic guiding field along x-axis which suppresses the influence of fluctuations orthogonal to it.

4.6.2. Improvements due to stability of magnetic field and trap polarization

After the introduction of the active magnetic field stabilization and better control of the polarization of the dipole trap light the coherence time could be significantly improved. In order to study the dephasing of superposition states $\frac{1}{\sqrt{2}}(|1,-1\rangle \pm |1,+1\rangle)$ we applied a weak field of about $5.5\,\mathrm{mG}$ along the quantization axis which allows to observe the envelope of the Larmor precession as shown in Fig.

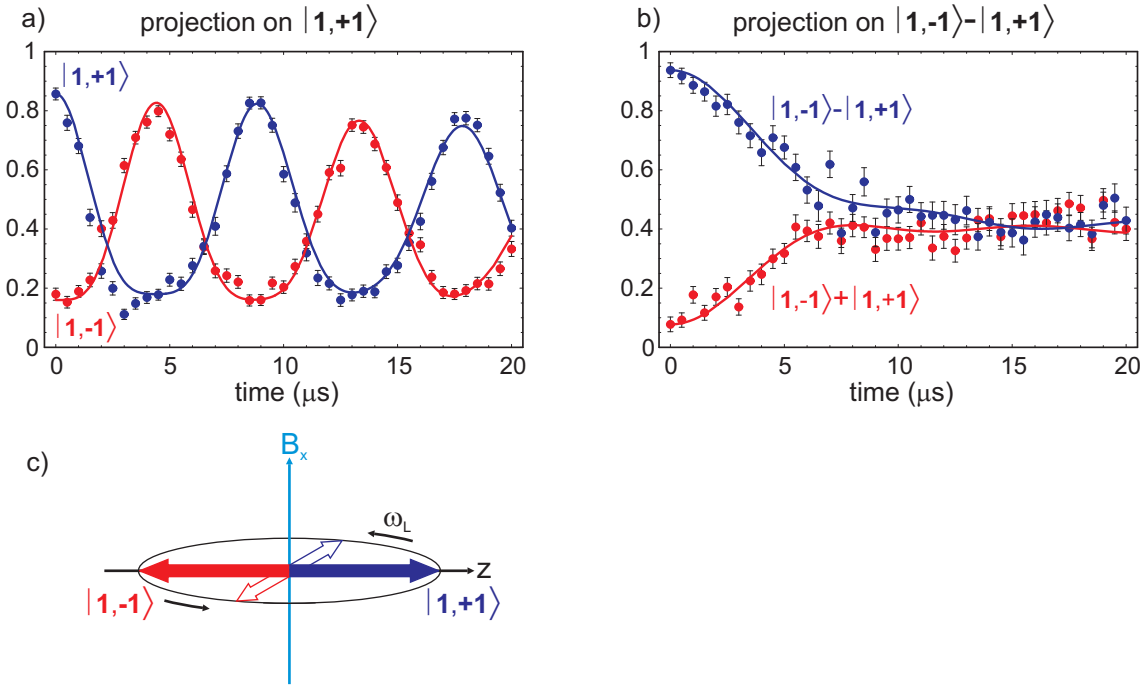

Figure 4.12.: Measurement of the time evolution of the atomic state (without active stabilization of the magnetic field and control of the dipole trap polarization). a) Evolution of the states $|1,+1\rangle$ and $|1,-1\rangle$ in a field $B_x \sim 150\,\mathrm{mG}$, projected onto the state $|1,+1\rangle$ after a given delay. The solid lines show the fit of the model based on Eq. (4.10). b) Evolution of $\frac{1}{\sqrt{2}}(|1,-1\rangle \pm |1,+1\rangle)$ states in a weak residual field $B \leq 15\,\mathrm{mG}$. c) Classical picture of a precessing magnetic dipole.

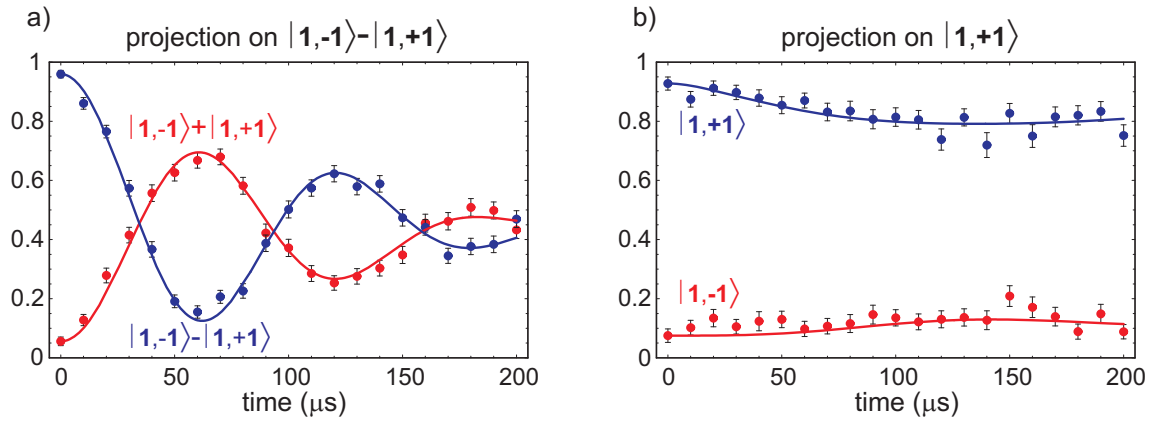

Figure 4.13.: Time evolution of atomic states with stabilized magnetic field and controlled polarization of the dipole trap. a) Evolution of the states $\frac{1}{\sqrt{2}}(|1,-1\rangle \pm |1,+1\rangle)$, the offset field along quantization axis is $5.5\,\mathrm{mG}$ corresponding to $\omega_L = 2\pi \cdot 3.85\,\mathrm{kHz}$. b) Evolution of the states $|1,\pm1\rangle$ in a field compensated to $B \lesssim 2\,\mathrm{mG}$.

4.13(a). The corresponding $\frac{1}{e}$ dephasing time is now on the order of $150\,\mu\mathrm{s}$. Under the assumption that the residual dephasing is mainly caused by the effective magnetic field induced by the dipole trap we can infer the fraction of the circularly polarized light $F_\sigma = 0.6\%$ (assuming an average atomic temperature $T = 0.15\,\mathrm{mK}$ the standard deviation of the distribution is then $2.25\,\mathrm{mG}$). The assumption that the circular admixture is now the main reason for dephasing is strongly supported by the measurement in Fig. 4.13(b). Here the states $|1,\pm1\rangle$, which are only sensitive to the field orthogonal to the quantization axis z, show significantly longer dephasing time, proving that the residual fluctuations are mainly along this axis. Since the magnetic field stabilization achieves nearly the same stability for all axes, the remaining effect can only be explained by the optically induced effective magnetic field.

4.6.3. Effect from polarization of the dipole trap light

Since, after the stabilization of the magnetic field, the effect of the dipole trap polarization is the limiting factor for the dephasing time, it has to be studied in more detail. Therefore, the evolution of $\frac{1}{\sqrt{2}}(|1,-1\rangle \pm |1,+1\rangle)$ states was compared for different linear polarization angles of the dipole trap beam (Fig. 4.14). The offset field along the quantization axis was adjusted such that no precession could be observed within $200\,\mu\mathrm{s}$. The difference in angle of the linear polarization was $1°$. It was found that an offset field difference of about $25\,\mathrm{mG}$ was necessary to compensate the change in Larmor frequency due to the different polarization. From this we can estimate the change in the circular light fraction of about 1.5% (in Fig. 4.14(b) F_σ is slightly higher, additionally the polarization changes from σ^- to σ^+). Assuming the circular dipole trap polarization being the only effect leading to dephasing, F_σ can also be estimated. The observed evolution in Fig. 4.14(a) is compatible with a fraction of circular light of $F_\sigma = 0.6\%..0.8\%$. The dephasing time in this measurement is still under-estimated due to residual Larmor precession.

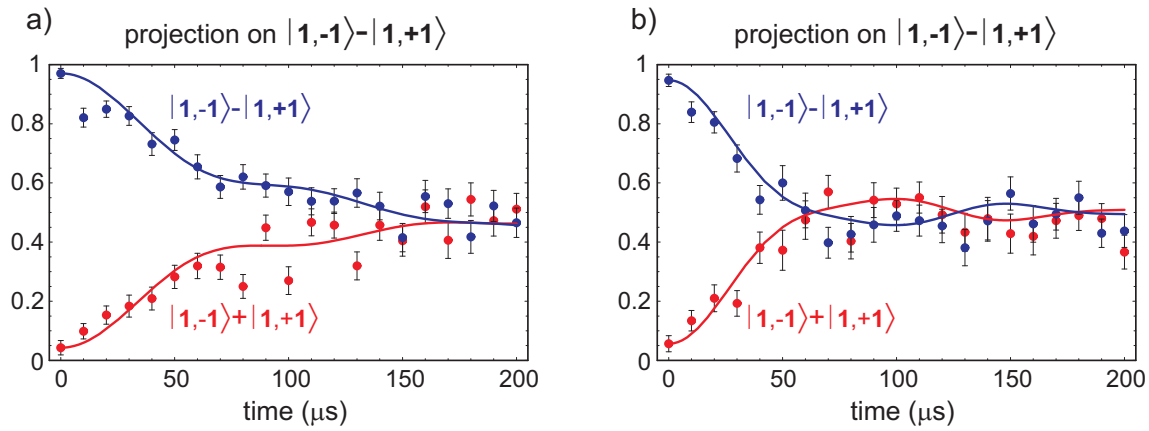

Figure 4.14.: Evolution of $\frac{1}{\sqrt{2}}(|1,-1\rangle \pm |1,+1\rangle)$ states for two linear polarizations of the dipole trap light differing (outside the glass cell) by 1°. The additionally applied offset field of $25\,\mathrm{mG}$ along the quantization axis nearly compensates the change of the mean effective field.

4.6.4. Effect of the guiding field

As was studied in Sec. 4.4.3, the application of a magnetic guiding field has a stabilizing effect upon certain atomic states (the eigenstates of the field Hamiltonian). In order to verify this in an experiment a weak guiding field of $25\,\mathrm{mG}$ was applied along the x-direction. In this case the state $\frac{1}{\sqrt{2}}(|1,-1\rangle - |1,+1\rangle) = |1,0\rangle_x$ is an eigenstate of the magnetic field and therefore is stabilized. At the same time the state $\frac{1}{\sqrt{2}}(|1,-1\rangle + |1,+1\rangle) = |1,0\rangle_y$, which is not an eigenstate, undergoes Larmor precession into $|1,0\rangle$ and back. This precession is not visible in the projection onto the $\frac{1}{\sqrt{2}}(|1,-1\rangle - |1,+1\rangle)$ state. As shown in Fig. 4.15 the eigenstate of the field remains unchanged over several milliseconds. However, the other prepared state will dephase on a much shorter time-scale. The reason is that the frequency of the Larmor precession between the $\frac{1}{\sqrt{2}}(|1,-1\rangle + |1,+1\rangle)$ and the $|1,0\rangle$ is subject to fluctuations of the magnetic field along the x-axis and thus dephases after about $75..150\,\mu\mathrm{s}$.

4.7. Partial tomography of the state evolution

The best way to determine the coherence properties of the state under study is to perform quantum state tomography. In the case of a spin-1 ground level the time evolution involves three states, thus the analysis becomes more difficult compared to a qubit state. In particular, the coherences between the $|1,\pm1\rangle$ Zeeman states and the $|1,0\rangle$ state can not be measured adequately with the present detection procedure. Still, the state tomography of the $\{|1,-1\rangle, |1,+1\rangle\}$-subspace allows to estimate missing elements of the spin-1 density matrix. See App. B for more details.

A tomographic measurement was performed for the time evolution of the states $\frac{1}{\sqrt{2}}(|1,-1\rangle \pm |1,+1\rangle)$ and $|1,\pm1\rangle$. The magnetic field was set such that practically no precession could be observed, while the circular fraction of the dipole trap polarization being $F_\sigma \lesssim 1\%$. For each delay time ($0..200\,\mu\mathrm{s}$ in steps of $50\,\mu\mathrm{s}$) the populations of eigenstates of $\hat{\sigma}_x$, $\hat{\sigma}_y$, $\hat{\sigma}_z$ operators were measured. From these measurements the sub-matrix $\hat{\rho}_s$ of the $\{|1,-1\rangle, |1,+1\rangle\}$ system was reconstructed according to Eq.

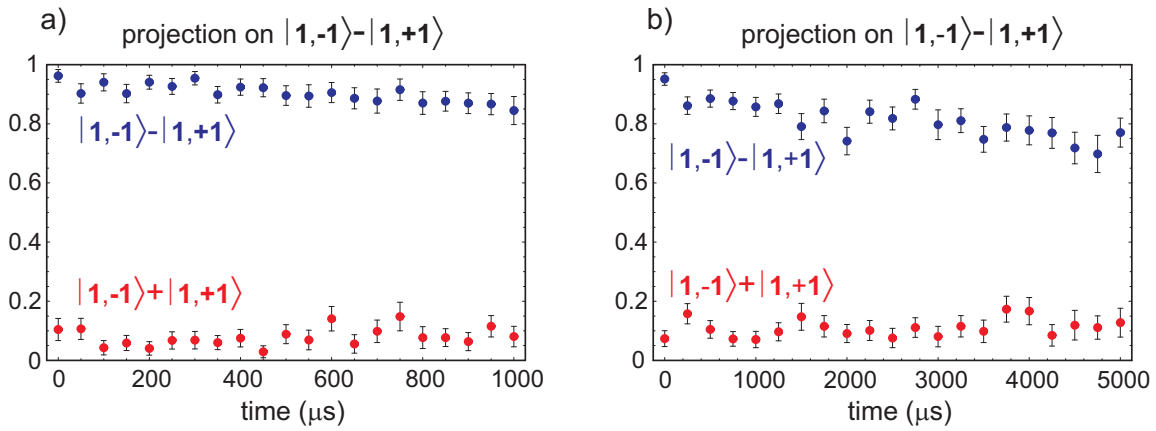

Figure 4.15.: Evolution of $\frac{1}{\sqrt{2}}(|1,-1\rangle \pm |1,+1\rangle)$ states in a guiding field along x-direction. Note that the precession between the $\frac{1}{\sqrt{2}}(|1,-1\rangle + |1,+1\rangle)$ and $|1,0\rangle$ states is not visible in the projection onto the $\frac{1}{\sqrt{2}}(|1,-1\rangle - |1,+1\rangle)$ state.

(B.6) and the remaining diagonal element is given by $\rho_{00} = 1 - trace(\hat{\rho}_s)$.

For the worst case estimation of the state coherence we assume that the population transfer into the $|1,0\rangle$ state takes place in a completely incoherent way. In this case the coherences to the $|1,0\rangle$ state are all equal to zero and the full 3×3 density matrix reads, according to Eq. (B.5)

$$\hat{\rho} = \begin{pmatrix} & & 0 \\ & \hat{\rho}_s & 0 \\ 0 & 0 & \rho_{00} \end{pmatrix} \tag{4.26}$$

The real part of the matrices obtained in this way is shown in Fig. 4.16. In the time evolution of the measured density matrices for the $\frac{1}{\sqrt{2}}(|1,-1\rangle \pm |1,+1\rangle)$ states one can observe several important features. The first one is the decay of the off-diagonal elements (coherences) as a general sign of dephasing. Second, a residual Larmor precession is visible as the change of the sign of the coherences which become imaginary at a certain point of the evolution (between 100 and 150 μs). Furthermore the population of the $|1,0\rangle$ state increases slowly getting as large as $\sim 15\%$ after 200 μs. In contrast, for the $|1,\pm1\rangle$ states the main process is a slow drift into the $|1,0\rangle$ state.

In order to estimate the coherence of the measured quantum state we calculate the purity parameter r according to Eq. (B.11)

$$r = \sqrt{\frac{1}{2}(3 \cdot trace(\hat{\rho}^2) - 1)} \tag{4.27}$$

The number r gives the lower bound for the coherent fraction of the partially mixed state after the time evolution (see App. B). For the evolution of the superposition states $\frac{1}{\sqrt{2}}(|1,-1\rangle \pm |1,+1\rangle)$, see Fig. 4.17(a), we determine the $\frac{1}{e}$ dephasing time of 150 μs in absence of a guiding field.

One has to keep in mind that this result was determined in the 3-level system for dephasing towards the completely mixed state $\frac{1}{3}\hat{\mathbb{1}}$. This process is given by two mechanisms. The first one is the dephasing of superpositions caused by fluctuations of the optically induced magnetic field resulting from circular admixture in polarization of the dipole trap light of the order of $F_\sigma = 0.6\% - 1\%$. It leads to decay of the off-diagonal components in the $\{|1,-1\rangle, |1,+1\rangle\}$-subspace which happens for

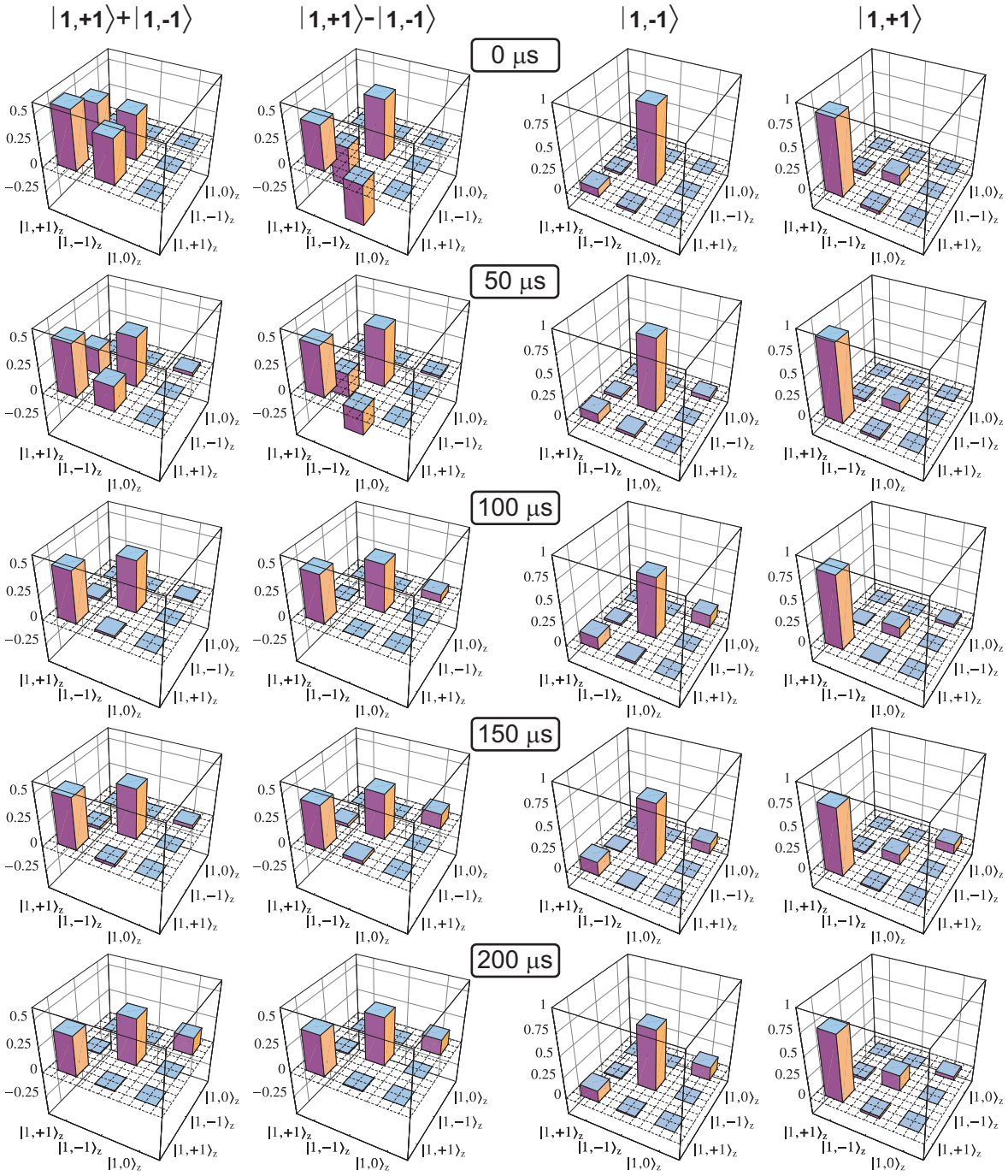

Figure 4.16.: Time evolution of the atomic density matrix as the atom is prepared initially in the states $\frac{1}{\sqrt{2}}(|1,-1\rangle \pm |1,+1\rangle)$ and $|1,\pm1\rangle$, respectively. The matrices (depicted is the real part) are reconstructed according to Eq. (4.26) under assumption of no coherence between $\{|1,-1\rangle, |1,+1\rangle\}$ and $|1,0\rangle$ states.

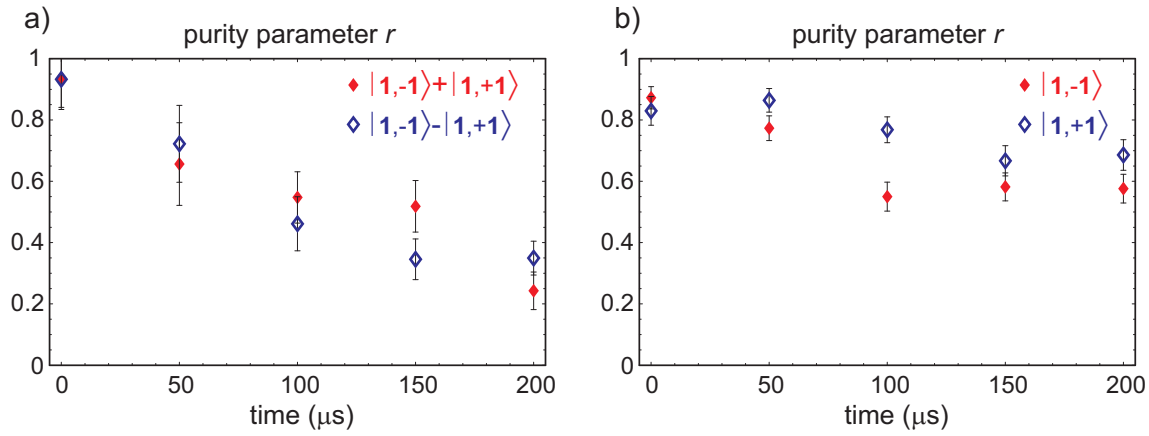

Figure 4.17.: Time evolution of the purity parameter r from tomographic measurements shown in Fig. 4.16. a) Initially prepared states are $\frac{1}{\sqrt{2}}(|1,-1\rangle \pm |1,+1\rangle)$. b) Initially prepared states are $|1,\pm1\rangle$.

this measurement on the timescale of

$$T_2^* = 75\,\mu\mathrm{s}.$$

This number is lower than the one which can be obtained from the envelope in Fig. 4.13(a) due to a larger admixture of circularly polarized trapping light. The second mechanism is the drift into the $|1,0\rangle$ state which is significantly slower and has no analogy in two-level systems.

For the $|1,\pm1\rangle$ states, see Fig. 4.17(b), we estimate the longitudinal dephasing time in absence of a guiding field by extrapolation

$$T_1 \gtrsim 500\,\mu\mathrm{s}$$

giving the timescale on which the qubit states approach an equal mixture of all three spin-1 states. This is a lower bound estimation as with the current detection procedure it is impossible to distinguish between coherent rotation into the $|1,0\rangle$ state and incoherent dephasing. In any case, the significantly higher longitudinal dephasing time shows that the fluctuations of the field are mainly along the quantization axis, caused predominantly by circular polarization admixture in the trapping light.

4.8. Summary

In this chapter the coherence properties of a qubit stored in Zeeman hyperfine states of the $F = 1$ level in ^{87}Rb were studied. The higher dimensionality (spin-1) of the system which incorporates the qubit leads to complex dynamics, in particular the quantum state can leave the qubit subspace during coherent evolution in a magnetic field. The main factors, which influence the coherence of the quantum state, were identified as fluctuations of the external magnetic field and the effective magnetic field caused by circular components of the dipole trap light. A model was developed which allows to describe the dephasing of the quantum state caused by these effects. In order to compensate the magnetic field fluctuations a system for active stabilization was developed and installed reducing the fluctuations below $1\,\mathrm{mG}$ for each axis. Furthermore the circular component of the dipole trap light was identified as additional source of decoherence and thus reduced below 1%. These improvements increased the dephasing time by over an order of magnitude. For superposition states of the form

$\frac{1}{\sqrt{2}}\left(|1,-1\rangle + e^{i\phi}\,|1,+1\rangle\right)$ the transversal dephasing time has increased from $T_2^* = 5..10\,\mu\mathrm{s}$ to $T_2^* = 75..150\,\mu\mathrm{s}$ which was verified by means of a partial quantum state tomography. The longitudinal coherence time of the states $|1,\pm1\rangle$ was estimated as $T_1 \gtrsim 500\,\mu\mathrm{s}$ (lower bound). Both results were measured in absence of an offset magnetic field. In a small guiding field ($\sim 25\,\mathrm{mG}$) we observed a high stability of eigenstates for several milliseconds.

As a possible extension in future experiments, one might apply an intermediate guiding field along the quantization axis, such that precession into the $|1,0\rangle$ can be neglected. In this case the system reduces to two states and the spin-echo technique could be applied to further increase the dephasing time.

5. Distribution of Entanglement over Long Distance

5.1. Introduction

In the experiments which were presented so far, atom-photon entanglement was used mainly as an interface to characterize and locally manipulate atomic states. The next step is to distribute the entanglement on a larger scale. This can be used, e.g., to create entanglement between separate atomic systems. First steps in this direction were done by different groups by entangling two atomic ensembles [78] and two trapped ions [79, 80] at a distance of few meters. In the first one, the photon was sent from one atomic ensemble to the other one where it was absorbed using EIT. In the later, two simultaneously emitted photons were sent to an intermediate location where entanglement swapping was performed.

Our goal is to establish atom-atom entanglement over several hundred meters, this requires a stable and reliable optical link. The communication of the photon over a large distance can be done either via a free-space link or using optical fibers. Free-space experiments have achieved impressive distances of up to $144\,\mathrm{km}$ demonstrating distribution of entangled photons and quantum cryptography [81, 82]. Practical urban free-space communication between rooftops was demonstrated as well [83]. However, this method requires a direct line of sight between sending and receiving units, is affected by weather conditions and has an increased background during daytime due to stray light.

An alternative is the fiber-based optical communication. It is more practical in the sense that a fiber can follow in principle any path and can be used at any time. Quantum informational experiments were performed over fibers demonstrating e.g. quantum key distribution [84] and distribution of polarization entanglement [85] over distances of $67\,\mathrm{km}$ and $100\,\mathrm{km}$ respectively. However, fibers have also disadvantages like non-negligible absorption, dispersion and birefringence. For the wavelength used in our experiment ($780\,\mathrm{nm}$) the absorption of a typical single-mode fiber is of the order of $6\,\mathrm{dB/km}$ easily allowing to bridge several hundred meters. Due to the very small bandwidth of the photons in our experiment ($6\,\mathrm{MHz}$) the dispersion can be neglected. However, the stress-induced birefringence represents a serious problem for transmission of polarization-encoded qubits as it changes the qubit state in an uncontrolled way.

In this chapter a system is presented which allows to compensate the effect of birefringence in fibers. A stable optical fiber link of $300\,\mathrm{m}$ is established and characterized. Large parts of this work were done by and together with Fredrik Hocke and are described in full detail in his diploma thesis [86]. As an ultimate test we have verified atom-photon entanglement over the $300\,\mathrm{m}$ fiber.

5.2. Measurement of polarization drifts in optical fibers

Optical fibers are a very practical tool for guiding light to a remote location with small losses and are widely used for optical telecommunication. For laboratory experiments, an additional advantage is the filtering of the spatial mode of light in single-mode fibers. However, a serious problem is

the preservation of the light polarization during propagation. Any bending of a fiber leads to local birefringence, which is induced by mechanical stress (see e.g. [87]). This leads to a change of the polarization state, depending on the mechanical stress, the temperature and the wavelength of the light. For experiments using the polarization degree of freedom of photons this effect must be avoided.

The use of so-called "polarization-maintaining" (PM) fibers does not solve the problem. These fibers are manufactured with already "built-in" mechanical stress, defining two orthogonal polarization eigen-axes. Linear polarization, which is coupled into one of the eigen-axes will adiabatically follow the bending of the fiber and stay in the same eigen-axis whose orientation is well defined with respect to the output coupler. Therefore, these fibers are capable of maintaining two orthogonal linear polarizations, which have to be coupled exactly into the two polarization eigen-modes. For encoding a qubit into the polarization of the light this is not sufficient, since the relative phase between these two polarization states is important as well. This phase is however strongly influenced because PM-fibers use birefringence to define the two eigen-axes.

The polarization rotation induced by the fiber is a unitary operation, which does not affect other parameters of the propagating light-pulse[1]. Therefore, if the effect of the fiber is known, it can be compensated by applying the inverse operation with wave-plates or a fiber polarization controller. In previous experiments the birefringence of the optical fiber guiding the photon from the collection objective to the detectors ($5\,\mathrm{m}$) was compensated manually. Proper fixing of the fiber to the optical table together with a constant temperature in the laboratory ensure stability for several weeks to months. For a long fiber in a cable channel the compensation procedure has to be performed more often. To counteract temperature- and mechanical drifts it can be necessary to adjust the compensation in periods of several minutes to hours. This requires a fast, reliable and automatic compensation procedure.

5.2.1. Reference polarimeter

The first step in compensation of an unknown polarization rotation is to measure it. This can be done by coupling in reference light of known polarization and measuring the polarization at the output. For a complete characterization of the fiber rotation this procedure has to be performed with two non-orthogonal input polarizations. For this purpose reference light of few μW power is used which can be switched between two polarizations (V and $+45°$) with help of mechanical shutters. The reference light is sent through the vacuum glass cell from where it follows the same path as the emitted photons passing the fiber which guides it to the detectors (see Fig. 5.1).

On the detector side a reference polarimeter was set up. It consists of three pairs of detectors simultaneously analyzing the polarization in three conjugate bases $\hat{\sigma}_x$ (H/V), $\hat{\sigma}_y$ ($\pm 45°$) and $\hat{\sigma}_z$ (R/L) which are defined by half- and quarter-wave plates and polarizing beam splitters (PBS). The six currents I of the photo-diodes are amplified, digitized and read into a computer which calculates the Stokes parameters as

$$\begin{aligned} S_1 &= \frac{I_H - I_V}{I_H + I_V} \\ S_2 &= \frac{I_{+45°} - I_{-45°}}{I_{+45°} + I_{-45°}} \\ S_3 &= \frac{I_R - I_L}{I_R + I_L} \end{aligned} \tag{5.1}$$

[1] The so-called "polarization-mode dispersion" (PMD), where one polarization component can overtake the other one due to birefringence (typically of the order of $1\,\mathrm{ps}/\sqrt{\mathrm{km}}$), is not relevant for our pulse durations ($\sim 26\,\mathrm{ns}$) and propagation lengths (few $100\,\mathrm{m}$).

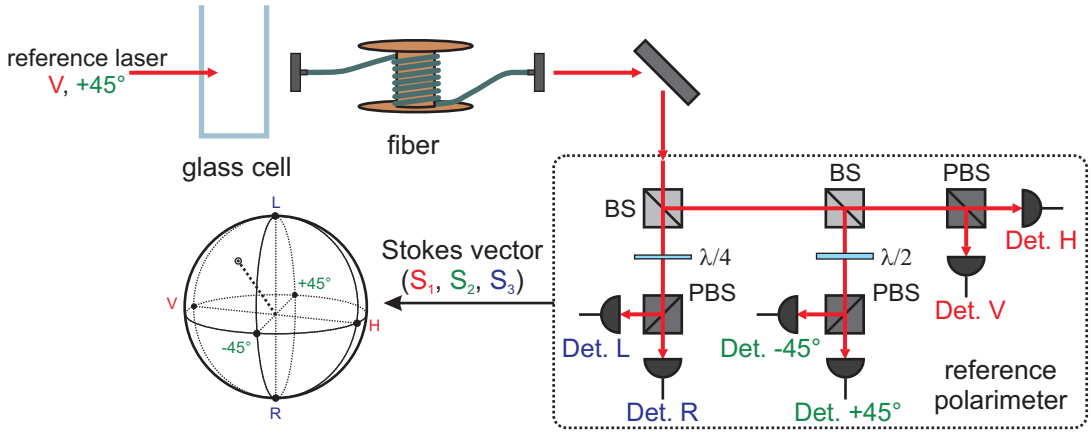

Figure 5.1.: Measurement of birefringence in the fiber. Reference light is coupled through the glass cell into the photon detection fiber and analyzed in a reference polarimeter. From six signals of the photodiodes the Stokes vector of the output polarization is determined.

The Stokes vector $\vec{S} = (S_1, S_2, S_3)$ completely describes the polarization state (including mixed states) and can be visualized on the Poincare-sphere the same way as a two-level system is represented on the Bloch-sphere. The whole procedure of sending two polarizations through the fiber, analyzing the output and determining the Stokes vector takes about $0.67\,\mathrm{s}$, mainly limited by the speed of mechanical shutters.

The precision of the reference polarimeter together with the purity of input reference polarizations are crucial parameters for the reliability of the compensation procedure. Therefore both systems were carefully calibrated with respect to a reference polarizing filter (extinction $> 1\colon 5000$). In order to achieve faithful polarization measurement, several issues had to be considered. Systematic errors like imperfect extinction of the polarizing beam splitters and different efficiencies of the photo-diodes were measured and eliminated in the calculation of the Stokes parameters. Furthermore, additional phases between H and V polarization occur after reflection on beam splitters or mirrors which have to be compensated using additional birefringent plates. Moreover, the non-polarizing beam splitters show residual polarization dependence leading to a change of polarization in the output ports. This error was minimized by selecting beam splitters with the best parameters out of a set, allowing measurement fidelities of at least 0.999. Finally, errors in the alignment of the waveplates which define the measurement bases were characterized showing an error of the order of $\sim 1^\circ$ on the Poincare sphere.

The performance of the reference polarimeter was determined by sending light with defined polarizations directly into its input. For V and $+45^\circ$ input polarizations the overlap[2] of the measured Stokes vectors $\vec{S}_V$, $\vec{S}_{+45^\circ}$ with expected $\vec{S}_{V\,(ideal)} = (-1, 0, 0)$, $\vec{S}_{+45^\circ\,(ideal)} = (0, 1, 0)$ was

$$\begin{aligned} \left\langle \vec{S}_{V\,(ideal)}, \vec{S}_V \right\rangle &= 0.9996 \\ \left\langle \vec{S}_{+45^\circ\,(ideal)}, \vec{S}_{+45^\circ} \right\rangle &= 0.9985 \end{aligned} \tag{5.2}$$

respectively. This proves the high fidelity of the polarization analysis.

[2]The overlap of two Stokes vectors $\vec{S}_A$, $\vec{S}_B$ is defined as $\left\langle \vec{S}_A, \vec{S}_B \right\rangle := \cos^2\left(\frac{1}{2}\arccos\left(\frac{\vec{S}_A \cdot \vec{S}_B}{|\vec{S}_A||\vec{S}_B|}\right)\right)$, where $\vec{S}_A \cdot \vec{S}_B = \sum_{j=1}^{3} S_{Aj} S_{Bj}$ is the scalar product. This definition takes into account the fact that the angles on the Poincare-sphere are twice as large compared to the real space, e.g., vectors of orthogonal states enclose an angle of π.

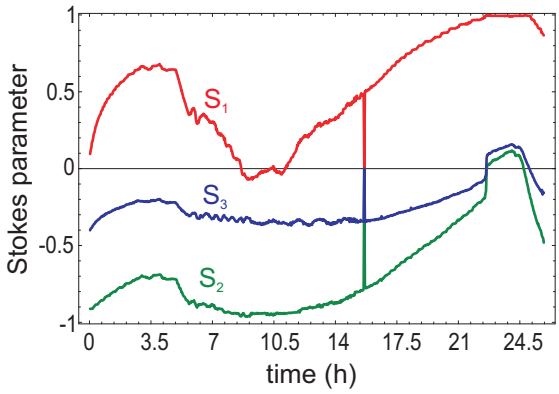

Figure 5.2.: Polarization drift in a 300 meter long single-mode optical fiber. The fiber is on a spool in a laboratory room without air conditioning. Shown are the Stokes parameters of the output polarization for fixed input polarization.

Measurement of polarization drift in 300 m fiber

After proving the reliability of the reference polarimeter the next step was to measure the polarization drift in a long fiber. Therefore a 300 meter long single-mode fiber (Nufern 630HP) was used which was left completely on its spool and placed directly on the optical table. No special measures were taken for mechanical stability of the fiber, additionally the air conditioning was deactivated, resulting in temperature drifts of about $5°\mathrm{C}$. The measurement of the output state for constant input polarization was performed continuously for $24\,\mathrm{h}$. The result is shown in Fig. 5.2. We observe drifts of polarization of the order of typically $8°..10°$ per hour on the Poincare-sphere on average. Faster drifts were mainly caused by temperature changes, people working in the lab, opening/closing of the doors, etc.

This measurement is not completely representative for the realistic situation where the fibers will be installed in underground cable channels. In particular the fiber is on the spool which results in a relatively strong and directed bending. For the future installation the fiber shall be enclosed into a stiff jacket which will avoid strong bending and increase the stability. Still, this measurement shows that the compensation of fiber birefringence should be repeated in intervals of the order of 10 minutes in order to minimize the polarization errors during the experiment.

5.3. Active stabilization of fiber birefringence

In order to perform an automatic procedure for compensation of the fiber birefringence, one needs the ability to measure it (already implemented), a device which will control it, and a method to determine the necessary parameters for the controller. The two later parts will be described in this section.

5.3.1. Polarization controller

For the control of the polarization we use a fiber-integrated device (General Photonics Polarite III). It consists of 4 piezo elements squeezing the fiber from different angles. The squeezing induces birefringence which is used for control of the polarization[3]. The device is shipped together with a

[3] In principle 3 channels would be sufficient to perform any unitary operation. The use of four channels simplifies the so-called “endless” (reset-free) polarization control (see e.g. [88]).

driver card. It has 4 input channels ranging $0 - 5\,\mathrm{V}$ which are internally amplified by a factor of 30. The inputs are controlled by a DA-card of a computer with a voltage range between $-10\,\mathrm{V}$ and $+10\,\mathrm{V}$ and a resolution of $2.5\,\mathrm{mV}$. For a single squeezer to perform a complete rotation on the Poincare-sphere, a voltage difference of about $1\,\mathrm{V}$ is needed on the input. The bandwidth of the polarization controller is $20\,\mathrm{kHz}$. The long term stability of the device was also studied, no drifts could be observed within a time period of 1 hour.

The polarization controller is able to map any input polarization onto an arbitrary output polarization. However, it is not trivial to deterministically set the necessary input parameters in order to achieve the desired effect. Therefore an iterative procedure which finds the optimal parameters was developed, as described in the following.

5.3.2. Parameter optimization algorithm

Given the effect of the fiber on two input reference polarizations, the task of the algorithm is to find an optimal set of parameters for the polarization controller. The optimal setting is the one where the two non-orthogonal input reference polarizations (here V and $+45°$) are preserved. Our method of choice is the so-called "gradient descent" which iteratively minimizes an appropriately defined measure for the polarization error.

As a measure of deviation between the measured Stokes vectors $\vec{S}_V$, $\vec{S}_{+45°}$ after the fiber and the setting values $\vec{S}_{V\,(set)}$, $\vec{S}_{+45°\,(set)}$ we define the error function as

$$f := \left|\vec{S}_V(\vec{U}) - \vec{S}_{V\,(set)}\right|^2 + \left|\vec{S}_{+45°}(\vec{U}) - \vec{S}_{+45°\,(set)}\right|^2 \tag{5.3}$$

which is basically the square sum of (Euclidean) distances between the measured polarizations and the desired ones. For the given set-points $\vec{S}_{V\,(set)}$, $\vec{S}_{+45°\,(set)}$ the error f is a function of 4 control voltages $\vec{U} = (U_1, U_2, U_3, U_4)$ with a global minimum equal to 0. Since 3 parameters are already sufficient to achieve any desired output polarization (and also each channel can perform several complete rotations on the Poincare-sphere within its input range), the optimal parameter set $\vec{U}_{opt}$ is not unique. This ambiguity, however, does not increase the complexity of the problem as the algorithm searches for the nearest optimal parameter set.

Next, the gradient of the error function with respect to the control voltages is determined. Each component (partial derivative) is measured by adding a small voltage ΔU on the corresponding channel and measuring the change of the error function

$$(\nabla f)_j(\vec{U}) = \frac{\partial f}{\partial U_j} \approx \frac{f(\vec{U} + (0, .., \Delta U_j, ..0)) - f(\vec{U})}{\Delta U_j} \tag{5.4}$$

The gradient vector gives the direction of maximal increase of the error function in the 4-dimensional parameter space. Therefore, the error function can be minimized best by adjusting the parameters in direction opposite to the gradient vector:

$$\vec{U}_{new} = \vec{U}_{old} - D \cdot \nabla f \tag{5.5}$$

where D is a scaling factor which defines the step size. Its value can be adjusted such, that depending on situation, quick convergence of the algorithm is ensured (for more details see [86]). Each step leads to a decrease of the error function for the two reference polarizations and finally converges to the global minimum. This procedure is repeated until the error function f gets smaller than a defined

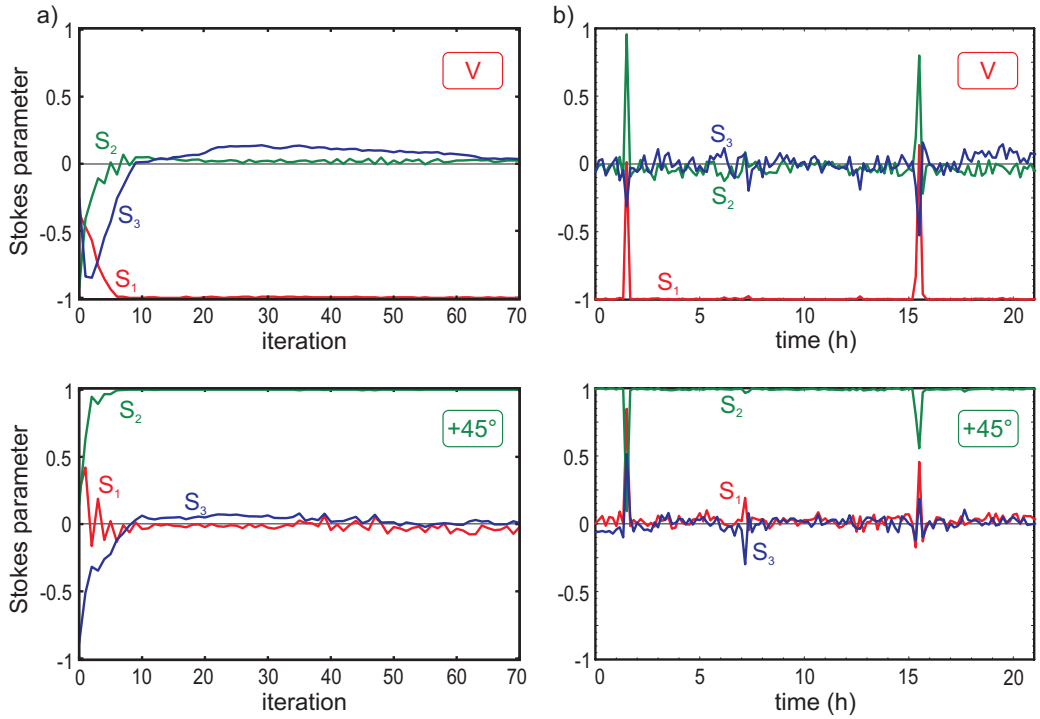

Figure 5.3.: Fiber birefringence compensation. Shown are the Stokes parameters of the polarization on the output of the $300\,\mathrm{m}$ fiber for input reference polarizations V and $+45°$. a) Initial convergence of the iterative optimization algorithm (one iteration takes $0.67\,\mathrm{s}$). b) Long-time behavior (same time between iterations). For explanation of the few outlying points see text.

threshold value of $f_{thr} = 0.008$. The algorithm terminates after the error function stays below the threshold for 5 iterations.

The advantage of this method is that it is relatively easy to implement, does not require large computational resources and its convergence is assured even in presence of small errors.

5.3.3. Performance

We have tested the automatic birefringence compensation procedure with the $300\,\mathrm{m}$ fiber. The algorithm was applied continuously and the output Stokes vectors for two reference polarizations were recorded. Fig. 5.3(a) shows the initial convergence of the algorithm after it has started at a random setting of the polarization controller. Within $10..20$ iterations the value of the error function is reduced below 0.02. After that the system gets stable within this region, with a mean value of $\bar{f} \leq 0.006$. This stability can be maintained for long periods of time, Fig. 5.3(b). The sometimes occurring errors in the measurement (visible as spikes) are due to eventual high CPU load of the controlling computer which leads to an asynchronicity in opening of the shutters during one iteration. These events have no influence on the final error as the system quickly converges again.

Several limits of the achievable performance have to be mentioned. First, the purity of the input reference polarizations is very critical. If the angle between two polarization states on the Poincare sphere is not $\frac{\pi}{2}$, the error function can not be reduced beyond a certain value. If this value is larger than

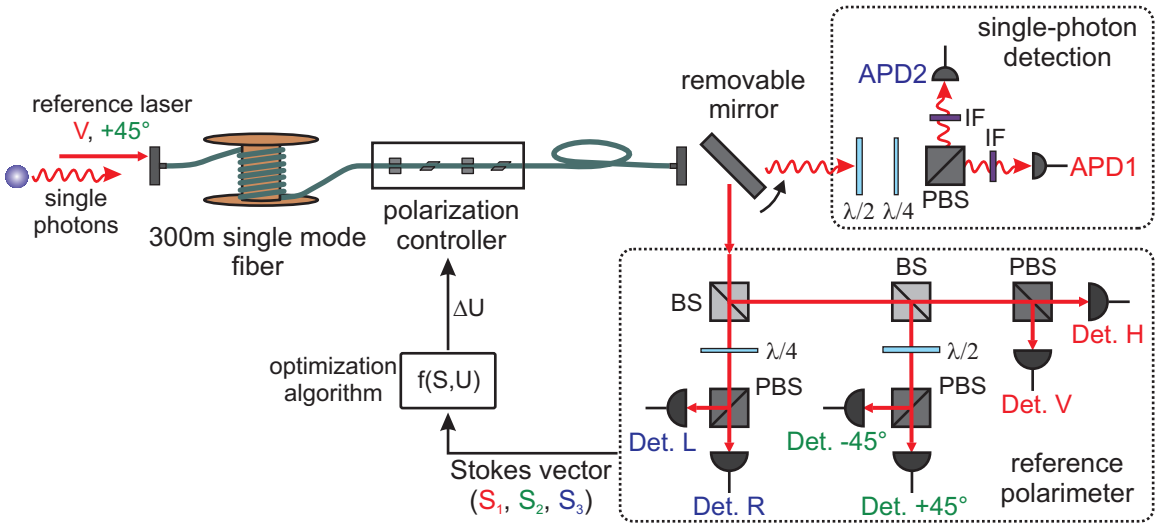

Figure 5.4.: Distribution of atom-photon entanglement over a long fiber.

the threshold f_{thr}, the algorithm will not terminate. This problem is avoided by carefully adjusting the reference polarizations. Second, the minimal rotation which the polarization controller can perform is given by the resolution of the analog output card. In the current setup the resolution is $2.5\,\mathrm{mV}$ giving a minimal angle on the Poincare sphere of $0.9°..1.2°$ (the response of different channels differs by up to 25%). Because of this discreteness it is not possible to reach the optimal point exactly. Additionally it introduces errors in the measurement of the gradient of the error function in Eq. (5.4) which relies on the small size of ΔU. In the future the output range of the analog card will be matched to the polarization controller input, thereby increasing the resolution.

In conclusion the automatic compensation system has proven to be reliable. Starting at a random position it typically converges within 22 iterations to a value where the overlap between the measured Stokes vectors on the output and the set values is $\left\langle \vec{S}_V, \vec{S}_{V\,(set)} \right\rangle, \left\langle \vec{S}_{+45°}, \vec{S}_{+45°\,(set)} \right\rangle \geq 0.998$. For compensation of small drifts after $15\,\mathrm{min}$ it needs typically less than 10 iterations to achieve the above value again. Additionally we have tested the influence of the wavelength of reference light onto the measured result. Within the achievable detuning range of several GHz of the reference laser no change in the measured polarization could be observed. This assures that no additional errors are introduced by the small frequency difference of the single photons with respect to the reference light ($51\,\mathrm{MHz}$).

5.4. Atom-photon entanglement over 300 meter fiber

Using the presented system for compensation of fiber birefringence we have measured the entanglement between the atom and the photon after sending the photon over $300\,\mathrm{m}$ fiber. The schematic of this experiment is shown in Fig. 5.4. Single photons emitted by the atom are first coupled by the microscope into the $5\,\mathrm{m}$ detection fiber which is followed by the $300\,\mathrm{m}$ fiber. Then they pass the polarization controller and are finally detected by single photon counting APDs. The overall transmission for the photon on the way to the detectors is about 45%. It is composed of coupling from the microscope fiber into $300\,\mathrm{m}$ fiber ($\sim 90\%$), transmission of the long fiber ($\sim 70\%$ for $780\,\mathrm{nm}$) and coupling into the optical fiber of the polarization controller which has a different core diameter ($\sim 80\%$).

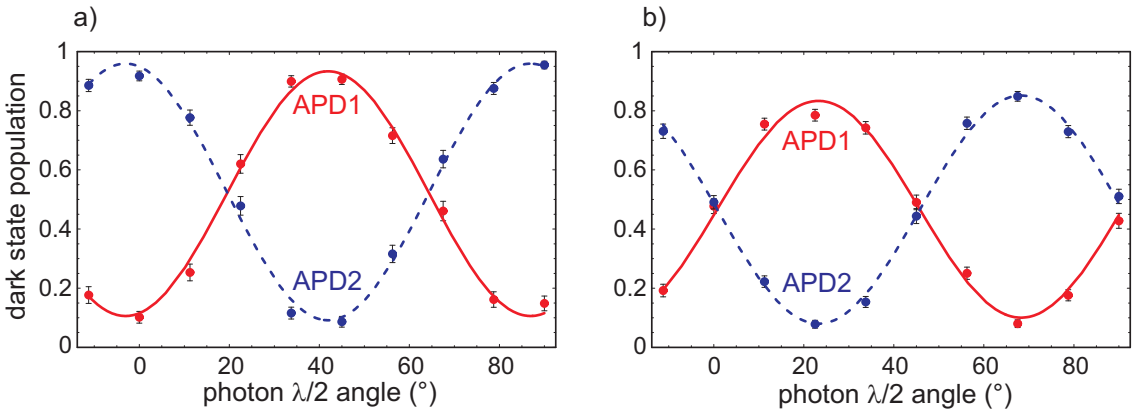

Figure 5.5.: Atom-photon correlations over a $300\,\mathrm{m}$ fiber. The halfwave plate defining the photonic measurement basis is rotated from $0°$ to $+90°$. The analyzed atomic state is $|\downarrow\rangle_x$ (a) and $|\downarrow\rangle_y$ (b).

To perform the compensation of the birefringence, reference light is sent into the fiber. On its output a rotatable mirror reflects the beam into the reference polarimeter. The compensation procedure, which takes less than $60\,\mathrm{s}$, is performed every experimental run (typically 12 minutes).

To prove the entanglement we have measured atom-photon correlations for two atomic measurement bases $\hat{\sigma}_x$ and $\hat{\sigma}_y$ (similar to Sec. 2.7.2). The result is shown in Fig. 5.5. The mean visibility of the correlation curves is $84.7\% \pm 2.7\%$ in (a) and $75.2\% \pm 2.6\%$ in (b). Taking the average of these two results (i.e. $80.0\% \pm 2.7\%$) and assuming this contrast in all bases we estimate the entanglement fidelity of $F = 0.85 \pm 0.02$.

The reduced visibility in the $\hat{\sigma}_y$ measurement is due to residual Larmor precession. In this measurement it leads to a partial rotation of the state $\frac{1}{\sqrt{2}}(|1,+1\rangle - i\,|1,-1\rangle)$ into the state $|1,0\rangle$ thereby reducing the contrast. By a better compensation of magnetic fields this issue will be eliminated in future experiments.

5.5. Summary

This chapter presents the necessary tools for maintaining the polarization of a photon during transmission over a long optical fiber. The birefringence of the fiber which is induced by mechanical stress is measured and compensated. For this purpose a polarimeter was set up which allows to characterize the polarization change of reference light with high precision (error $\leq 0.2\%$). An integrated fiber polarization controller serves to counteract the effect of the fiber. For finding optimal input parameters of the controller an algorithm was developed which iteratively minimizes the polarization error. The whole system operates automatically and finds the optimal parameters within several seconds. It is used periodically between the measurement runs and provides the necessary polarization stability.

First measurements of atom-photon entanglement over $300\,\mathrm{m}$ fiber have shown a fidelity of 0.85 only limited by residual magnetic fields acting on the atom. The optical fiber link has proven to be stable and reliable giving the necessary prerequisite for communicating the photon over a large distance.

6. Summary and Outlook

This work demonstrates the control over a system of a single atom entangled with a single photon. A microscopic optical dipole trap allows to isolate and to store a single atom. Entanglement between the spin of the atom and the polarization of the photon is generated using spontaneous decay in a Λ-type system. For the analysis of the entangled state a novel detection scheme was developed for analysis of the atomic state in arbitrary measurement bases. This method allowed to apply quantum state tomography to the atom-photon state and to completely characterize it revealing a fidelity of up to 90%. During my work the system was systematically improved, allowing to generate the entanglement (almost) on demand and to make it available for further applications.

The novel atom-photon entanglement achieved with our system opens up a variety of new possibilities. One of the most intriguing is the implementation of quantum teleportation between two very different systems: matter and light. It allows manipulation of the atomic state at a distance without the need of direct interaction. In order to achieve this we have encoded a state into the expanded Hilbert space of the photon by means of an interferometer. This state was then teleported onto the atom with a high fidelity, this was confirmed by full state tomography on the atom. This is the first demonstration of a quantum communication protocol between a photonic and an atomic qubit.

The most important application of the atom-photon entanglement is the interface between matter-based atomic memories and photonic quantum communication channels. This allows to combine the advantages of long coherence times in atomic systems with the ability of long-distance communication with photons. A part of this work was devoted to a study of both properties.

The coherence of the Zeeman sublevels which constitute the atomic qubit was characterized. This required understanding the rich dynamics of a spin-1 system. In order to characterize this system the method of qubit state tomography had to be extended allowing to estimate the degree of coherence of the analyzed state. The main mechanisms leading to dephasing were identified as fluctuations of external magnetic fields and of the fields induced by the optical trap. Such influences were systematically suppressed, in particular by active stabilization of magnetic fields. These measures have improved the coherence time by more than an order of magnitude to over $75\,\mu$s. The achieved stability is sufficient for current and future experiments.

Communication of the photon over long distances requires a reliable optical connection. For this purpose a fiber link of $300\,\mathrm{m}$ length was set up and tested. In order to compensate the distortion of the photonic polarization state in the fiber due to birefringence, an active polarization control was integrated. The fiber link maintained its stability for long periods of time keeping the polarization error below 1%. As a first step towards long-distance quantum communication we have established atom-photon entanglement over the long fiber. This experiment proves that the fiber link is appropriate for connection of distant laboratories.

Future work will be dedicated to the creation of entanglement between two atoms over a large distance. This can be done by generating two entangled atom-photon pairs in separated setups and sending the photons to an intermediate location. There, a Bell-state measurement on the photons projects the atoms onto an entangled state. A first demonstration of this so-called entanglement swapping with two ions was performed very recently in [80]. However, the emission wavelength for the ion in this experiment ($369.5\,\mathrm{nm}$) limits the fiber communication to a distance of few meters due to

absorption. In future we plan to create two entangled atoms at a distance of $300\,\mathrm{m}$. For this purpose a second atomic trap is now being set up in a neighboring laboratory. It incorporates a number of improvements, in particular, by using an objective with higher numerical aperture the photon collection efficiency is increased by more than a factor of 2. Additionally, its optical tables are designed such that the whole setup can be moved to a different location in order to increase the distance between the atomic traps.

With a pair of entangled atoms separated by a large distance a loophole-free Bell experiment becomes feasible. Such an experiment has to fulfill two conditions: (1) high detection efficiency and (2) strict locality, i.e. space-like separation of the measurement events with independent choice of the measurement basis. The first condition is fulfilled for the current scheme of atomic state detection (Sec. 2.6.5) which per definition has an efficiency of 100%. However, this detection procedure involves counting of photons to give the answer in which state the atom is, taking typically about $30\,\mathrm{ms}$. In order to fulfill the locality condition the required separation between the two experiments would be in this case at least $c \cdot 30\,\mathrm{ms} = 9000\,\mathrm{km}$. If one does not require that the answer about the atomic state is present at the output of the measurement system, but rather that the wavefunction has collapsed onto a certain state, the time becomes significantly shorter. The resonant scattering of light during the push-out process (Sec. 2.6.1) leads to the reduction of the state of more than 99% within $350\,\mathrm{ns}$. This allows to dramatically reduce the required distance.

However, to exclude any doubts resulting from the not absolutely clear role of the measurement process, a detection procedure is desired which is capable of giving a (classical) answer about the atomic state within a very short time. A possible solution is to replace the push-out process by state-selective ionization. The resulting free electron and Rubidium ion can then be detected by channel electron multipliers. This approach is currently investigated in our group. First measurements look promising revealing a detection efficiency of above 90% for detecting at least one of the fragments. The total detection process takes less than $1\,\mu\mathrm{s}$ which would allow a conclusive loophole-free Bell test at a distance of $300\,\mathrm{m}$.

A. Definition of light polarizations and atomic states

This section will define the light polarizations used in the text with respect to the real laboratory frame and the correspondence of those to the respective atomic transitions will be shown.

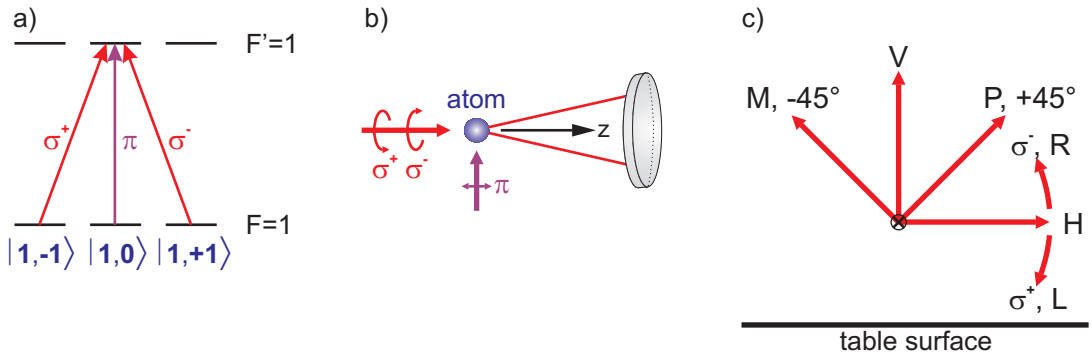

Figure A.1.: a) Definition of the $\sigma^{\pm}$ and π-transitions with respect to the atomic states. b) The corresponding polarization in the laboratory frame, the quantization axis is along the observation objective. c) Convention for polarizations when looking along the STIRAP beam propagation direction (source view).

The natural quantization axis for the atom in our experiment is given by the axis of the observation optics and shall be called z-axis throughout this work[1]. The three substates $|1,+1\rangle$, $|1,-1\rangle$ and $|1,0\rangle$ of the $F = 1$ ground level correspond (classically) to the orientations of the atomic spin along the quantization axis, opposite to its direction, or no well-defined orientation (projection equal to zero). We speak of an optical σ^+ transition if the absorption of the photon increases the projection of the atomic spin onto the quantization axis by one unit of $\hbar$. Respectively, a σ^- transition decreases the spin component by one unit of $\hbar$. A π-transition does not change the projection of atomic spin and corresponds to light polarization along the quantization axis. For circular polarization the handedness is defined by looking at the rotation of the electric field vector of the incoming beam from the point of view of the target. Clockwise rotation corresponds here to the right-circular polarization (R). According to the right-hand rule, for a beam going along the STIRAP path towards the observation objective (Fig. 2.4) the σ^+ transition corresponds to the left-circular (L) polarization. The horizontal polarization H is defined as being parallel to the surface of the optical table and V polarization as being orthogonal to it.

In contrast to the linear polarizations, which are easy to define in the experiment, the situation with the circular polarization is different. In order to determine the handedness of the polarization screw one needs a calibrated circular polarizer or waveplates with marked fast and slow axes. In our case

[1]The states of the atom and of the photon are analyzed along this direction.

symbol	composition	atomic dark state	qubit state
R	σ^-	$\|1,-1\rangle$	$\|\downarrow\rangle_z$
L	σ^+	$\|1,+1\rangle$	$\|\uparrow\rangle_z$
H	$\frac{1}{\sqrt{2}}(\sigma^+ + \sigma^-)$	$\frac{1}{\sqrt{2}}(\|1,+1\rangle + \|1,-1\rangle)$	$\|\uparrow\rangle_x$
V	$\frac{i}{\sqrt{2}}(\sigma^+ - \sigma^-)$	$\frac{i}{\sqrt{2}}(\|1,+1\rangle - \|1,-1\rangle)$	$\|\downarrow\rangle_x$
P, $+45°$	$\frac{1}{\sqrt{2}}e^{i\frac{\pi}{4}}(\sigma^+ - i\sigma^-)$	$\frac{1}{\sqrt{2}}e^{i\frac{\pi}{4}}(\|1,+1\rangle - i\|1,-1\rangle)$	$\|\downarrow\rangle_y$
M, $-45°$	$\frac{-1}{\sqrt{2}}e^{-i\frac{\pi}{4}}(\sigma^+ + i\sigma^-)$	$\frac{-1}{\sqrt{2}}e^{-i\frac{\pi}{4}}(\|1,+1\rangle + i\|1,-1\rangle)$	$\|\uparrow\rangle_y$

Table A.1.: Definitions of the basic polarizations and corresponding atomic states. The detection procedure (Sec. 2.6) empties the population of the remaining two states of the $F = 1$ level, and therefore can be considered as projection onto the dark state.

we were only able to define the handedness relatively to the detection, i.e. if the atom emits a right-circular polarized photon, it ends up in the state which is dark with respect to left-circular polarized STIRAP. Table A.1 shows a summary of STIRAP polarizations and corresponding analyzed states.

The entangled atom-photon state can be written in the three conjugate bases as

$$\begin{aligned} \left|\Psi^+\right\rangle &= \frac{1}{\sqrt{2}}\Big(\,|1,-1\rangle\left|\sigma^+\right\rangle + |1,+1\rangle\left|\sigma^-\right\rangle\Big) \\ &= \frac{1}{\sqrt{2}}\Big(\,|\downarrow\rangle_z|L\rangle + |\uparrow\rangle_z|R\rangle\Big) \\ &= \frac{1}{\sqrt{2}}\Big(\,|\downarrow\rangle_x|V\rangle + |\uparrow\rangle_x|H\rangle\Big) \\ &= \frac{1}{\sqrt{2}}\Big(\,|\downarrow\rangle_y|P\rangle + |\uparrow\rangle_y|M\rangle\Big). \end{aligned} \tag{A.1}$$

B. Quantum state tomography and quantification of state coherence

This section briefly describes the techniques used for acquisition of density matrices in our experiments. The relevant cases are a qubit (the photon or the $\{|1,+1\rangle, |1,-1\rangle\}$ subspace of the atomic $F = 1$ level), a qutrit (the full $F = 1$ space), and two qubits (joint atom-photon state). Furthermore a convenient measure for quantification of the coherence of a quantum state is introduced.

Single qubit

For a two-level system the density matrix of the state can be constructed by the straightforward relation (see e.g. [45]):

$$\hat{\rho} = \frac{1}{2}\left(\hat{\mathbb{1}} + \langle\hat{\sigma}_x\rangle \cdot \hat{\sigma}_x + \langle\hat{\sigma}_y\rangle \cdot \hat{\sigma}_y + \langle\hat{\sigma}_z\rangle \cdot \hat{\sigma}_z\right) = \frac{1}{2}\sum_{j=0}^{3} \langle\hat{\sigma}_j\rangle \cdot \hat{\sigma}_j \tag{B.1}$$

where $\hat{\sigma}_j \in \{\hat{\mathbb{1}}, \hat{\sigma}_x, \hat{\sigma}_y, \hat{\sigma}_z\}$ are the three Pauli operators together with the identity. Their expectation values can be determined by measuring the populations $p(|\uparrow\rangle_j)$, $p(|\downarrow\rangle_j)$ of the corresponding spin eigenstates (Stern-Gerlach measurement):

$$\langle\hat{\sigma}_j\rangle = p(|\uparrow\rangle_j) - p(|\downarrow\rangle_j)$$

in particular for the atom (see also Tab. A.1):

$$\begin{aligned}
\langle\hat{\sigma}_x\rangle &= p(\frac{1}{\sqrt{2}}(|1,+1\rangle + |1,-1\rangle)) - p(\frac{1}{\sqrt{2}}(|1,+1\rangle - |1,-1\rangle)) \\
\langle\hat{\sigma}_y\rangle &= p(\frac{1}{\sqrt{2}}(|1,+1\rangle + i\,|1,-1\rangle)) - p(\frac{1}{\sqrt{2}}(|1,+1\rangle - i\,|1,-1\rangle)) \\
\langle\hat{\sigma}_z\rangle &= p(|1,+1\rangle) - p(|1,-1\rangle)
\end{aligned} \tag{B.2}$$

As long as the atomic state is within the $\{|1,+1\rangle, |1,-1\rangle\}$ subspace (i.e. the $|1,0\rangle$ state is not populated), the relation $p(|\downarrow\rangle_j) = 1 - p(|\uparrow\rangle_j)$ holds and therefore $\langle\hat{\sigma}_j\rangle = 2p(|\uparrow\rangle_j) - 1$. Thus only one measurement of population per basis is required. Altogether three Stern-Gerlach measurements are necessary for the full tomography of the atomic level subspace $\{|1,+1\rangle, |1,-1\rangle\}$.

Two qubits

The preceding procedure of a single qubit tomography can be generalized for a system of two qubits. In this case the 4×4 density matrix is given by

$$\hat{\rho} = \frac{1}{4}\sum_{j,k=0}^{3} \langle\hat{\sigma}_j \otimes \hat{\sigma}_k\rangle \cdot \hat{\sigma}_j \otimes \hat{\sigma}_k \tag{B.3}$$

with $\hat{\sigma}_j \in \{\hat{\mathbb{1}}, \hat{\sigma}_x, \hat{\sigma}_y, \hat{\sigma}_z\}$. The left operator acts on the first qubit (the atom), the right one acts on the second qubit (the photon). The expectation values for products of Pauli operators $\langle \hat{\sigma}_j \otimes \hat{\sigma}_k \rangle$ are

$$\langle \hat{\sigma}_j \otimes \hat{\sigma}_k \rangle = p(|\uparrow\rangle_j |\uparrow\rangle_k) - p(|\downarrow\rangle_j |\uparrow\rangle_k) - p(|\uparrow\rangle_j |\downarrow\rangle_k) + p(|\downarrow\rangle_j |\downarrow\rangle_k) \tag{B.4}$$

where $p(|\Psi\rangle_1 |\Psi\rangle_2)$ is the population of the state $|\Psi\rangle_1 \otimes |\Psi\rangle_2$ in the two-qubit product space. Overall 3×3 measurements are required to determine the necessary expectation values for a complete two-qubit tomography.

Qutrit

During evolution in a magnetic field the atomic state can leave the $\{|1,-1\rangle, |1,+1\rangle\}$ subspace and therefore a modification of the analysis procedure is required. In order to perform a complete tomography of the spin-1 Hilbert space it is necessary to measure expectation values of operators which act on all three Zeeman states of the $F = 1$ space. It was shown [89, 90] that 5 Stern-Gerlach measurements (each providing the population of the 3 spin-1 eigenstates along a certain direction) are necessary and sufficient to obtain all elements of the density matrix. However, the atomic state detection procedure in our experiment (Sec. 2.6) is only able to select dark states in the $\{|1,-1\rangle, |1,+1\rangle\}$ subspace while an atom in the $|1,0\rangle$ state would be always transfered to $F = 2$ level and removed from the trap. Therefore, such Stern-Gerlach measurements can not be implemented in the current system[1]. Still, the population of the $|1,0\rangle$ state can be acquired indirectly (as the population missing in the $\{|1,-1\rangle, |1,+1\rangle\}$ subspace) allowing a partial reconstruction which is done as follows.

For the 3-state system $\{|1,-1\rangle, |1,+1\rangle, |1,0\rangle\}$ the 3×3 density matrix is

$$\hat{\rho} = \begin{pmatrix} \rho_{-1-1} & \rho_{-11} & \rho_{-10} \\ \rho_{1-1} & \rho_{11} & \rho_{10} \\ \rho_{0-1} & \rho_{01} & \rho_{00} \end{pmatrix} = \begin{pmatrix} & \hat{\rho}_s & \rho_{-10} \\ & & \rho_{10} \\ \rho_{0-1} & \rho_{01} & \rho_{00} \end{pmatrix} \tag{B.5}$$

where $\hat{\rho}_s$ is the sub-matrix of the $\{|1,-1\rangle, |1,+1\rangle\}$ system. From the measured state populations it can be calculated as

$$\hat{\rho}_s = p(|1,-1\rangle) \cdot |1,-1\rangle\langle 1,-1| + p(|1,+1\rangle) \cdot |1,+1\rangle\langle 1,+1| + \frac{1}{2}\langle \hat{\sigma}_x \rangle \cdot \hat{\sigma}_x + \frac{1}{2}\langle \hat{\sigma}_y \rangle \cdot \hat{\sigma}_y \tag{B.6}$$

where $\langle \hat{\sigma}_x \rangle$ and $\langle \hat{\sigma}_y \rangle$ are determined using Eq. (B.2). Furthermore $\rho_{00} = 1 - trace(\hat{\rho}_s)$ holds. Altogether we obtain the three diagonal and two off-diagonal elements of the density matrix for the atomic qutrit. The remaining off-diagonal elements (the coherences to the $|1,0\rangle$ state) have to be estimated. The lower bound is 0 while the upper bound is given by the inequality $|\rho_{jk}|^2 \leq \rho_{jj} \cdot \rho_{kk}$.

Quantification of coherence of a quantum state

In order to find a quantitative measure for coherence of a quantum state represented by the density matrix $\hat{\rho}$, the *purity* $P(\hat{\rho})$ is defined as

$$P(\hat{\rho}) := \mathrm{trace}(\hat{\rho}^2) \tag{B.7}$$

[1] This would require STIRAP-transfer including π-polarized light, which can not be applied along the quantization axis. In principle such measurements would become possible by implementing additional state analysis from direction orthogonal to the quantization axis.

In contrast to the fidelity $F = \langle\Psi_t|\hat{\rho}|\Psi_t\rangle$ which is defined with respect to a pure target state $|\Psi_t\rangle$, the purity is related to the coherent fraction of the density matrix with respect to the closest pure state which is in general unknown. As it is not necessary to find the closest pure state for the calculation of the purity parameter, its usage is especially convenient in the case where the state undergoes coherent evolution and is subject to decoherence at the same time.

The purity is a very general measure, however, it is not very intuitive. It is possible to construct a more intuitive measure by the following consideration. For a 2-level system the density matrix of a partially mixed state can be written in the form[2]

$$\hat{\rho} = (1-r)\frac{1}{2}\hat{\mathbb{1}} + r\,|\Psi\rangle\,\langle\Psi| \tag{B.8}$$

where r is the *purity parameter*, $|\Psi\rangle$ is a pure state and $\frac{1}{2}\hat{\mathbb{1}}$ represents a completely mixed state. It is straightforward to show that

$$\mathrm{trace}(\hat{\rho}^2) = \frac{1}{2}(1+r^2) \Rightarrow r = \sqrt{2P(\hat{\rho})-1} \tag{B.9}$$

In contrast to the purity P, the purity parameter r directly quantifies the coherent fraction of the density matrix.

For the 3-level system similar relations hold, the partially mixed state can be represented as

$$\hat{\rho} = (1-r)\frac{1}{3}\hat{\mathbb{1}} + r\,|\Psi\rangle\,\langle\Psi| \tag{B.10}$$

and then

$$\mathrm{trace}(\hat{\rho}^2) = \frac{1}{3}(1+2r^2) \Rightarrow r = \sqrt{\frac{1}{2}(3P(\hat{\rho})-1)}. \tag{B.11}$$

This relation is used for characterization of coherence of the atomic state in chapter 4.

[2]The representation of a partially mixed state is not unique. Here we use the convenient picture of a completely isotropic dephasing ("white noise").

C. Distribution of potential energy of a single atom in a harmonic trap

In this section I will consider the following problem: given a single particle (atom) in a harmonic potential, what is the distribution of potential energy (and thus of the light-shifts) in thermal equilibrium? For an optical dipole trap it determines the distribution of light-shifts, which is important for coherence properties. The answer is not given directly by thermodynamics, since in the case of a single particle the details of the motion play a role for the probability to get a certain state at a given time. This leads to the situation, where the distribution of the total energy E is well known (given by the Boltzmann distribution) but the distribution of the potential energy U can not be inferred from it. The Virial theorem states that for the harmonic potential the mean value obeys $\langle U \rangle = \frac{1}{2}E$ but gives no information on the distribution. Thus the motional details of the specific problem have to be considered.

1-dimensional case

We consider a 1-dimensional harmonic oscillator without damping. The potential energy is given by $U(x) = \frac{1}{2}kx^2$, where k is the spring constant. For a given total energy E_x the solution of the equation of motion is an oscillation $x(t) = A_x sin(\omega t)$ with the amplitude $A_x = \sqrt{\frac{2E_x}{k}}$. Then we can write the potential energy directly as

$$U(E_x, \phi_x) = E_x \sin(\phi_x)^2$$

where ϕ_x is the oscillation phase. In order to obtain the probability distribution of U for a given E_x we note that the phase ϕ_x is uniformly distributed, i.e. picking the oscillator at a random time gives any phase ϕ_x with equal probability (it is sufficient to consider $\phi_x \in [0..\frac{\pi}{2}]$). We get the probability density function

$$p_{E_x}(U) = \frac{1}{N}\frac{d\phi_x}{dU} = \frac{1}{N}\frac{d}{dU}\left(\arcsin(\sqrt{\frac{U}{E_x}})\right) = \frac{1}{N}\frac{1}{2\sqrt{U(E_x - U)}}$$

with a norm N. After normalization we get

$$p_{E_x}(U) = \frac{1}{\pi}\frac{1}{\sqrt{U(E_x - U)}} \tag{C.1}$$

This function has two poles, at $U = 0$ and $U = E_x$ (see Fig. C.1(a)) which can be easily understood. The first one is attributed to the local minimum of potential energy at zero. The second one is due to the turning point of the oscillation, the system spends a longer time at this point.

In thermal equilibrium we assume Boltzmann distribution $\frac{1}{k_B T}\exp(-\frac{E_x}{k_B T})$ of the total energy E_x. Therefrom we obtain the thermal distribution of potential energy

$$p_{1D}(U) = \int_0^\infty dE_x p_{E_x}(U)\frac{1}{k_B T}\exp(-\frac{E_x}{k_B T}) = \frac{1}{\sqrt{\pi}\sqrt{k_B T}}\frac{1}{\sqrt{U}}\exp(-\frac{U}{k_B T}) \tag{C.2}$$

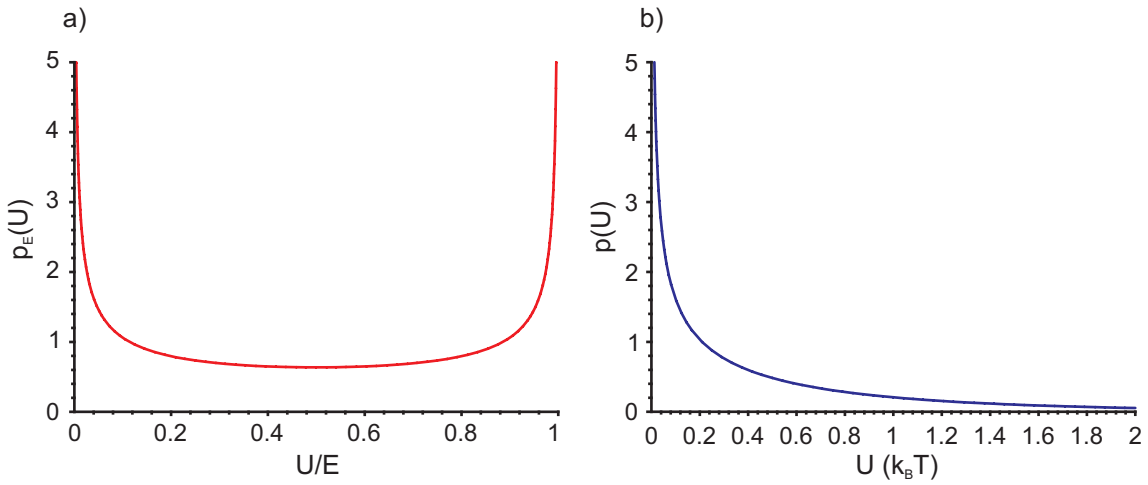

Figure C.1.: Potential energy distribution of a 1-dimensional harmonic oscillator. a) Probability density for a given total energy $E = E_x$. b) Probability density for Boltzmann distribution of the total energy E.

which is shown in Fig. C.1(b). The mean value of this distribution is $\frac{1}{2}k_BT$, in perfect agreement with the Virial theorem. Furthermore, since the kinetic energy $E_{kin} = E - U$ for the harmonic oscillator must have the same distribution, one can easily see

$$p(E) = \int_0^E dU(p_{1D}(U)p(E_{kin})) = \int_0^E dU(p_{1D}(U)p_{1D}(E-U)) =$$
$$= \frac{1}{\pi k_BT}\int_0^E dU \frac{1}{\sqrt{U}}\exp(-\frac{U}{k_BT})\frac{1}{\sqrt{E-U}}\exp(-\frac{E-U}{k_BT}) = \frac{1}{k_BT}\exp(-\frac{E}{k_BT})$$

which gives the expected 1-dimensional Boltzmann distribution of the total energy E.

2-dimensional case

As we extend the oscillation to two dimensions, the calculation of the probability density of the potential energy gets more difficult. The expression for the potential energy is

$$U(E_x, \phi_x, E_y, \phi_y) = E_x \sin(\phi_x)^2 + E_y \sin(\phi_y)^2$$

In contrast to the previous consideration, where the potential energy had an unambiguous dependence on ϕ_x, in two and more dimensions there are infinitely many states of motion with the same potential energy. One can obtain the probability density for the potential energy to be in the interval $[U, U + dU]$ by taking the derivative of the cumulative probability function $F(U)$ with respect to U:

$$p_{E_x,E_y}(U) = \frac{d}{dU}F_{E_x,E_y}(U)$$

where $F_{E_x,E_y}(U)$ is the probability to find a potential energy U' which is smaller or equal to U:

$$F_{E_x,E_y}(U) = P(U' \leq U) = \int_V d\phi_x d\phi_y$$

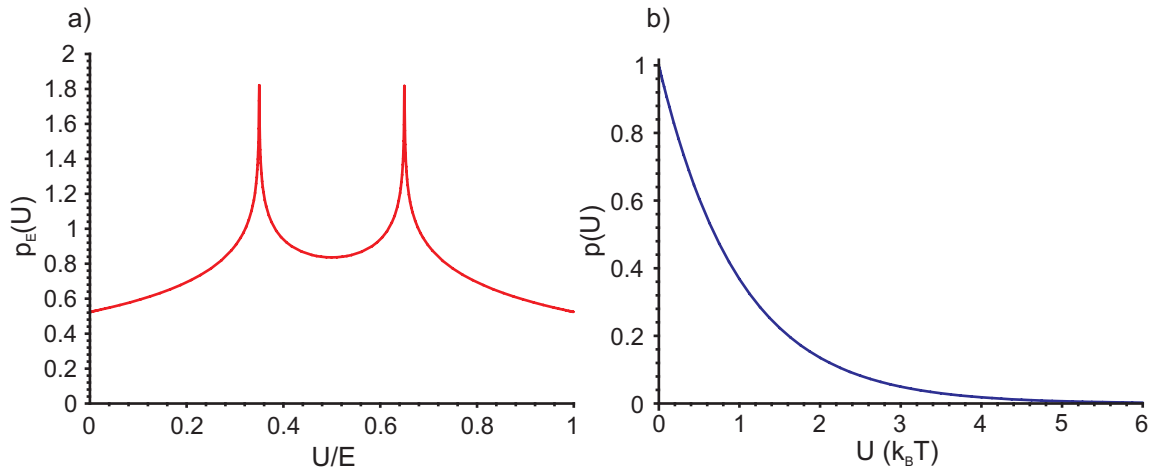

Figure C.2.: Potential energy distribution of a 2-dimensional harmonic oscillator. a) Probability density for $E_x = 0.65E$, $E_y = 0.35E$. b) Probability density for Boltzmann distribution of E_x, E_y.

and V is the set of states with potential energy $U' \leq U$ for given E_x, E_y. The result is

$$p_{E_x,E_y}(U) = \mathfrak{Im}\left(\frac{1}{2\sqrt{u(1-u)}}\mathcal{F}\left(-\infty, \sqrt{\frac{u(1-u)-e_x(1-e_x)}{u(1-u)}}\right)\right)$$

with $\mathcal{F}(z,k)$ being the incomplete elliptic integral of the first kind and $u = \frac{U}{E}$, $e_x = \frac{E_x}{E}$, $e_y = 1 - e_x$. An example of such distribution is shown in Fig. C.2(a), the two peaks in this picture correspond to the turning points of the two independent oscillations along the x- and y-axes.

Although the result for fixed energies E_x, E_y is already non-analytic, the thermal distribution can still be obtained. To do this we note that in thermal equilibrium the two oscillations are independent and their energies are Boltzmann distributed. The potential energy U is the sum of the two partial potential energies U_x, U_y. Then the 2-dimensional probability density function is the convolution of the two 1-dimensional densities:

$$\begin{aligned} p_{2D}(U) &= \int_0^U dU_x (p_{1D}(U_x) p_{1D}(U - U_x)) = \\ &= \frac{1}{\pi k_B T}\int_0^U dU_x \frac{1}{\sqrt{U_x}}\exp(-\frac{U_x}{k_B T})\frac{1}{\sqrt{U-U_x}}\exp(-\frac{U-U_x}{k_B T}) = \frac{1}{k_B T}\exp(-\frac{U}{k_B T}) \end{aligned} \quad \text{(C.3)}$$

Again one can easily check that this distribution has a mean value of $k_B T$ and that the distribution of the total energy E is

$$\begin{aligned} p(E) &= \int_0^E dU (p_{2D}(U) p_{2D}(E-U)) = \\ &= \frac{1}{(k_B T)^2}\int_0^E dU \exp(-\frac{U}{k_B T})\exp(-\frac{E-U}{k_B T}) = \frac{1}{(k_B T)^2} E \cdot \exp(-\frac{E}{k_B T}) \end{aligned}$$

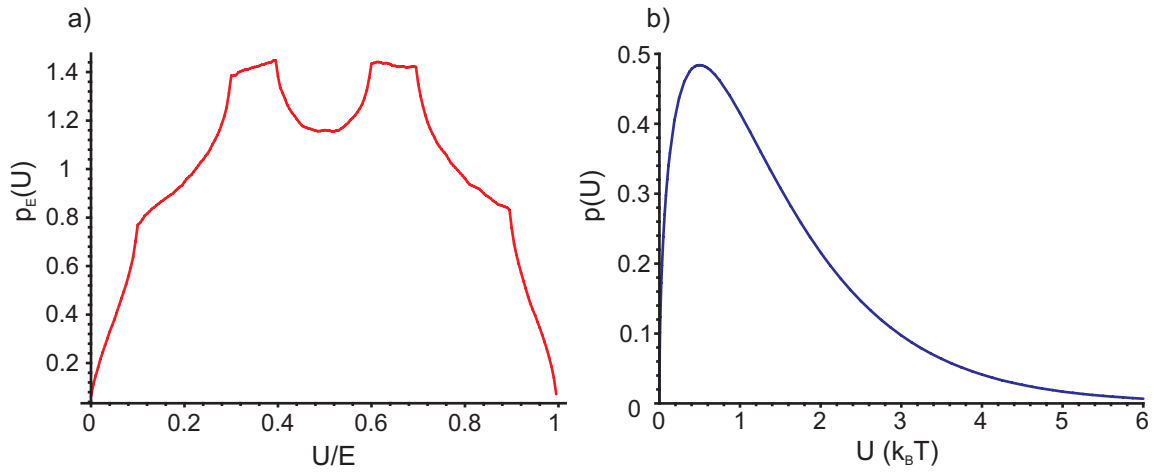

Figure C.3.: Potential energy distribution of a 3-dimensional harmonic oscillator. a) Probability density for $E_x = 0.6E$, $E_y = 0.3E$, $E_z = 0.1E$ (result of a Monte-Carlo simulation). b) Probability density for Boltzmann distribution of E_x, E_y, E_z.

3-dimensional case

The procedure of finding the probability density for fixed energies E_x, E_y, E_z is similar to the 2-dimensional case. The explicit calculation gave no closed expression, but it is possible to calculate distributions using a Monte-Carlo simulation. The program calculates the expression

$$U(E_x, \phi_x, E_y, \phi_y, E_z, \phi_z) = E_x \sin(\phi_x)^2 + E_y \sin(\phi_y)^2 + E_z \sin(\phi_z)^2$$

for fixed E_x, E_y, E_z by inserting random, uniformly distributed phases ϕ_x, ϕ_y, ϕ_z. Fig. C.3(a) shows the simulated probability density resulting from 10^9 calculated points.

The calculation of the probability density for Boltzmann distribution of energies E_x, E_y, E_z is done similar to Eq. (C.3) by performing a convolution of the 2-dimensional with a 1-dimensional distribution:

$$\begin{aligned} p_{3D}(U) &= \int_0^U dU_z p_{1D}(U_z) p_{2D}(U - U_z) = \\ &= \frac{1}{\sqrt{\pi}(k_B T)^{3/2}} \int_0^U dU_z \frac{1}{\sqrt{U_z}} \exp(-\frac{U_z}{k_B T}) \exp(-\frac{U - U_z}{k_B T}) = \frac{2}{\sqrt{\pi}(k_B T)^{3/2}} \sqrt{U} \exp(-\frac{U}{k_B T}) \end{aligned} \tag{C.4}$$

This distribution has a mean value of $\frac{3}{2} k_B T$ and the distribution of the total energy $E = U + E_{kin}$ is

$$\begin{aligned} p(E) &= \int_0^E dU (p_{3D}(U) p_{3D}(E - U)) = \\ &= \frac{4}{\pi(k_B T)^3} \int_0^E dU \sqrt{U} \exp(-\frac{U}{k_B T}) \sqrt{E - U} \exp(-\frac{E - U}{k_B T}) = \frac{1}{2(k_B T)^3} E^2 \exp(-\frac{E}{k_B T}) \end{aligned}$$

which is equal to the expected 3-dimensional Maxwell-Boltzmann distribution.

D. Polarization effects in strongly focused beams

The formalism of Gaussian optics in paraxial approximation is a very powerful tool for description of laser beams, it is valid for a very large range of beam parameters. However, if the beam is focused to a very small spot (few μm and less) the paraxial approximation fails because of the large beam divergence. In this case deviations from the Gaussian behavior occur, especially in the vicinity of the focus the polarization of the electric field is different and the form of the focal spot depends on the polarization as well. In our experiment especially the dipole trap beam is focused very tightly ($3.5\,\mu$m in the first trap and $1.2\,\mu$m for the new trap which is being set up). Therefore it is important to know how big these effects are and how do they influence the experimental parameters.

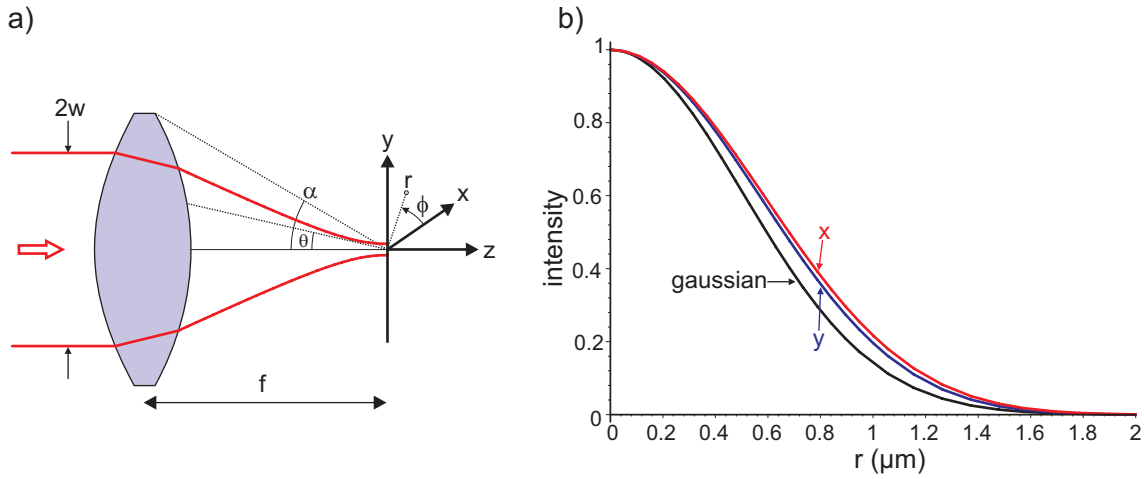

Figure D.1.: a) Focusing of a gaussian beam by a lens. b) Normalized intensity distribution in the focal plane for $w_0 = 1\,\mu$m and $\lambda = 856\,$nm, shown are cuts along x- (red) and y-direction (blue). The extension of the spot in along x-axis (direction of linear polarization of the input beam) is slightly larger than along y-axis. Black line shows the distribution expected from Gaussian optics with calculated waist w_0.

For the derivation of the diffraction integrals we follow the papers by Richards, Bovin and Wolf [91, 92] with the extension that a Gaussian beam is used instead of a plane wave at the input of the system. The beam, which propagates along the z-axis, has a wavelength λ, a (Gaussian) waist w and is linearly polarized along the x-axis. An ideal lens with a focal length f focuses the beam down, see Fig. D.1(a). The field distribution in vicinity of the focus can be explicitly calculated by integration

and is given in cylindric coordinates by

$$\begin{aligned} E_x(r,\phi,z) &= E_0 \cdot (F_0(r,z) + F_2(r,z)\cos(2\phi)) \\ E_y(r,\phi,z) &= E_0 \cdot F_2(r,z)\sin(2\phi) \\ E_z(r,\phi,z) &= E_0 \cdot 2iF_1(r,z)\cos(\phi) \end{aligned} \tag{D.1}$$

where r is the radius in x-y plane and ϕ is the angle with respect to the x-axis. E_0 is a scaling constant which describes absolute field strength and is not important in this consideration. The diffraction integrals are calculated as

$$\begin{aligned} F_0(r,z) &= \int_0^\alpha d\theta \exp(-\frac{f^2\tan(\theta)^2}{w^2})\sqrt{\cos(\theta)}(1+\cos(\theta))J_0(kr\sin(\theta))e^{ikz\cos(\theta)}\sin(\theta) \\ F_1(r,z) &= \int_0^\alpha d\theta \exp(-\frac{f^2\tan(\theta)^2}{w^2})\sqrt{\cos(\theta)}\sin(\theta)J_1(kr\sin(\theta))e^{ikz\cos(\theta)}\sin(\theta) \\ F_2(r,z) &= \int_0^\alpha d\theta \exp(-\frac{f^2\tan(\theta)^2}{w^2})\sqrt{\cos(\theta)}(1-\cos(\theta))J_2(kr\sin(\theta))e^{ikz\cos(\theta)}\sin(\theta) \end{aligned} \tag{D.2}$$

with J_0, J_1, J_2 being the Bessel-J functions of the first kind. The integration sums partial waves coming from infinitesimal rings on the lens, angle θ is the opening angle of these rings with respect to the z-axis as seen from the integration point. The lens aperture is defined by the opening angle α. We have found approximate expressions for the diffraction integrals which are valid for focal spot sizes down to $\sim 1\,\mu$m:

$$\begin{aligned} F_0(r,z) &\approx F_0(0,0)\frac{1}{\sqrt{1+\frac{z^2}{z_R^2}}}\exp\left(-\frac{r^2}{w_0^2(1+\frac{z^2}{z_R^2})}\right) \\ F_1(r,z) &\approx F_0(0,0)\frac{1}{2z_R}\frac{r}{1+\frac{z^2}{z_R^2}}\exp\left(-\frac{r^2}{w_0^2(1+\frac{z^2}{z_R^2})}\right) \\ F_2(r,z) &\approx F_0(0,0)\frac{1}{(2z_R)^2}\frac{r^2}{\left(1+\frac{z^2}{z_R^2}\right)^{\frac{3}{2}}}\exp\left(-\frac{r^2}{w_0^2(1+\frac{z^2}{z_R^2})}\right) \end{aligned} \tag{D.3}$$

where $w_0 = \frac{\lambda}{\pi}\frac{f}{w}$ and $z_R = \frac{\pi}{\lambda}w_0$ are the beam waist and Rayleigh range expected from Gaussian optics. The value $F_0(0,0)$ is given by

$$F_0(0,0) = \int_0^\alpha d\theta \exp(-\frac{f^2\tan(\theta)^2}{w^2})\sqrt{\cos(\theta)}(1+\cos(\theta))\sin(\theta)$$

Using the above expressions we have calculated the field distribution for different sizes of the focal spot. The first interesting effect of the tight focusing is the asymmetry of the focal spot. For the incoming beam being linearly polarized along x-axis the extension along x-axis is larger than along y-axis, see Fig. D.1(b). This effect was experimentally verified in [93]. However, for the spot sizes used in our experiment this effect is negligible, down to a spot size of $w_0 = 1\,\mu$m it is of the order of few percent.

The second important effect is the presence of longitudinal field E_z along the propagation direction. As the electromagnetic field is transversal by nature, this effect is surprising. However, it can be

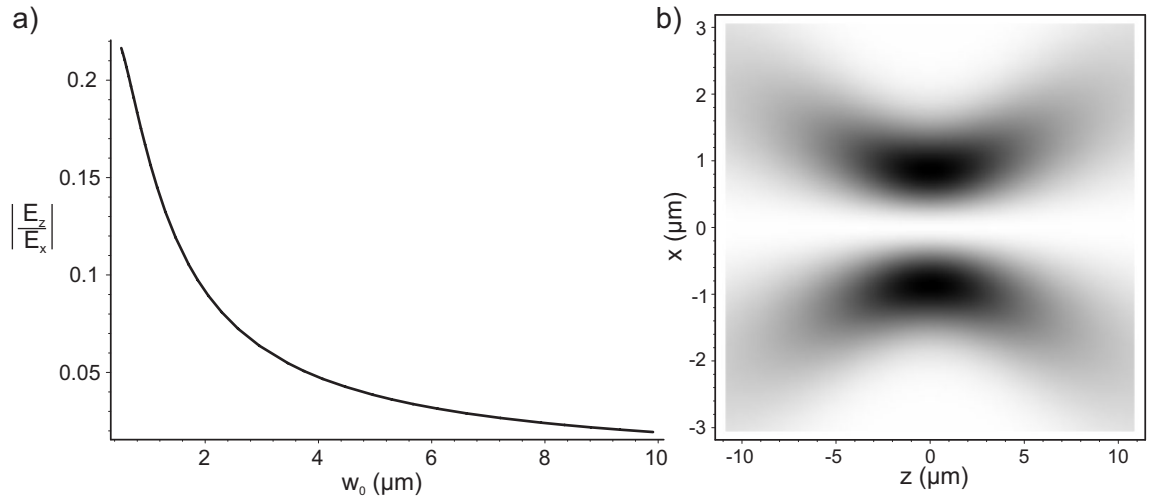

Figure D.2.: Longitudinal polarization near the focus of a linearly polarized beam. a) Ratio $\left|\frac{E_z}{E_x}\right|$ of the longitudinal field amplitude to the amplitude along direction of original polarization (along x-axis). The ratio is evaluated as a function of the beam radius (approximately w_0 from Gaussian optics) at the position of its maximum ($x \approx \frac{1}{\sqrt{2}} w_0$, $y = 0 = z$), here exact expressions (D.2) were used. b) Time averaged intensity distribution of the longitudinal component $|E_z|^2$ in the x-z plane (white corresponds to zero intensity, black to the maximum) for a spot radius of $1.2\,\mu\mathrm{m}$. The graphs were calculated for the wavelength of $\lambda = 856\,\mathrm{nm}$. To speed up the calculations, approximate expressions (D.3) were used.

understood because of the big divergence angle which is necessary for achieving a tight focus in the beam - the partial waves coming from different angles interfere in the focus giving a longitudinal field component. From Eq. (D.1) one can see that the longitudinal field E_z has a phase of $\frac{\pi}{2}$ with respect to the E_x component. Therefore, the field gets rotating components in the x-z plane which correspond to circular polarization along the y-axis. The distribution of intensity of the longitudinal component $|E_z|^2$ in the x-z plane is shown in Fig. D.2(b). On the z- and y-axes the intensity is equal to zero and has its maximum in the focal plane at $x \approx \frac{1}{\sqrt{2}} w_0$ where w_0 is the waist expected from Gaussian optics. The two "vortices" on different sides of the focus in x-z plane rotate in opposite directions (E_z has opposite signs). The fact that the longitudinal field is zero in the center of the trap reduces its effect upon the atoms which are located predominantly in the center. The $\frac{1}{e}$-radius of the thermal atomic density distribution is given in the transversal direction by $r_{th} = \sqrt{kT/2U_0}\, w_0$. For our typical experimental parameters ($U_0 = 0.65\,\mathrm{mK}$, $T = 0.15\,\mathrm{mK}$) this radius is $r_{th} = 0.34 \cdot w_0$. Within this region the longitudinal field is small, however, for higher temperatures the atomic distribution will extend to regions where the longitudinal field becomes significant.

The magnitude of the longitudinal field was calculated for different sizes of the focused spot, Fig. D.2(a). For the spot radius of $3.5\,\mu\mathrm{m}$ the expected relative amplitude at the position of its maximum is $\left|\frac{E_z}{E_x}\right|(3.5\,\mu\mathrm{m}) \approx 0.05$, which corresponds to a relative intensity of circular polarization along y-axis of about $2 \cdot (0.05)^2 = 0.005$. For even smaller focus sizes this effect will get important for coherence considerations because it will induce an effective magnetic field along y-axis (see chapter 4).

Bibliography

[1] A. Einstein, B. Podolsky, and N. Rosen. *Can Quantum-Mechanical Description of Physical Reality Be considered Complete?* Phys. Rev. **47**, 777 (1935).

[2] J.S. Bell. *On the Einstein-Podolsky-Rosen Paradox.* Physics **1**, 195 (1964).

[3] J.F. Clauser, M.A. Horne, A. Shimony, and R.A. Holt. *Proposed Experiment to Test Local Hidden-Variable Theories.* PRL **23**, 880 (1969).

[4] S.J. Freedman and J.F. Clauser. *Experimental Test of Local Hidden Variable Theories.* PRL **28**, 938 (1972).

[5] A. Aspect, P. Grangier, and G. Roger. *Experimental tests of Realistic Local Theories via Bell's Theorem.* PRL **47**, 460 (1981).

[6] A. Aspect, J. Dalibard, and G. Roger. *Experimental test of Bell's inequalities using time-varying analyzers.* PRL **49**, 1804 (1982).

[7] G. Weihs, T. Jennewein, C. Simon, H. Weinfurter, and A. Zeilinger. *Violation of Bell's inequality under strict Einstein locality conditions.* PRL **81**, 5039 (1998).

[8] P.H. Eberhard. *Background level and counter efficiencies required for a loophole free Einstein-Podolsky-Rosen experiment.* PRA **47**, R747 (1993).

[9] M.A. Rowe et al. *Experimental violation of a Bell's inequality with efficient detection.* Nature **409**, 791 (2001).

[10] M. Zukowski, A. Zeilinger, M.A. Horne, and A.K. Ekert. *"Event-Ready-Detectors" Bell Experiment via Entanglement Swapping.* PRL **71**, 4287 (1993).

[11] P.W. Shor. *Discrete logarithms and factoring.* Proc. 35th Ann. Symp. on Foundations of Computer Science p. 124 (1994).

[12] L.K. Grover. *A fast quantum mechanical algorithm for database search.* quant-ph/9605043v3 (1996).

[13] I.L. Chuang et al. PRL **80**, 3408 (1998); I.L. Chuang et al. Nature **393**, 143 (1998); M.A. Nielsen et al. Nature **396**, 52 (1998); L.M.K. Vandersypen et al. Nature **414**, 883 (2001).

[14] C. Monroe et al. PRL **75**, 4714 (1995); S. Gulde et al. Nature **421**, 48 (2003); M. Riebe et al. Nature **429**, 734 (2004); M.D. Barrett et al. Nature **429**, 737 (2004); J. Chiaverini et al. Nature **432**, 602 (2004); R. Reichle et al. Nature **443**, 838 (2006).

[15] O. Mandel et al. Nature **425**, 937 (2003); D. Schrader et al. PRL **93**, 150501 (2004).

[16] J. Volz et al. *Observation of Entanglement of a Single Photon with a Trapped Atom.* PRL **96**, 030404 (2006).

[17] M. Weber. *Quantum optical experiments towards atom-photon entanglement.* PhD Thesis. LMU Univ. of Munich (2005). http://nbn-resolving.de/urn:nbn:de:bvb:19-37985

[18] J. Volz. *Atom-Photon Entanglement.* PhD Thesis. LMU Univ. of Munich (2006). http://nbn-resolving.de/urn:nbn:de:bvb:19-56356

[19] B.B. Blinov, D.L. Moehring, L.M. Duan, and C. Monroe. *Observation of entanglement between a single trapped atom and a single photon.* Nature **428**, 153 (2004).

[20] T. Wilk, S.C. Webster, A. Kuhn, and G. Rempe. *Single-Atom Single-Photon Quantum Interface.* Science **317**, 488 (2007).

[21] D.N. Matsukevich et al. *Entanglement of a Photon and a Collective Atomic Excitation.* PRL **95**, 040405 (2005).

[22] N.D. Mermin. *Quantum Computer Science.* Cambridge Univ. Press (2007); M.A. Nielsen and I.L. Chuang. *Quantum Computation and Quantum Information.* Cambridge Univ. Press (2002); D. Bouwmeester, A. Eckert, A. Zeilinger. *The physics of quantum information.* Springer (2000).

[23] V. Giovanetti et al. Science **306**, 1330 (2004); A.N. Boto et al. PRL **85**, 2733 (2000); V. Giovanetti et al. PRL **96**, 010401 (2006).

[24] C.A. Kocher and E.D. Commins. *Polarization correlation of photons emitted in an atomic cascade.* PRL **18**, 575 (1967).

[25] C.Y. Lu et al. *Experimental entanglement of six photons in graph states.* Nature Physics **3**, 91 (2007).

[26] M. Eibl et al. PRL **92**, 077901 (2004); Z.Zhao et al. Nature **430**, 54 (2004); N. Kiesel et al. PRL **95**, 210502 (2005). N. Kiesel et al. PRL **98**, 063604 (2007).

[27] H. Häffner et al. *Scalable multiparticle entanglement of trapped ions.* Nature **438**, 643 (2005).

[28] O. Mandel et al. *Controlled collisions for multi-particle entanglement of optically trapped atoms.* Nature **425**, 937 (2003)

[29] D. Steck. *Rubidium 87 D Line Data.* http://steck.us/alkalidata

[30] T.W. Hänsch and A.L. Schawlow. *Cooling of gases by laser radiation.* Opt. Comm. **13**, 68 (1975).

[31] S. Chu, L. Hollberg, J.E. Bjorkholm, A. Cable, and A. Ashkin. *Three-dimensional viscous confinement and cooling of atoms by resonance radiation pressure.* PRL **55**, 48 (1985).

[32] E.L. Raab, M. Prentiss, A. Cable, S. Chu, and D.E. Pritchard. *Trapping of Neutral Sodium Atoms with Radiation Pressure.* PRL **59**, 2631 (1987).

[33] J. Dalibard and C. Cohen-Tannoudji. *Laser cooling below the Doppler limit by polarization gradients: simple theoretical models.* J. Opt. Soc. Am B, **6**, 2023 (1989).

[34] N. Schlosser, G. Reymond, and P. Grangier. *Collisional Blockade in Microscopic Optical Dipole Traps.* PRL **89**, 023005 (2002).

[35] M. Weber, J. Volz, K. Saucke, C. Kurtsiefer and H. Weinfurter. *Analysis of a single-atom dipole trap.* PRA **73**, 043406 (2006).

[36] E. Arimondo. *Coherent population trapping in laser spectroscopy.* Progr. Optics **35**, 257 (1996).

[37] H. Dehmelt. *Proposed* 10^{14} $\Delta\nu/\nu$ *Laser Fluorescence Spectroscopy on* Tl^+ *Mono-Ion Oscillator, II*. Bull. Am. Phys. Soc. **20**, 60 (1975).

[38] W. Nagourney, J. Sandberg, and H. Dehmelt. *Shelved optical electron amplifier: Observation of quantum jumps.* PRL **56**, 2797 (1986).

[39] R.G. Unanyan, M. Fleischhauer, B.W. Shore, and K. Bergmann. *Robust creation and phase-sensitive probing of superposition states via stimulated Raman adiabatic passage (STIRAP) with degenerate dark states.* Opt. Comm. **155**, 144 (1999).

[40] F. Vewinger, M. Heinz, R.G. Fernandez, V. Vitanov, and K. Bergmann. *Creation and measurement of a coherent superposition of quantum states.* PRL **91**, 213001 (2003).

[41] P.H. Lee and M.L. Skolnik. *Saturated Neon absorption inside a 6238-Å laser.* Appl. Phys. Lett. **10**, 303 (1967).

[42] L. Ricci et al. *A compact grating-stabilized diode laser system for atomic physics.* Opt. Comm. **117**, 541 (1995).

[43] K. Kurtsiefer. *A programmable pattern generator.* unpublished.

[44] T. Schmitt-Manderbach. *Long-distance free-space quantum key distribution.* PhD Thesis. LMU Univ. of Munich (2007). http://nbn-resolving.de/urn:nbn:de:bvb:19-81020

[45] D.F.V. James, P.G. Kwiat, W.J. Munro, and A.G. White. *Measurement of qubits.* PRA **64**, 052312 (2001).

[46] S. Berner. *Remote-State Präparation eines einzelnen Atoms.* Diploma Thesis. LMU Univ. of Munich (2006).

[47] C.H. Bennett et al. *Teleporting an Unknown Quantum State via Dual Classical and Einstein-Podolsky-Rosen Channels.* PRL **70**, 1895 (1993).

[48] S. Kuhr et al. Science **293**, 278 (2001); S. Kuhr et al. PRL **91**, 213002 (2003).

[49] S. Massar and S. Popescu. *Optimal Extraction of Information from Finite Quantum Ensembles.* PRL **74**, 1259 (1995).

[50] C.H. Bennett et al. *Purification of Noisy Enanglement and Faithful Teleportation via Noisy Channels.* PRL **76**, 722 (1996).

[51] D. Bouwmeester et al. *Experimental quantum teleportation.* Nature **390**, 575 (1997).

[52] D. Boschi, S. Branca, F. De Martini, L. Hardy, and S. Popescu. *Experimental Realization of Teleporting an Unknown Pure Quantum State via Dual Classical and Einstein-Podolsky-Rosen Channels.* PRL **80**, 1121 (1998).

[53] I. Marcikic, H. de Riedmatten, W. Tittel, H. Zbinden, and N. Gisin. *Long-distance teleportation of qubits at telecommunication wavelengths.* Nature **421**, 509 (2003).

[54] N. Lütkenhaus, J. Calsamiglia, and K.A. Suominen. *Bell measurements for teleportation.* PRA **59**, 3295 (1999).

[55] J.A.W. von Houwelingen, N. Brunner, A. Beveratos, H. Zbinden, and N. Gisin. *Quantum Teleportation with a Three-Bell-State Analyzer.* PRL **96**, 130502 (2006).

[56] M. Riebe et al. *Deterministic quantum teleportation with atoms.* Nature **429**, 734 (2004).

[57] M.D. Barrett et al. *Deterministic quantum teleportation of atomic qubits.* Nature **429**, 737 (2004).

[58] A. Furusawa et al. *Unconditional Quantum Teleportation.* Science **282**, 706 (1998).

[59] J. Sherson et al. *Quantum teleportation between light and matter.* Nature **443**, 557 (2006).

[60] C.H. Bennett et al. *Remote State Preparation.* PRL **87**, 077902 (2001).

[61] N. Peters et al. *Remote State Preparation: Arbitrary Remote Control of Photon Polarization.* PRL **94**, 150502 (2005).

[62] S.A. Babichev, B. Brezger, A.I. Lvovsky. *Remote Preparation of a Single-Mode Photonic Qubit by Measuring Field Quadrature Noise.* PRL **92**, 047903 (2004).

[63] X. Peng et al. *Experimental implementation of remote state preparation by nuclear magnetic resonance.* Phys. Lett. A **306**, 271 (2003).

[64] S. Popescu. *An optical method for teleportation.* quant-ph 9501020 (1995).

[65] M. Michler. *Quantentelepräparation und nicht kontextuelle verborgene Variable.* PhD-thesis, University of Vienna (2000).

[66] I.I. Rabi, J.R. Zacharias, S. Millman, and P. Kusch. *A new method of Measuring Nuclear Magnetic Moment.* Phys. Rev. **53**, 318 (1938).

[67] C. Ramanathan et al. *NMR Quantum Information Processing.* Quantum Information Processing **3**, 15 (2004).

[68] E.L. Hahn. *Spin Echoes.* Phys. Rev. **80**, vol. 4, 580 (1950).

[69] D.J. Wineland et al. *Quantum information processing and multiplexing with trapped ions.* Proc. 2002 Int. conference on atomic physics (2003).

[70] R. Blatt, H. Haeffner, C.F. Roos, C. Becher, and F. Schmidt-Kaler. *Ion Trap Quantum Computing with Ca^+ Ions.* Quantum Information Processing **3**, 61 (2004).

[71] D. Schrader et al. *Neutral Atom Quantum Register.* PRL **93**, 150501 (2004).

[72] B. Julsgaard et al. *Experimental demonstration of quantum memory for light.* Nature **432**, 482 (2004).

[73] C. Langer et al. *Long-Lived Qubit Memory Using Atomic Ions.* PRL **95**, 060502 (2005).

[74] S. Kuhr et al. *Analysis of dephasing mechanisms in a standing-wave dipole trap.* PRA **72**, 023405 (2005).

[75] W.H. Zurek. *Environment-induced superselection rules.* Phys. Rev. D **26**, 1862 (1982).

[76] H.A. Kramers and W. Heisenberg. *The scattering by radiation of atoms.* Zeits. f. Physik **31**, 681 (1925); G. Breit. *Quantum Theory of Dispersion.* Reviews of modern physics **4**, 504 (1932).

[77] R.A. Cline, J.D. Miller, M.R. Matthews, D.J. Heinzen. *Spin relaxation of optically trapped atoms by light scattering.* Opt. Lett. **19**, 207 (1994).

[78] D.N. Matsukevich et al. *Entanglement of Remote Atomic Qubits.* PRL **96**, 030405 (2006).

[79] D.L. Moehring et al. *Entanglement of single-atom quantum bits at a distance.* Nature **449**, 68 (2007).

[80] D.N. Matsukevich, P. Maunz, D.L. Moehring, S. Olmschenk, and C. Monroe. *Bell inequality violation with two remote atomic qubits.* PRL **100**, 150404 (2008).

[81] R. Ursin et al. *Entanglement-based quantum communication over 144 km.* Nature Physics **3**, 481 (2007).

[82] T. Schmitt-Manderbach et al. *Experimental demonstration of free-space decoy-state quantum key distribution over 144 km.* PRL **98**, 010504 (2007).

[83] H. Weier, T. Schmitt-Manderbach, N. Regner, C. Kurtsiefer, and H. Weinfurter. *Free space quantum key distribution: Towards real life application.* Fortschr. Phys. **54**, 840 (2006).

[84] D. Stucki, N. Gisin, O. Guinnard, G. Ribordy, and H. Zbinden. *Quantum key distribution over 67 km with a plug&play system.* New Journal of Physics **4**, 41.1 (2002).

[85] H. Hübel et al. *High-fidelity transmission of polarization encoded qubits from an entangled source over 100 km of fiber.* Opt. Express **15**, 223601 (2007).

[86] F. Hocke. *Long Distance Atom Photon Entanglement.* Diploma Thesis. LMU Univ. of Munich (2007).

[87] R. Ulrich, S.C. Rashleigh, and W. Eickhoff. *Bending-induced birefringence in single-mode fibers.* Opt. Lett. **5**, 273 (1980).

[88] N.G Walker and G.R. Walker. *Endless polarization control using four fibre squeezers.* Electronics Letters **23**, 290 (1987).

[89] R.G. Newton and B.L. Young. *Measurability of the Spin Density Matrix.* Annals of Physics **49**, 393 (1968).

[90] H.F. Hofmann and S. Takeuchi. *Quantum-state tomography for spin-l systems.* PRA **69**, 042108 (2004).

[91] E. Wolf. Proc. Roy. Soc. A **253**, 349 (1959); R. Richards and E. Wolf. ibid., 358.

[92] A. Bovin and E. Wolf. *Electromagnetic Field in the Neighborhood of the Focus of a Coherent Beam.* Phys. Rev. **138**, B 1561 (1965).

[93] R. Dorn, S. Quabis and G. Leuchs. *The focus of light - linear polarization breaks the rotational symmetry of the focal spot.* Journ. of Mod. Opt. **50**, 1917 (2003).

Acknowledgements

In the end I would like to thank the following persons:

- The members of the atom project: Jürgen Volz, my room neighbor for always helping me to cope with experimental problems, and exciting discussions about many things, including physics; Markus Weber for his different point of view; diploma students Stefan Berner, Peter Krebs, Fredrik Hocke, Christian Jakob, Andreas Deeg and Norbert Ortegel for their valuable contributions to the experiment and for distracting me with their questions; PhD students Florian Henkel, Michael Krug and Julian Hofmann for their patient work - good luck for the future!
- Past and present members of the Weinfurter group: Juliane Bahe, Magdalena Kaminska, Nadja Regner, Asli Ugur, Martin Fürst, Gerhard Huber, Harald Krauss, Nikolai Kiesel, Roland Krischek, Jan Lich, Davide Marangon, Yousef Nazirizadeh, Reinhold Pohlner, Markus Rau, Daniel Richart, Daniel Schlenk, Christian Schmid, Tobias Schmitt-Manderbach, Sebastian Schreiner, Pavel Trojek, Henning Weier, Chunlang Wang, Ulrich Weber, Witlef Wieczorek for the nice working atmosphere
- Prof. Harald Weinfurter for giving me the possibility to join the experiment and the big freedom during the work; Prof. Gerhard Rempe for being a referee of this work
- The whole group of Prof. Hänsch for creating an excellent scientific environment
- All QCCC-ists and in particular our coordinator, Thomas Schulte-Herbrüggen for interesting seminars and workshops; Elite Network of Bavaria for financial support
- Gabriele Gschwendtner and Nicole Schmidt for their organizational skills; Anton Scheich for his support in questions of electronics and for accepting with a smile that my circuits unexpectedly *do* work; Jürgen Aust, Thomas Großhauser and their team for solving our requests to the mechanical workshop quickly, precisely and competently
- My teacher Jury Jukelis - what he gave me has helped me all the way, especially during some hard and frustrating periods
- My friends, many of whom I did not see often during this period; Victor Czenter for many exciting moments under- and over water; Nikolai Kolachevsky for the nice conversations about physics and philosophy during mountain tours
- My wife Julia for creating a warm place, for her love and patience
- My parents for everything.